RIGA TECHNICAL UNIVERSITY
Faculty of Civil Engineering
Institute of Transportation Engineering

Andris Freimanis
Doctoral Student of the Study Programme "Civil Engineering"

CRACK DEVELOPMENT ASSESSMENT USING MODAL ANALYSIS IN PERIDYNAMIC THEORY

Scientific supervisor
Professor Dr. sc. ing.
AINĀRS PAEGLĪTIS

RTU Press
Riga 2019

Freimanis, A. Crack Development Assessment Using Modal Analysis in Peridynamic Theory. Doctoral Thesis. Riga: RTU Press, 2019. 113 p.

Published in accordance with the decision of the Promotion Council P-06 of August 20, 2019, Minutes No. 3-2019.

DOCTORAL THESIS PROPOSED TO RIGA TECHNICAL UNIVERSITY FOR THE PROMOTION TO THE SCIENTIFIC DEGREE OF DOCTOR OF ENGINEERING SCIENCES

To be granted the scientific degree of Doctor of Engineering Sciences, the present Doctoral Thesis has been submitted for the defense at the open meeting of RTU Promotion Council on November 29, 2019 at the Faculty of Civil Engineering of Riga Technical University, Kipsalas street 6B, room 422.

OFFICIAL REVIEWERS

Dr. sc. ing. Sandris Ručevskis
Riga Technical University

Professor Dr. sc. ing. Jānis Andersons
University of Latvia, Latvia

Professor Dr. sc. ing. Darius Bačinskas
Vilnius Gediminas Technical University, Lithuania

DECLARATION OF ACADEMIC INTEGRITY

I hereby declare that the Doctoral Thesis submitted for the review to Riga Technical University for the promotion to the scientific degree of Doctor of Engineering Sciences is my own. I confirm that this Doctoral Thesis had not been submitted to any other university for the promotion to a scientific degree.

Andris Freimanis …….
Date: ……

The Doctoral Thesis has been written in English. It consists of an Introduction; 6 Chapters; Conclusion; 54 figures; 30 tables; 2 appendices; the total number of pages is 114. The Bibliography contains 120 titles.

ABSTRACT

Structural damage is caused by design faults, construction quality shortcomings, or external effects. If such damage is not discovered and is allowed to grow, structure's load-bearing capacity deteriorates, which can lead to costly repairs or in extreme cases structure's collapse. However, accurate damage detection techniques can extend the life of these structures and provide measurable economic benefit.

Modal analysis is widely used to detect structural damage, for quality control in manufacturing, to validate numerical models, etc. In principle, engineers should be able to detect introduced damage from shifts in modal frequencies and changes in mode shapes, yet in practice, damage detection by modal analysis is difficult.

Modeling systems with evolving discontinuities e.g. cracks, still present a challenge, because classical theory uses partial differential equations, which are undefined when discontinuities are present in the displacement field. Contrary, peridynamic theory, which is a non-local reformulation of the classical theory, represents forces and displacements using integral equations, which are defined even with discontinuous displacement fields. Therefore, discontinuities are a natural part of a peridynamic solution rather than a burden, thus making this theory an attractive option for damage modeling. Peridynamic modal analysis, however, is still undeveloped.

This thesis aims to implement a novel massively-parallel open-source modal solver for peridynamic modal problems, verify its results against finite-element modal analysis results and validated them against experimental modal analysis results, and demonstrate how peridynamic modal analysis can be used together with peridynamic damage simulations to obtain modal parameters of damaged structures.

Peridynamic modal solver was implemented in an open source peridynamics software Peridigm. The implementation used the shift-invert transform, in which block Krylov-Schur eigensolver solved the eigenvalue problem and flexible block GMRES linear solver with ILU preconditioner solved the substitution. Solver parameters were optimized using four different peridynamic modal problems. The optimization cases were generated using Latin Hypercube method and the optimal solver parameters for the considered cases are presented.

Peridynamic modal analysis was used to compute modal properties of a 100 × 50 × 8 mm plate and nine different crack configurations were considered. Linear peridynamic solid material model, which is equivalent to an elastic material in the classical mechanics theory, was used and no boundary conditions were applied thus simulating the free-free boundary condition case. The first 12 modes were computed. The first six were rigid-body-motion modes, so only the second six were used for verification. Lastly, convergence studies were performed using four different mesh densities and four different horizon lengths.

Finite-element results were used to verify the accuracy of peridynamic modal analysis. A model with the same dimensions as in peridynamics was created in finite-element software Ansys using 8-node SOLID 185 elements. Linear-elastic material model was used and no BCs were applied. Cracks were created by not connecting solid element nodes that lay on the crack plane.

The experimental modal analysis results, measured with a 2D Polytec PSV-400 scanning laser vibrometer, were used for the experimental validation of the peridynamic results. Test specimens were 100 × 50 × 8 mm plates manufactured from polymethyl methacrylate (PMMA) sheets using laser cutting. The same nine crack configurations as used in peridynamic simulations were created and tested. Specimens were excited using a loudspeaker and they were suspended in two cotton thread loops to ensure free-free BC.

Results show excellent agreement between the peridynamic and the finite-element modal frequencies. The differences ranged between 0.00 % and -4.00 %. The peridynamic modal frequencies were lower as the horizon increased. This behavior can be explained by the increasing peridynamic "surface effect". Peridynamic results also agreed well with the experimental results. The modal frequencies were within ±3.2 % of the experimental results. Moreover, the peridynamic frequency shifts are similar to frequency shifts in the finite-element and experimental analyses. The largest difference between the peridynamic and the finite-element frequency shifts was -1.38 percentage points, but between the peridynamic and the experimental frequency shifts +1.95 percentage points. The peridynamic and the finite-element mode shapes agreed well and were in the same order at each crack configuration. Also, peridynamic and experimental mode shapes agreed well, furthermore, the change in the mode shapes from the introduced damage was similar in both analyses.

Two convergences – δm and δ – were considered. In the δm convergence study, results asymptotically approached a single value as the mesh density increased. The convergence is faster than linear, but slower than quadratic. Moreover, it was shown that the asymptotic range of convergence is reached with the largest model. The δ-convergence plots were not asymptotic and showed that the difference between the non-local and the local solution does not shrink smoothly as the horizon decreases.

Lastly, a practical application of p modal analysis is demonstrated. The developed modal solver was coupled with a peridynamic fatigue simulation and modal parameters were obtained before and after fatigue damage growth. The difference in modal frequencies was between -2.91 % and -0.45 %. The fatigue simulation created a measurable shift in modal frequencies, which can be used for damage assessment, model validation, and quality assurance.

ANOTĀCIJA

Konstrukciju bojājumus izraisa projekta kļūdas, nekvalitatīvs būvniecības process vai dažādas ārējas ietekmes. Ja šos bojājumus savlaicīgi neatklāj un ļauj tiem izplatīties, tad konstrukciju nestspēja samazinās, kas var novest pie dārgiem remontdarbiem vai, ekstrēmos gadījumos, pat to sabrukuma. Taču precīzas bojājumu noteikšanas metodes var paildzināt konstrukciju kalpošanas mūžu un radīt izmērāmu ekonomisko ieguvumu.

Modālo analīzi plaši izmanto konstrukciju bojājumu noteikšanā, ražošanas procesu kvalitātes kontrolē, skaitlisko modeļu validēšanai utt. Principā inženieriem vajadzēt varēt noteikt konstrukcijā radušos bojājumus no izmaiņām to modālajās frekvencēs un modu formās, taču praksē bojājumu noteikšana ar modālās analīzes palīdzību joprojām ir sarežģīta.

Sistēmu ar pārtraukumiem deformāciju laukā (piemēram, plaisu) modelēšana joprojām ir izaicinājums, jo klasiskā mehānikas teorija izmanto parciālos diferenciālvienādojumus, kuri nav definēti kā tikko deformāciju lauks nav nepārtraukts. Pretēji, peridinamikas teorija, kura ir nelokāls klasiskās teorijas pārformulējums, spēkus un pārvietojumus aprēķina izmantojot integrālvienādojumus, kuri ir definēti pat, ja deformāciju lauks ir pārtraukts. Tādejādi pārtraukumi deformāciju laukā ir dabiska peridinamikas risinājuma sastāvdaļa nevis papildu slogs, kas šo teoriju padara pievilcīgu dažādu bojājumu modelēšanai. Taču modālā analīze peridinamikas teorijā joprojām nav plaši apskatīta

Šīs disertācijas mērķis ir izstrādāt jaunu masīvi paralēlu atvērtā koda modālo risinātāju (*solver*) priekš peridinamikas modālajiem uzdevumiem, verificēt rezultātus pret modālo analīzi galīgo elementu metodē un validēt tos pret eksperimentālās modālās analīzes rezultātiem, un nodemonstrēt kā peridinamikas modālā analīze var tikt lietota kopā ar bojājumu simulācijām, lai iegūtu bojātu konstrukciju modālos parametrus.

Peridinamikas modālais risinātājs tika implementēts atvērtā koda peridinamikas aprēķinu programmā Peridigm. Tas izmantoja *shift-invert* transformāciju, kurā īpašvērtību problēmu atrisināja bloku Krilova-Šūra (*block Krylov-Schur*) īpašvērtību risinātājs un mainīgais bloku GMRES (*flexible block GMRES*) lineārais risinātājs ar ILU priekškondicionētāju (*preconditioner*) atrisināja substitūciju. Risinātāju parametri tika optimizēti izmantojot četras dažādas peridinamikas modālās problēmas. Optimizācijas parametri tika ģenerēti izmantojot Latīņu-Hiperkuba (*Latin Hypercube*) metodi un optimālie risinātāju parametri katrai optimizācijas problēmai ir parādīti.

Ar peridinamikas modālo analīzi aprēķināja $100 \times 50 \times 8$ mm lielas plāksnes modālās īpašības deviņās dažādās plaisu konfigurācijās. Tika izmantots *Linear peridynamic solid* materiāla modelis, kurš ir analogs lineāri elastīgam materiāla modeli klasiskajā mehānikas teorijā. Modelim netika pielikti nekādi robežnoteikumi tā simulējot *free-free* testa apstākļus. Aprēķinātas tika pirmās 12 modas. No tām pirmās sešas bija cieta ķermeņa kustības (*rigid-body motion*) modas, tādēļ tikai otrās sešas tika izmantotas verifikācijai. Beigās tika pētīta skaitliskā konverģence, izmantojot modeļus ar četriem dažādiem režģa blīvumiem un četriem dažādiem horizonta garumiem.

Galīgo elementu metodes rezultātus izmantoja, lai verificētu peridinamikas modālās analīzes precizitāti. Tāds pats modelis tika izveidots galīgo elementu metodes programmā

Ansys, izmantojot 8 punktu SOLID 185 elementus. Izmantots tika lineāri elastīga materiāla modelis un netika pielikti nekādi robežnoteikumi. Plaisas galīgo elementu modelī tika izveidotas nesavienojot elementu punktus, kuri atradās uz plaisas plaknes.

Eksperimentālās modālās analīzes rezultātus ieguva ar 2D Polytec PSV-400 skanējošo lāzera vibrometru un tos izmantoja peridinamikas rezultātu validēšanai. Testa paraugi bija 100 × 50 × 8 mm lielas plāksnītes, kuras ar lāzergriešanu izgatavotas no polimetil metakrilāta (PMMA) plātnēm. Tās pašas deviņas plaisu konfigurācijas, kuras izmantoja peridinamikas simulācijās, tika izmantotas arī laboratorijas testos. Paraugus iesvārstīja ar skaļruņa palīdzību un tie bija iekārti divās kokvilnas diega cilpās, lai nodrošinātu *free-free* robežnoteikumus.

Rezultāti rāda izcilu atbilstību starp peridinamikas un galīgo elementu modālajām frekvencēm. Atšķirības starp tām bija no -4.00 % līdz 0.00 % robežās. Peridinamikas modālās frekvences samazinājās, pieaugot horizonta garumam. To var izskaidrot ar pieaugošo peridinamikas "virsmas efektu". Laba atbilstība redzama arī starp peridinamikas un eksperimentu rezultātiem. Aprēķinātās modālās frekvences no eksperimentu rezultātiem neatšķīrās par vairāk kā ±3.2 %. Turklāt peridinamikas frekvenču nobīde (*frequency shift*) ir līdzīga galīgo elementu un eksperimentālo frekvenču nobīdei. Lielākā atšķirība starp peridinamikas un galīgo elementu frekvenču nobīdēm bija -1.38 procentpunkti, bet starp peridinamikas un eksperimenta frekvenču nobīdēm +1.95 procentpunkti. Peridinamikas un galīgo elementu modu formas sakrita un to secība pie katras plaisu kombinācijas bija vienāda. Peridinamikas un eksperimenta modu formas arī atbilda vienas otrām. Turklāt bojājumu izraisītās modu formu izmaiņas bija līdzīgas kā peridinamikas, tā eksperimentālajā analīzē.

Tika apskatītas divas konverģences – δm un δ. δm konverģences rezultāti, pieaugot tīkla blīvumam, asimptotiski tiecās uz vienu vērtību. Konverģence bija ātrāka kā lineāra, taču lēnāka par kvadrātisku. Turklāt ar lielāko izmantoto režģa blīvumu tika sasniegts asimptotiskais konverģences apgabals. δ konverģence nebija asimptotiska un parādīja, ka starpība starp nelokālo un lokālo rezultātu, saīsinoties horizontam, nesamazinās vienmērīgi.

Pēdējā nodaļa demonstrē praktisku peridinamikas pielietojumu. Izstrādātais modālās analīzes risinātājs tika savienots ar noguruma simulāciju un modālos parametrus ieguva pirms un pēc noguruma bojājumu simulācijas. Atšķirība modālajās frekvencēs bija starp -2.91 % un -0.45 %. Noguruma simulācija radīja izmērāmu frekvenču nobīdi, kuru var izmantot bojājumu novērtēšanā, aprēķina modeļu validācijai un kvalitātes pārbaudēm.

TABLE OF CONTENTS

1 INTRODUCTION

1.1 Novelty and motivation

Structural damage is caused by design faults, construction quality shortcomings, or external effects such as improper use, overloading, natural disasters, environmental factors, etc. If damage is not discovered and is allowed to grow, structure's load-bearing capacity deteriorates, which can lead to costly repairs or in extreme cases its collapse. Notable examples include Ponte Morandi bridge collapse in Genoa, Italy in 2018 [1], Florida International University pedestrian bridge collapse in Florida, the USA in 2018 [2] and Maxima department store collapse in Riga, Latvia in 2013 [3].

Moreover, damage accumulates as a part of a structures' natural aging process. In situations as, for example, in Latvia where 37 % of all bridges are reported as either in poor or very poor condition [4], or in Europe where 35 % of its roughly half a million rail bridges are over 100 years old [5], accurate damage detection techniques can extend life of these structures and provide measurable economic benefit [6–8].

On top of natural aging, an increasing number of extreme loading conditions due to climate change also contribute to faster deterioration of the infrastructure. Some scenarios have shown that in Latvia an increase of 80 % - 100 % in bridge scour risk can be expected by 2070-2100 [9].

Modal analysis is widely used to detect structural damage, to control quality in manufacturing, to validate numerical models, etc. Modal properties – modal frequencies and mode shapes – depend on the object's mechanical and geometrical properties. When damage, such as cracks, is introduced in a structure its geometrical and/or mechanical properties change. In principle, engineers should be able to detect introduced damage from shifts in modal frequencies and changes in mode shapes. In practice, damage detection by modal analysis is hard due to several limitations:

- generally, the damage is localized, but computed or experimentally determined modes represent global displacements, therefore, local phenomena must be detected from a change in global data;
- frequency shifts due to damage are often small compared to the influence of boundary conditions or test conditions e.g. wind for bridges;
- lack of computational approaches that allow both crack growth modeling and modal analysis.

Modal analysis use in structural health monitoring will not be discussed here in detail, because it in itself is not the topic of this thesis, but quality reviews are presented in [10–14].

An interesting research project [15] used an inverse eigenvalue problem to find the location and magnitude of several masses attached to a string from measured modal properties. If it is possible to compute changes in mass matrix i.e. locations of several masses using an inverse modal problem, then it might be also possible to use inverse eigenvalue problem to compute changes in stiffness matrix i.e. crack locations. However, this requires explicit crack modeling,

rather than simulating damage by adding mass or reducing node stiffness as is common in finite-element (FE) analysis.

Additionally, there is a clear need for new and open computational modeling and simulation software as noted by the European Materials Modeling Council's roadmap [16]. Moreover, need for new modeling software particularly for engineering applications, such as uncertainty quantification, risk analysis and decision in engineering, is recognized by the Council of the European Union in its decision that established the Horizon 2020 (H2020) framework programme for research and innovation [17]. In particular, H2020 topics, such as NMP-20-2014 Widening materials models, FoF-08-2015 ICT-enabled modelling, simulation, analytics and forecasting technologies, NMBP-23-2016 Advancing the integration of Materials Modelling in Business Processes to enhance effective industrial decision making and increase competitiveness, NMBP-25-2017 Next generation system integrating tangible and intangible materials model components to support innovation in industry, DT-NMBP-09-2018: Accelerating the uptake of materials modelling software, and DT-NMBP-10-2019 Adopting materials modeling to challenges in manufacturing processes, shows that readily available modeling software for use in industry is required [18–20].

Several problems, however, inhibit wide use of modeling tools. They are often seen as difficult to use and not accurate enough. Particularly for small enterprises, they require a substantial investment in terms of people (expertise), infrastructure and capital. Software licenses present another issue that prohibits the industry from using computational codes developed in academia [16]. Keeping this in mind, all computational code written as part of this thesis will be made available on Github or similar code repositories thereby enabling researchers and engineers to use it freely.

Peridynamic theory or peridynamics (PD) is a non-local reformulation of classical continuum mechanics theory originally proposed by Stewart Silling [21,22] to address limitations of the classical theory when a displacement field is discontinuous. Modeling systems with evolving discontinuities e.g. cracks, still present a challenge, because classical theory uses partial differential equations, which are undefined when discontinuities are present in the displacement field. Contrary, peridynamic theory represents forces and displacements using integral equations, which are defined even with discontinuous displacement fields. Therefore, discontinuities are a natural part of a PD solution rather than a burden, thus making this theory an attractive option for damage modeling.

A peridynamic body in its continuum definition consists of an infinite number of nodes. Each node is connected through bonds to all other nodes within a range called the horizon. This name was chosen because interaction vanishes for nodes that are farther than one horizon away from each other. Essentially a node doesn't "see" past its horizon. The peridynamic theory is non-local because a node can be connected to other nodes that are not its nearest neighbors as long as the distance between them is shorter than the horizon. Moreover, PD models converge to continuum mechanics models in the limit when the horizon approaches zero for smooth deformations [23,24] and non-smooth solutions of non-local models [25]. PD models also recover molecular dynamics results for atomistic resolution, therefore, they can be considered an upscaling of molecular dynamics models [26]. A brief introduction to peridynamics is

presented in Chapter 2 Theory background, but for an extended overview, the author recommends [27–29].

Other non-local formulations of continuum mechanics have been discussed by several authors [30,31]. Moreover, it has been showed that the stresses in front of the crack tip are finite as the crack tip is approached asymptotically, rather than infinite as in local continuum mechanics theory [32,33], but this formulation still uses spatial partial derivatives to represent forces and displacements, which are undefined on the surface of discontinuities.

Damage in PD is introduced by breaking a bond according to some specified damage law. The benefit is that peridynamics allow for "spontaneous" crack formation, meaning that they were not present initially, but formed after some damage criterion was exceeded. It follows that the crack path doesn't have to be specified *a priori.* Cracks will initiate and grow according to the specified damage criterion.

Since its introduction in 2000, the peridynamic theory has experienced increased use. Its applications include modeling of concrete [34–37], wood [38], crystal plasticity [39,40], laminated-composite materials [41–45], layered glass [46], fatigue damage [47–52], corrosion damage [53], dynamic blast loading [54], shock wave in granular material [55], hydraulic fracturing [56], ship's propeller-ice impact [57], crack propagation and branching [58] and crack nucleation [59]. PD modal analysis for structural health monitoring has been explored only in [60], which considered only limited 2D benchmark problems.

The author's preliminary studies showed that solving PD modal problems poses significant challenges. First, peridynamic stiffness matrices are non-symmetric, thus require non-Hermitian solvers and working with complex numbers. Second, a node in PD is generally connected to more nodes than a node in FE analyses, thus stiffness matrices contain more non-zeros and their bandwidth is wider. Third, PD models are usually large in number of nodes, which means that the matrix size is also large. These factors increase the computational cost of PD modal problems and can lead to poor solver convergence. Moreover, due to large computational cost, these simulations are frequently run on computing clusters, which require a massively-parallel computational implementation, otherwise the length of simulations would be prohibitively long. Therefore, a considerable part of the research for this thesis was devoted to finding and implementing a combination of solvers that can solve PD modal problems in an efficient manner in a parallel environment. These challenges are explained in more detail in chapter 3.1 Peridynamic implementation.

The scientific novelty of the presented research is the following:

- the well-known modal analysis has been implemented and studied in a new mechanic's theory – peridynamics – in which it has not been explored in detail before. The difference from the previous authors' work is that 3D rather than 2D problems are considered, which means that more than just bending modes are present, and the results are verified and validated at several crack configurations rather than only at undamaged and one damaged configuration, thereby providing more detailed analysis;
- this thesis developed, implemented and optimized the first massively-parallel and open-source PD modal solver in the world. Since it is open-source, it will be freely

available to researchers in academia and industry, ensuring the sustainability of the research.

The selection of this topic was motivated by three challenges mentioned previously:

- the difficulty of detecting structural damage through changes in modal properties;
- the clear need for new and open computational modeling tools for European academia and industry;
- the potential use of explicit crack modeling in peridynamic theory together with the modal analysis to detect and locate structural damage.

1.2 Aim and scope

This thesis aims to develop a novel massively-parallel open-source modal solver for peridynamic modal problems, verify its results against finite-element modal analysis results, validate them against experimental modal analysis results, and demonstrate how PD modal analysis can be used together with PD damage simulations to obtain modal parameters of damaged structures.

This thesis will not try to show that PD modal analysis is better than FE modal analysis and should be used in its place from now on. Rather the goal is to show that PD analysis is a viable alternative when considering problems where damage is present.

The FE analysis was chosen because it is the most popular computational method for modal analysis, therefore, is well understood, widely used, and trusted by engineers and researchers. The experimental modal analysis was chosen to provide an independent reference point for both computational methods.

The thesis will be limited with the development and optimization of a peridynamic modal solver, followed by verification and validation of its results, and, lastly, a demonstration of its use together with a fatigue simulation.

The scope of the thesis will be limited in several ways:

- a rectangular plate structure will be used. Common real-life structures would have a more complex shape, however, the thesis considers development and testing of a viable peridynamic modal analysis approach not simulations of any real-life structures. For that purpose, a plate shape is sufficient. Additionally, FE and PD computational model and the test specimens for the experimental analysis will be easy to make. Moreover, a rectangular plate contains both bending and torsional modes within the measurement range;
- test specimens will be manufactured from a linear-elastic material – polymethyl methacrylate – because it's easy to obtain, cheap, easy to cut into shape, easy to work with (not heavy as concrete, smelly as asphalt, abrasive as glass fiber). It follows that linear-elastic material models will be used in simulations;
- the experimental modal analysis will be done in 2D due to limitations of available equipment, but numerical analyses will be done in 3D;
- cracks in verification and validation experiments will be created manually, instead of naturally occurring e.g. fatigue or corrosion cracking;

- the fatigue damage model will be used for demonstration of PD modal analysis applications.

1.3 Thesis tasks

To achieve the aim of the thesis, the following tasks must be fulfilled:

1. Develop and optimize a modal solver that can be efficiently run in a massively-parallel computing environment on a computing cluster and can solve a peridynamic modal problem;
2. choose a test specimen and compute its modal frequencies and mode shapes at nine different crack configurations using PD and FE modal analysis, obtain its experimental modal properties using the experimental modal analysis. Then verify the PD results against the FE results and validate them against the experimental results;
3. consider several mesh densities and horizon lengths in the PD simulations to study the mesh convergence;
4. demonstrate the use of PD modal analysis coupled with a fatigue damage simulation.

1.4 Thesis practical value

The developed computer code will be made freely accessible (open-source) to researchers and engineers worldwide. Thereby, ensuring that the results of this research can be practically applied and used in further research, rather than left lying on a shelf. Additionally, this will ensure the sustainability of the research.

Modeling of systems with evolving discontinuities still presents a challenge because classical continuum mechanics theory uses partial differential equations, which are undefined when discontinuities are present in the displacement field. Contrary, peridynamic theory represents forces and displacements using integral equations, which are defined even with discontinuous displacement fields. Therefore, discontinuities are a natural part of a PD solution rather than a burden, thus making this theory an attractive option for damage modeling.

Combining this advantage with modal analysis improves the currently used techniques in numerical model validation, product design, manufacturing quality assurance, and structural damage detection. Moreover, the peridynamic modal solver is implemented in open-source software, so researchers and engineers worldwide can use the developed code for free and with few restrictions.

Furthermore, a practical use-case of the peridynamic analysis is presented. A fatigue damage simulation is combined with the developed modal solver and the modal parameters of a test object are obtained at 0 and 870 000 fatigue cycles. Such simulations can be used for model validation, manufacturing quality assessment, and structural damage detection. For example, when simulation results are compared to experimental modal results, the simulated data can be used to judge how many fatigue cycles has an object already endured and how many are left until a failure.

1.5 Arguments for the defense of the thesis

- The developed peridynamic modal solver implementation has been optimized for use in a massively-parallel computational environment and can solve PD modal problems.
- The PD modal frequencies are in excellent agreement with the FE and the experimental modal frequencies in both undamaged and damaged configurations.
- The PD mode shapes agree well with and are in the same order as the FE mode shapes at a single crack configuration. The PD mode shapes also agree well with the experimental mode shapes. Moreover, the change in mode shapes from the introduced damage is similar in both analyses.
- The PD modal analysis can be coupled with PD damage simulations to simulate damage and obtain modal properties of the damaged object.

1.6 List of conferences

1. 6th European Conference on Computational Mechanics, 7th European Conference on Computational Fluid Dynamics ECCM-ECFD 2018, Glasgow, UK, 11-15 June 2018. http://www.eccm-ecfd2018.org/frontal/default.asp
2. 2018 International Symposium of Rail Infrastructure Systems Engineering (i-RISE 2018), Brno, Chechia
3. International Modal Analysis Conference IMAC-XXXVI 2018, Orlando, Florida, USA, 12-15 February 2018 https://semimac.org/event/imac-xxxvi/
4. The 3rd International Conference on Innovative Materials, Structures and Technologies IMST 2017, Riga, Latvia, 27-29 September 2017. https://imst.rtu.lv/node/46
5. Modern building materials, structures, and techniques MBMST 2016, Vilnius, Lithuania, 26-27 May 2016. http://mbmst.vgtu.lt/

1.7 List of publications

The following publications were published during the research for this thesis. They are arranged in chronological order starting with the most recently published papers. An asterisk (*) shows papers included in either Scopus or Web of Science databases.

1. Freimanis, A.; Paeglītis, A. Modal Analysis of Healthy and Cracked Isotropic Plates in Peridynamics. Conf. Proc. Soc. Exp. Mech. Ser. 2019, 359–361, doi:10.1007/978-3-319-74700-2_41. *
2. A. Freimanis, S. Kaewunruen, and M. Ishida, “Peridynamic Modeling of Rail Squats,” in Sustainable Solutions for Railways and Transportation Engineering: Proceedings of the 2nd GeoMEast International Congress and Exhibition on Sustainable Civil Infrastructures, 2019, pp. 108–118.
3. Freimanis, A.; Kaewunruen, S. Peridynamic Analysis of Rail Squats. Appl. Sci. 2018, 8, 2299, doi:10.3390/app8112299. *

4. Kaewunruen, S.; Janeliukstis, R.; Freimanis, A.; Goto, K. Normalised curvature square ratio for detection of ballast voids and pockets under rail track sleepers. J. Phys. Conf. Ser. 2018, 1106, 012002, doi:10.1088/1742-6596/1106/1/012002. *
5. S. Kaewunruen, A. Freimanis, and M. Ishida, "EFFECT OF EXTREME CLIMATE ON WHEEL-RAIL INTERACTION OVER RAIL SQUATS," in Proceedings of the 6th. European Conference on Computational Mechanics (Solids, Structures and Coupled Problems) ECCM 6, 7th. European Conference on Computational Fluid Dynamics ECFD 7, 2018, pp. 11–15.
6. Freimanis, A.; Kaewunruen, S.; Ishida, M. Peridynamics Modelling of Rail Surface Defects in Urban Railway and Metro Systems. Proceedings 2018, 2, 1147, doi:10.3390/proceedings2161147.
7. Freimanis, A.; Paeglitis, A. Mesh Sensitivity in Peridynamic Quasi-static Simulations. Procedia Eng. 2017, 172, 284–291, doi:10.1016/j.proeng.2017.02.116. *
8. Freimanis, A.; Paeglītis, A. Modal analysis of isotropic beams in peridynamics. IOP Conf. Ser. Mater. Sci. Eng. 2017, 251, 012088, doi:10.1088/1757-899X/251/1/012088.*
9. Paeglitis, A.; Freimanis, A. Comparision of constant-span and influence line methods for long-span bridge load calculations. Balt. J. Road Bridg. Eng. 2016, 11, 84–91, doi:10.3846/bjrbe.2016.10. *
10. Freimanis, A.; Paeglītis, A. Analysis of Yearly Traffic Fluctuation on Latvian Highways. IOP Conf. Ser. Mater. Sci. Eng. 2015, 96, 012064, doi:10.1088/1757-899X/96/1/012064. *

1.8 Thesis composition and outline

This thesis is structured in eight chapters, as follows:

- chapter 1 Introduction presents the motivation behind the thesis and its novelty, defines thesis aim and scope, outlines thesis chapters and lists articles published during the research period;
- chapter 2 Theory background introduces theories, tools, and methods used in the thesis, such as peridynamic theory, modal analysis, and linear algebra concepts;
- chapter 3 Computational implementation and optimization describes the problems and solutions behind computational implementation of PD modal solver and the optimization process of its parameters;
- chapter 4 Specimen manufacturing and experimental setup goes over the selection and manufacturing of test specimens and experimental setup used to obtain their mechanical and modal properties;
- chapter 5 Verification and validation of peridynamic modal analysis compares modal properties computed peridynamic modal properties with those computed using finite-element analysis and measured experimentally;
- chapter 6 Convergence studies show how the results converge with changing computational mesh density and horizon length;

- chapter 7 Demonstration of peridynamic modal analysis application combines the developed modal solver with a fatigue simulation to show one of its potential applications;
- chapter 8 Conclusions summarizes thesis work and draws conclusions from the presented material.

The thesis is 114 pages long and written in English. It contains 54 figures, 30 tables, and 120 references.

2 THEORY BACKGROUND

Generally, researchers will be more or less familiar with the topics presented in this chapter, however, the author considered it worthwhile to present this information, so that it is available in a short and condensed form. This chapter has three parts: the first presents the peridynamic theory, but for a broader overview the author recommends [27–29,61]; the second discusses the computational modal analysis and more information please see [62–65]; lastly, the third part presents linear algebra concepts and for a wider discussion the author recommends [66,67].

2.1 Peridynamic theory

A peridynamic body B consists of an infinite number of nodes each uniquely described by its position vector in the reference configuration $\boldsymbol{x_i}$, volume V_i, density ρ_i and. An example of a discretized two-dimensional PD body is showed in figure 2.1. Node $\boldsymbol{x_i}$ interacts with other nodes $\boldsymbol{x_j}$ through bonds (relative position vectors) $\boldsymbol{\xi_{ij}}$ where

$$\boldsymbol{\xi}_{ij} = \boldsymbol{x}_j - \boldsymbol{x}_i. \tag{2.1}$$

These interactions are limited to a range called the horizon δ and nodes $\boldsymbol{x_j}$ that are connected to $\boldsymbol{x_i}$ are called the family of $\boldsymbol{x_i}$, $\boldsymbol{H_i}$.

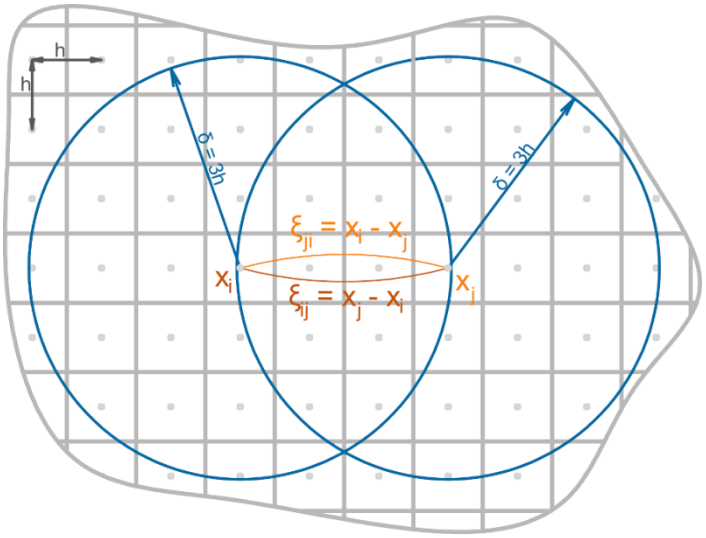

Figure 2.1. A discretized two-dimensional PD body B. Only two bonds – $\boldsymbol{\xi}_{ij}$ and $\boldsymbol{\xi}_{ji}$ – are showed. Both are showed curved to avoid overlapping.

Peridynamic theory was first introduced in its bond-based form [21], which assumes that each bond connected to $\boldsymbol{x_i}$ responds independently of all others. This form is limited to Poisson's ratio value of $\nu = 0.25$ for 3D bodies, it can't distinguish between deviatoric and volumetric deformations, therefore, doesn't allow plastic incompressibility. In 2007 peridynamic theory was greatly expanded by the introduction of its state-based form [22]. It allows interdependencies between bonds, thus removing previously mentioned limitations. Only the state-based form is used in this thesis.

When a body deforms, node $\boldsymbol{x}_i$ experiences displacement $\boldsymbol{u}_i$ and moves to its deformed position $\boldsymbol{y}_i = \boldsymbol{x}_i + \boldsymbol{u}_i$. The bond in the deformed configuration is $\boldsymbol{y}_j - \boldsymbol{y}_i$. This deformation creates a bond force density vector $\boldsymbol{t}_{ij}$ that depends on the collective deformation of all nodes in H_i and an opposite bond force density vector $\boldsymbol{t}_{ji}$ that depends on the collective deformation of H_j. Bond forces are force densities (force per volume), not stresses (force per area), because in peridynamics each node describes some volume rather than some area as in the classical continuum mechanics theory.

The bond deformation vectors for each bond in a family H_i are stored in an infinite-dimensional array called the deformation state

$$\boldsymbol{Y}_i = \begin{Bmatrix} \boldsymbol{y}_1 - \boldsymbol{y}_i \\ \vdots \\ \boldsymbol{y}_n - \boldsymbol{y}_i \end{Bmatrix}. \tag{2.2}$$

The deformation of a bond $\boldsymbol{\xi}_{ij} = \boldsymbol{x}_j - \boldsymbol{x}_i$ in a deformation state $\boldsymbol{Y}_i$ is by convention referred to using $\langle \cdot \rangle$ brackets:

$$\boldsymbol{Y}_i\langle \boldsymbol{x}_j - \boldsymbol{x}_i \rangle = \boldsymbol{Y}_i\langle \boldsymbol{\xi} \rangle = \boldsymbol{y}_j - \boldsymbol{y}_i. \tag{2.3}$$

The same notation is used also for other states when referring to the value for an individual bond.

Similarly, the force state $\boldsymbol{T}_i$ at particle $\boldsymbol{x}_i$ associates with each bond in a family H_i a force density vector $\boldsymbol{t}_{ij}$:

$$\boldsymbol{T}_i = \begin{Bmatrix} \boldsymbol{t}_{i1} \\ \vdots \\ \boldsymbol{t}_{in} \end{Bmatrix}, \tag{2.4}$$

and

$$\boldsymbol{T}_i\langle \boldsymbol{x}_j - \boldsymbol{x}_i \rangle = \boldsymbol{T}_i\langle \xi \rangle = \boldsymbol{t}_{ij}. \tag{2.5}$$

Then the peridynamic equation of motion in the integral form at some time t is

$$\rho_i \ddot{\boldsymbol{u}}_i = \int_{\boldsymbol{H}_i} \left(\boldsymbol{T}_i\langle \boldsymbol{x}_j - \boldsymbol{x}_i \rangle - \boldsymbol{T}_j\langle \boldsymbol{x}_i - \boldsymbol{x}_j \rangle \right) dV_j + \boldsymbol{b}_i, \tag{2.6}$$

where ρ_i – density,

$\ddot{\boldsymbol{u}}_i$ – acceleration,

$\boldsymbol{b}_i$ – external force density.

The PD equation of motion doesn't contain any spatial derivatives, therefore, boundary conditions aren't necessary for the solution, however, they are required to solve many practical problems. Moreover, in PD boundary conditions are applied to a layer of particles under the surface of a body B rather than to smooth segments of the body's boundaries or single points

in the body, as in the classical theory. This means that forces acting on the body's surface must also be applied to some volume under the surface as external force density $\boldsymbol{b}$, which has the dimensions of force per volume. Similarly, displacement and velocity boundary conditions must also be prescribed to some boundary layer. Macek and Silling [68] suggested that the thickness of the boundary layer should be taken equal to the horizon δ.

The bond force density vectors are computed using bond deformations:

$$\boldsymbol{T}_i = \boldsymbol{T}(\boldsymbol{Y}_i), \tag{2.7}$$

where $\boldsymbol{T}(\boldsymbol{Y}_i)$ is a state-valued function of a state – a material model. Force states are analogous to stress tensors at a point in the classical continuum mechanics theory.

The PD strain energy density W_i depends on the deformation of H_i:

$$W_i = W(\boldsymbol{Y}_i). \tag{2.8}$$

But the total stored energy E is distributed among all nodes in a body B according to the deformation of each node's family H_i:

$$E = \int_B W_i dV_i = \int_B W(\boldsymbol{Y}_i) dV_i\,. \tag{2.9}$$

Elastic state-based material models can be derived by equating strain energies in PD and the classical theory.

State-based peridynamics differ between two kinds of materials – ordinary, in which the bond force density vector $\boldsymbol{T}\langle\xi\rangle$ is always parallel to the deformed bond $\boldsymbol{Y}\langle\xi\rangle$, and non-ordinary were vectors are not necessarily parallel.

A material model, in case of an ordinary material, must always take the form of

$$\boldsymbol{T} = g\langle\boldsymbol{\xi}\rangle\boldsymbol{Y}\langle\boldsymbol{\xi}\rangle, \tag{2.10}$$

where $g\langle\boldsymbol{\xi}\rangle$ – a scalar-valued state, because the bond forces are always parallel to the deformed bonds. The simplest ordinary state-based model for solids is the linear peridynamic solid (LPS) introduced in [22]:

$$\boldsymbol{T}\langle\boldsymbol{\xi}\rangle = \left(\frac{3k\theta\omega\langle\boldsymbol{\xi}\rangle|\boldsymbol{\xi}|}{m} + \frac{15\mu}{m}\omega\langle\boldsymbol{\xi}\rangle e^d\langle\boldsymbol{\xi}\rangle\right)\boldsymbol{M}, \tag{2.11}$$

where k – shear modulus,

θ – dilatation,

ω – influence function,

m – weighted volume,

μ – shear modulus,

e^d – deviatoric extension state,

$\boldsymbol{M} = \frac{\boldsymbol{Y}\langle\xi\rangle}{|\boldsymbol{Y}\langle\xi\rangle|}$ – a unit vector.

Non-ordinary state-based materials, for which the force density vector $\boldsymbol{T}\langle\boldsymbol{\xi}\rangle$ is not necessarily parallel to the deformed bond $\boldsymbol{Y}\langle\boldsymbol{\xi}\rangle$, will not be discussed here, because they are not used in the thesis. However, they have been discussed by several authors [69–73].

Contribution of a bond to the force density at a node $\boldsymbol{x}_i$ can be weighed using an influence function ω_i. They were introduced in [22] , and their role have been further explored in [74,75]. The value of an influence function can depend on the length, direction or other bond properties. It can also be used to introduce damage – remove interaction between two nodes by setting the influence function to 0 i.e. break the bond, when some damage criterion is reached.

The simplest damage criterion could be the critical stretch, in which a bond breaks when it's stretched past some critical value s_c:

$$\omega(\xi) = \begin{cases} 1 & , \quad if\ s_{ij} < s_c \\ 0 & , \quad if\ s_{ij} \geq s_c \end{cases}, \tag{2.12}$$

where s_c – critical bond stretch,

s_{ij} – current bond stretch:

$$s_{ij} = \frac{|\boldsymbol{y}_j - \boldsymbol{y}_i| - |\boldsymbol{x}_j - \boldsymbol{x}_i|}{|\boldsymbol{x}_j - \boldsymbol{x}_i|} = \frac{|\boldsymbol{Y}\langle\boldsymbol{\xi}_{ij}\rangle| - |\boldsymbol{\xi}_{ij}|}{|\boldsymbol{\xi}_{ij}|} \tag{2.13}$$

As bonds are broken, a decreasing number of bonds have to carry the same load leading to increased bond stretch and, therefore, more damage. When the number of unbroken bonds becomes too low to carry the applied load, cracks grow rapidly leading to catastrophic failure.

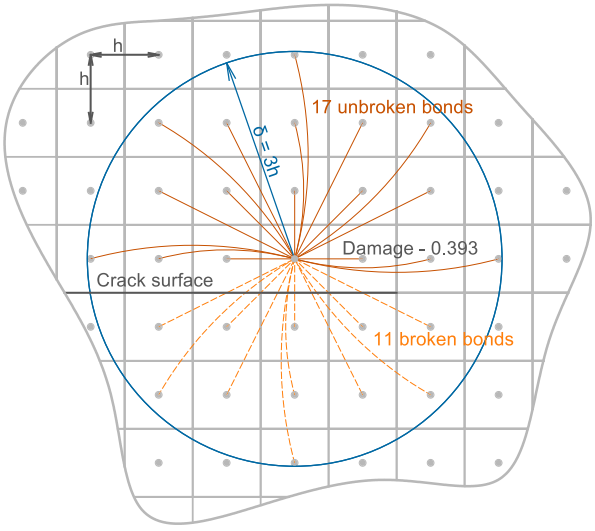

Figure 2.2. A discretized two-dimensional PD body B with a crack. Some bonds are showed curved to avoid overlapping.

Then the damage at a node can be defined as a ratio between the broken and the initial number of bonds [76], for illustration please see figure 2.2:

$$\phi(\boldsymbol{x}_i) = 1 - \frac{\int_{H_{\boldsymbol{x}_i}} \omega(\boldsymbol{x}_i)\, dV_{\boldsymbol{x}_j}}{\int_{H_{\boldsymbol{x}_i}} dV_{\boldsymbol{x}_j}}. \tag{2.14}$$

Other researchers have proposed other damage models, for example: based on critical energy density [77], fatigue damage models [47,78], continuum damage models incorporated in PD [79], damage model through phase field theory [80].

2.2 Modal analysis

In both continuum mechanics theory and peridynamic theory a body *B* consists of an infinite number of particles $\boldsymbol{x}_i$ that have some density ρ_i. When some force acts upon a body *B*, it experiences some deformation and displacement. For a basic problem with a linear elastic material that obeys Hooke's Law, the generalized equation of motion of an n degree of freedom (DOF) system in a matrix form is

$$\boldsymbol{M}\ddot{\boldsymbol{u}} + \boldsymbol{C}\dot{\boldsymbol{u}} + \boldsymbol{K}\boldsymbol{u} = \boldsymbol{F}, \tag{2.15}$$

where $\boldsymbol{M}$ – n×n mass matrix,

$\boldsymbol{C}$ – n×n damping matrix,

$\boldsymbol{K}$ – n×n stiffness matrix,

$\ddot{\boldsymbol{u}}, \dot{\boldsymbol{u}}, \boldsymbol{u}$ – n×1 acceleration, velocity and displacement vectors respectively,

$\boldsymbol{F}$ - n×1 force vector.

Equation (2.15) is a quadratic eigenvalue problem, however, when damping of a system is small it is commonly ignored. Then (2.15) can be rewritten as:

$$\boldsymbol{M}\ddot{\boldsymbol{u}} + \boldsymbol{K}\boldsymbol{u} = \boldsymbol{F}, \tag{2.16}$$

The mass matrix $\boldsymbol{M}$ describes the mass of each node in a body and the stiffness matrix $\boldsymbol{K}$ describes the stiffness that a node $\boldsymbol{x}_i$ exerts on a node $\boldsymbol{x}_j$ and vice versa. The construction of these matrices will be described in chapter 3 Computational implementation and optimization.

Free vibrations of a multiple DOF system are initiated by the presence of an initial potential or kinetic energy. If a system is undamped there are no dissipative mechanisms and it is expected that the free vibrations are synchronous in that all independent variables execute motion with the same time-dependent behavior. Thus, when free vibrations at a single frequency are initiated for a particular system, the ratio of any two dependent variables is independent of time. This leads to the normal-mode solution

$$\boldsymbol{u}(t) = \boldsymbol{x}e^{i\omega t}, \tag{2.17}$$

where ω – the frequency of vibration,

$\boldsymbol{x}$ – an n-dimensional vector called a mode shape.

When the values of ω are such that (2.17) is satisfied, they are called modal frequencies and each modal frequency has a corresponding mode shape. Equation (2.16) is linear and homogenous, so its general solution is a linear superposition over all possible modes. Substituting (2.17) into (2.16) yields

$$(-\omega^2 \boldsymbol{M}\boldsymbol{x} + \boldsymbol{K}\boldsymbol{x})e^{i\omega t} = \boldsymbol{0}. \tag{2.18}$$

Since $e^{i\omega t} \neq 0$ for any real value of t, rearranging terms and substituting ω^2 for λ leads to

$$\boldsymbol{K}\boldsymbol{x} = \lambda \boldsymbol{M}\boldsymbol{x}. \tag{2.19}$$

In linear algebra (2.19) is called the generalized eigenvalue problem and λ, $\boldsymbol{x}$ values that satisfy this equality are called eigenvalues and eigenvectors respectively. Eigenvectors $\boldsymbol{x}$ are also mode shapes that show displacement of each node in an n-DOF system. Eigenvalues λ are related to modal frequencies f through

$$f = \frac{+\sqrt{\lambda}}{2\pi}. \tag{2.20}$$

2.3 Linear algebra

A matrix $\boldsymbol{A}$ is a rectangular array of numbers arranged in m rows and n columns. Its dimensions are commonly written as $m \times n$. A vector is a $m \times 1$ matrix and a matrix that has as many rows as columns i.e. $m = n$ is called a square matrix. Each independent element of a matrix is denoted by a_{ij}, where i and j denotes row and column index respectively. A square matrix element whose row index is equal to its column index – $a_{11}, a_{22} \ldots a_{nn}$ – are said to be on the main diagonal. And a matrix $\boldsymbol{D}$ is called a diagonal matrix if all elements not on its main diagonal are zero

$$d_{ij} = 0 \; if \; i \neq j. \tag{2.20}$$

Moreover, the sum of the elements on a $n \times n$ square matrix's $\boldsymbol{A}$ main diagonal is call the trace of $\boldsymbol{A}$**:**

$$tr(\boldsymbol{A}) = \sum_{i=1}^{n} a_{ii}\,. \tag{2.21}$$

A band matrix $\boldsymbol{B}$ is a matrix whose non-zero elements are confined to a diagonal band, comprising the main diagonal and zero or more diagonals on either side

$$b_{ij} = 0, if \; |i - j| > k, \tag{2.22}$$

where k – bandwidth. For example bandwidth of a diagonal matrix $k = 0$, but for a 5×5 tridiagonal matrix

$$B = \begin{bmatrix} b_{11} & b_{12} & 0 & 0 & 0 \\ b_{21} & b_{22} & b_{23} & 0 & 0 \\ 0 & b_{32} & b_{33} & b_{34} & 0 \\ 0 & 0 & b_{43} & b_{44} & b_{45} \\ 0 & 0 & 0 & b_{54} & b_{55} \end{bmatrix}. \quad (2.23)$$

bandwidth $k = 1$.

Furthermore, when a band is narrow compared to the size of a matrix itself (most of the elements are equal to zero) such a matrix is called sparse. Conversely, a matrix with many non-zero elements is called dense. It is hard to define how many zeros should be in a matrix before it's considered sparse. However, the most common definition is offered in [81], where it is said that "We shall refer to a matrix as dense if the percentage of zero elements or its distribution is such as to make it uneconomic to take advantage of their presence." and it is understood that the opposite is a sparse matrix.

Several special matrices are used in the thesis. An identity matrix

$$\boldsymbol{I} = \begin{bmatrix} 1 & \cdots & 0 \\ \vdots & \ddots & \vdots \\ 0 & \cdots & 1 \end{bmatrix} \quad (2.24)$$

is a matrix with ones on the main diagonal and zeros everywhere else. The inverse of a square matrix $\boldsymbol{A}$ is a matrix $\boldsymbol{A^{-1}}$ such that

$$\boldsymbol{A A^{-1}} = \boldsymbol{I}. \quad (2.25)$$

And a matrix $\boldsymbol{A}$ is called singular, if it doesn't have a matrix inverse $\boldsymbol{A^{-1}}$. The transpose of a matrix $\boldsymbol{A}$ is a matrix $\boldsymbol{A^T}$, whose j-th column is an i-th row of a matrix $\boldsymbol{A}$

$$\boldsymbol{A}^T_{ij} = \boldsymbol{A}_{ji}. \quad (2.26)$$

A matrix $\boldsymbol{A}$ is called symmetric if it is equal to its transpose $\boldsymbol{A^T}$

$$\boldsymbol{A} = \boldsymbol{A^T}. \quad (2.27)$$

An equation

$$\boldsymbol{A x} = \lambda \boldsymbol{x}, \quad (2.28)$$

where $\boldsymbol{A}$ – n × n square matrix,

$\boldsymbol{x}$ – eigenvector,

λ – eigenvalue

is called a standard eigenvalue problem. A pair of λ and $\boldsymbol{x}$ for which (2.28) holds is called an eigenpair.

The spectrum of a square $n \times n$ matrix $\boldsymbol{A}$ is the set of its eigenvalues and its spectral radius is the largest absolute value of its eigenvalues. The largest and the smallest eigenvalue is called exterior eigenvalues, but the rest are called interior eigenvalues. Furthermore, $\boldsymbol{A}$ has as many

eigenvalues λ_n as it has rows. The sum of the n eigenvalues equals the sum of n diagonal entries:

$$tr(\boldsymbol{A}) = \sum_{i=1}^{n} \lambda_i = \sum_{i=1}^{n} a_{ii} \tag{2.29}$$

and the product of the n eigenvalues equals the determinant of $\boldsymbol{A}$

$$det(\boldsymbol{A}) = \prod_{i=1}^{n} \lambda_i \,. \tag{2.30}$$

Commonly in engineering, an eigenvalue problem with not one but two matrices, called a generalized eigenvalue problem, is used

$$\boldsymbol{Ax} = \lambda \boldsymbol{Bx}, \tag{2.31}$$

where $\boldsymbol{B}$ – n × n square matrix. When $\boldsymbol{B} = \boldsymbol{I}$, a generalized eigenvalue problem becomes a standard eigenvalue problem.

When matrices $\boldsymbol{A}$ and $\boldsymbol{B}$ are symmetric and their elements are real numbers, then their eigenvalues are also real numbers. However, a PD stiffness matrix $\boldsymbol{K}$ is commonly non-symmetric, therefore, its eigenvalue will be a complex number $a + ib$, where $i^2 = -1$ is the imaginary unit. A complex conjugate of $a + ib$ is the number $a - ib$. The sign of the imaginary part is reversed. Commonly it is denoted with a star or a bar: $a - ib = (a + ib)^* = \overline{a + \imath b}$. Moreover, a real number is a complex number with $b = 0$.

For complex matrices, an equivalent of a transpose is called a conjugate transpose and written as

$$\boldsymbol{A}^H = \overline{\boldsymbol{A}}^T. \tag{2.32}$$

Its entries $A_{ij}^H = \overline{A_{j\imath}}$. Matrices that equal their conjugate transpose are called hermitian, with the opposite being non-hermitian. Since a real number is a complex number with $b = 0$, symmetric matrices are also hermitian.

In physics and engineering, linear algebra is used to solve systems of equations, most commonly either $\boldsymbol{Ax} = \boldsymbol{b}$ or $\boldsymbol{Ax} = \lambda \boldsymbol{Bx}$. Methods for solving for $\boldsymbol{x}$ are either direct or iterative and computer algorithms that solve these systems of equations are called solvers. An excellent overview of different eigenvalue problems and methods for solving them is presented in [82] and for detailed information on different iterative solvers, the author recommends [83].

Direct methods will reach an exact solution, if it exists, in some finite number of steps, however, the entire matrix is generally needed to be stored in computer memory. When a matrix is large the finite number of steps and the required computer memory will also be large.

Contrary, iterative methods obtain an approximation of $\boldsymbol{x}$ that is often good enough for practical applications. Moreover, they don't require the whole matrix to be stored in computer memory. Iterative methods start from some initial guess $\boldsymbol{x_0}$ and in each step update the old

guess $\boldsymbol{x_n}$ to produce a new guess $\boldsymbol{x_{n+1}}$ that is slightly closer to the exact solution. When the difference between $\boldsymbol{x_n}$ and $\boldsymbol{x_{n+1}}$ (the residual) falls below some specified tolerance value, the computation is stopped and it is said that the result has converged.

Matrices in peridynamics commonly are large. 1 875 000 × 1 875 000 is the size of the largest matrix used in this thesis, therefore, only iterative solvers were used.

Preconditioning is a technique used in iterative solvers to modify the original problem

$$\boldsymbol{Ax = b} \tag{2.33}$$

in such a way that an equivalent problem

$$\boldsymbol{P^{-1}Ax = P^{-1}b}, \tag{2.34}$$

where $\boldsymbol{P}$ – a preconditioner, for which the iterative solver converges faster is obtained. Preconditioner $\boldsymbol{P}$ needs to be chosen such that it is easy to compute and reduces the number of iterations needed for the iterative solver to converge. (2.34) can be rewritten as

$$\boldsymbol{P^{-1}(Ax - b)} = 0. \tag{2.35}$$

This is called left preconditioning because it applies preconditioner to the left of a matrix $\boldsymbol{A}$. The original problem in (2.33) can also be rewritten as

$$\boldsymbol{AP^{-1}Px = b}. \tag{2.36}$$

Then (2.36) is solved by solving

$$\boldsymbol{AP^{-1}y = b}. \tag{2.37}$$

for $\boldsymbol{y}$ and

$$\boldsymbol{Px = y} \tag{2.38}$$

for $\boldsymbol{x}$. This is called the right preconditioning, because preconditioner $\boldsymbol{P}$ is applied to the right of the matrix $\boldsymbol{A}$.

Preconditioning is also used for eigenvalue problems. In cases when eigenvalues are not well separated or are located in the interior of the eigenvalue spectrum eigenvalue, a solver – if it converges at all – may need many steps to generate acceptable approximation. Therefore, a spectral transformation can be used. It transforms eigenvalue spectrum such that poorly separated eigenvalues are well separated and an interior eigenvalue lies on the exterior.

The best known is the so-called shift-invert technique. A generalized eigenvalue problem in (2.31) is transformed into

$$\boldsymbol{Cx} = \theta\boldsymbol{x}, \tag{2.39}$$

where both C and θ are substitutions

$$\boldsymbol{C} = (\boldsymbol{A} - \sigma \boldsymbol{B})^{-1} \boldsymbol{B} \tag{2.40}$$

and

$$\theta = (\lambda - \sigma^2)^{-1}, \tag{2.41}$$

where σ – shift value. (2.39) is now a simple eigenvalue problem. When a shift σ is chosen well, eigenvalues of matrix $\boldsymbol{C}$ are better separated than those of $\boldsymbol{A}$, which leads to faster convergence. If a solver converged, then obtained eigenvectors $\boldsymbol{x}$ are the same as eigenvectors for the original problem, but eigenvalues need to be reinverted and shifted back:

$$\lambda = \frac{1}{\theta} + \sigma^2. \tag{2.42}$$

Using this transformation, the eigenvalue problem is solved using two solvers – a linear solver for the substitution $\boldsymbol{C}$ in (2.40) and an eigensolver for the eigenproblem in (2.39). Solvers themselves will not be discussed here, because the development of solvers themselves is beyond the scope of this thesis. The implementation of these solvers is described in chapter 3.1 Peridynamic implementation.

Then obtained eigenvectors $\boldsymbol{x}$ are the mode shapes of the original problem in (2.31), but modal frequencies f are calculated from eigenvalues that have to be reinverted and shifted back so insert (2.42) into (2.20):

$$f = \frac{+\sqrt{\frac{1}{\theta} + \sigma^2}}{2\pi}. \tag{2.50}$$

3 COMPUTATIONAL IMPLEMENTATION AND OPTIMIZATION

This chapter describes the peridynamic implementation, followed by the finite-element implementation, and the optimization of the PD modal solver parameters.

PD simulations were run on the computing cluster Vasara at Riga Technical University. Different numbers of Dell EMC PowerEdge R640 nodes each with 2 x Intel(R) Xeon(R) Gold 6154 3.00 GHz CPUs with 36 cores were used. Each node had 348 GB maximum available RAM and a 240GB SSD. They were connected through an Infiniband EDR 100 Gb/s connection. The cluster ran Centos 7.5 operating system and used Torque 6.1.1.1 resource manager. The modal solver was implemented by extending Peridigm 1.5.0, which at the time of writing is available at https://github.com/peridigm/peridigm.

3.1 Peridynamic implementation

Modal Solver

During the research for and the development of this thesis it became clear that solving PD modal problems poses significant challenges:

- First, peridynamic stiffness matrices are non-symmetric, thus require non-Hermitian solvers, whereas comparable FE problems would have symmetric stiffness matrices. Generally, non-symmetric matrices take up more computer memory, because the whole matrix rather than only half needs to be stored. Non-symmetric matrices may not be diagonalizable, which excludes common matrix factorization methods such as Cholesky or LDL factorizations. Another complication is that the eigenvalues of non-symmetric problems need not be real, so solutions involve working with complex numbers.
- Second, a node in PD is generally connected to more nodes than a node in FE analyses so the stiffness matrices contain more non-zeros and their bandwidth is wider. Usually, only the non-zero elements of a matrix are stored in the computer memory and it is assumed that every element that isn't stored is zero. As the number of non-zero elements increases, the required memory also increases. Moreover, more non-zeros lead to poorer convergence, because there are more values to consider.
- Third, for practical problems, PD models consist of a large number of nodes, possibly in the millions. The node size needs to be small otherwise, as the bonds between nodes break, the crack tip would advance in large jumps, which poorly describe the behavior of a crack. Furthermore, reasonable mesh convergence can be achieved only with large models. Additionally, if the node size is large the boundary conditions can have a disproportionate effect on the behavior of the model, thus Saint-Venant's principle will not be met.

The large number of non-zeros in the stiffness matrix can be reduced by setting the displacement of a set of nodes to zero thus simulating a support. Matrix entries for those nodes would be zero and generally more zero entries in a stiffness matrix lead to easier convergence.

However, the free-free boundary conditions, which allow the test specimen to move in all directions, are often used in modal testing. Therefore, the author wished to implement a solver that can solve the problem regardless of the chosen support conditions.

Due to large computational cost, peridynamic simulations are frequently run on computing clusters. In order to take advantage of the available computing resources, the solver requires an efficient massively-parallel computational implementation. This limits the number of feasible programming languages and computing libraries.

The modal solver was implemented in open-source peridynamics code Peridigm [84,85], which was chosen because it provides an easily extensible, robust framework for peridynamic computation. Since it's open-source software, the author could later contribute the written code making this analysis available to other researchers and engineers. Moreover, as Peridigm already implements quasi-static and explicit solvers, several parts – material models, stiffness matrix creation routines, discretization management, and boundary conditions – could be reused. Therefore, reducing the time spent on writing the code for a working modal solver.

Several software libraries were considered for the implementation of the modal solver – SLEPc [86], ARPACK [87], SpectrA [88], and Trilinos [89]. Out of these four, the Trilinos library was chosen, because

- Peridigm is already built using several packages from Trilinos, so further integration was easier;
- Trilinos is designed for massively-parallel computations making it well suited for running on a computing cluster;
- All three - linear solvers, eigensolvers and preconditioners – are available in Trilinos, therefore only one library needs to be used for implementation.

Trilinos is split into several packages, where each package is a self-contained, independent piece of software with its own set of requirements and a variety of ways for package interaction are available. Peridigm is built and the modal solver was implemented using several of them, but only those that were used to implement the modal solver are mentioned here:

- Epetra – defines basic distributed parallel matrix classes for basic matrix and vector operations that are used by all Trilinos packages [67];
- Teuchos – a collection of classes for dynamic memory management and communicating hierarchical lists of parameters [90];
- Ifpack – package for object-oriented algebraic preconditioners for the solution of preconditioned iterative solvers [91];
- Belos – iterative linear solver package for both Hermitian and non-hermitian problems [92];
- Anasazi – package for large-scale parallel eigenvalue and eigenvector solvers for both symmetric and non-symmetric problems [93,94].

The modal problem was solved using the shift-invert technique, in which the eigenvalue spectrum of a generalized eigenvalue problem is transformed inverted and shifted by σ^2 so that it's easier to solve. Details of this transformation are presented in chapter 2.3 Linear algebra.

All solvers needed to be applicable to non-hermitian problems, because the peridynamic stiffness matrix is non-symmetric. Two eigensolvers - block Krylov-Schur eigensolver [95,96]

and Generalized-Davidson eigensolver [97] – were considered. Four linear solvers – LU direct solver, flexible block-generalized minimum residual (GMRES) [98], block-GMRES [99], and block conjugate gradient (CG) [100] iterative solvers – were considered. And only one preconditioner – Incomplete LU (ILU) [83] – was considered. Only simulations with the combination of ILU preconditioner, flexible block-GMRES linear solver, and block Krylov-Schur eigensolver converged for the free-free case, so these three were chosen.

The behavior of solvers is controlled by several parameters that change the convergence speed and the memory use of a simulation. They can be split into four parts:

- The eigenproblem itself has two parameters:
    - Number of Frequencies – the number of eigenvalues that the eigensolver will have to find;
    - Sigma – the shift value for the shift-invert transformation.
- ILU preconditioner has three parameters:
    - ILU Drop Tolerance - preconditioner entries with magnitude less than this value will be dropped;
    - ILU Level-of-fill – only this number of entries in a row with the largest magnitude will be kept. When this parameter is large then a complete factorization will be computed, which will be very slow;
    - ILU Overlap level – number of overlapped rows among processors;
- Flexible block-GMRES solver has four parameters:
    - Linear Solver Block Size – number of right-hand sides to use simultaneously;
    - Linear Solver Number of Blocks – number of blocks to consider in a single iteration;
    - Linear Solver Max Number of Restarts – the maximum number of allowed solver restarts;
    - Linear Solver Tolerance – relative convergence tolerance for the linear solver;
- Block Krylov-Schur eigensolver has four parameters:
    - Eigensolver Block Size - number of right-hand sides to use simultaneously;
    - Eigensolver Number of Blocks – number of blocks to consider in a single iteration;
    - Eigensolver Max Restarts – the maximum number of allowed solver restarts;
    - Eigensolver Tolerance – relative convergence tolerance for the eigensolver.

Peridynamic model

A simple rectangular plate structure was chosen to verify and validate peridynamic results. Common real-life structures would have a more complex shape, however, this research concerns itself with development and testing of a viable peridynamic modal analysis approach not simulations of any real-life structures. For that purpose, a plate shape is sufficient. Furthermore, it will be easy to create FE and PD computational models and rectangular test specimens for the experimental analysis can be manufactured easily.

A good validation and verification case would include several possible outcomes. For this study, those would be several different mode shapes. Therefore, a rectangular plate was a good choice, because bending, transversal bending, torsional, and in-plane bending modes were present.

Peridigm doesn't have a built-in mesh generator. Instead, mesh files must be supplied by the user. Its mesh files are text files with each line describing a single node. Data must be separated in columns, where values – x, y, z coordinate, block ID, volume – must be stored in columns 1 through 5. A block is a group of nodes to which some material model, damage model, and contact model are prescribed. The model size was 0.10×0.05×0.008 m and an example is shown in figure 3.1.

Peridigm uses a meshfree discretization [76], in which a node describes some volume around it but isn't limited by any geometrical constraints. For example, nodes of a single cubic solid element in the FE analysis must have six faces between them and these faces must not intercross. In meshfree discretization, nodes have no such geometrical constraints.

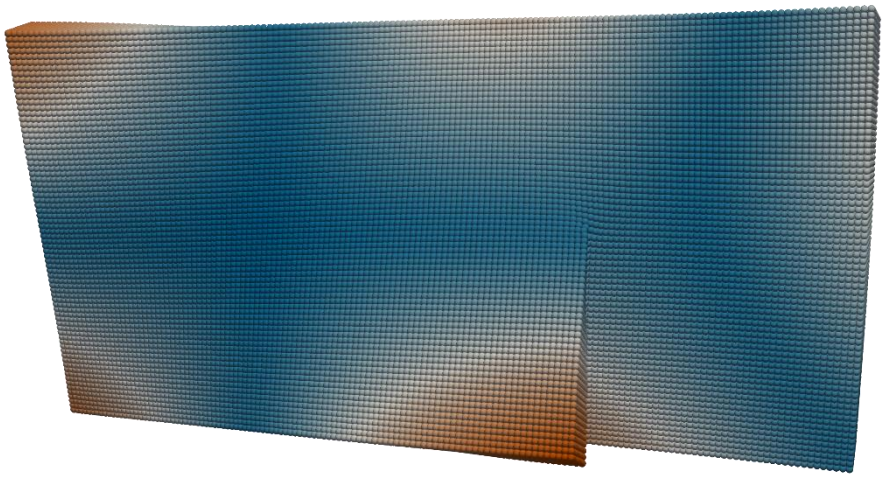

Figure 3.1. A 3D peridynamic model with a 25 mm deep crack showing the 2nd torsional mode.

Four different models with 40 000, 135 000, 320 000, 625 000 nodes were used. The idea was to have the same node spacing h in all directions i.e. cubic nodes. The nodal spacing was 0.001 m, 0.000667 m, 0.0005 m and 0.0004 m respectively. The horizon is commonly taken as some multiple of the nodal spacing h. In 3D it is rarely taken larger than $3h$ or $4h$ because the number of neighbors and, therefore, the computational cost increases rapidly with an increasing horizon. In this thesis the horizon values of $\sqrt{2}h, 2h, 3h, 4h$ are used. All considered combinations of the number of nodes, nodal spacing, and the horizon are presented in table 3.1.

Simulations used Linear Peridynamic Solid (LPS) material model, which is the PD equivalent of an elastic material model in the continuum mechanics. No boundary conditions were applied to simulate free-free test conditions. The material properties were:

- elastic modulus – 5.35 GPa;
- Poisson's ratio – 0.33;
- density – 1200 kg/m^3.

Table 3.1.

All PD horizon-mesh combinations for convergence studies.

Nodes in the model	Nodal spacing (h), m	Horizon	Horizon, m
40000	0.001	$\sqrt{2}h$	0.03162
40000	0.001	$2h$	0.00200
40000	0.001	$3h$	0.00300
40000	0.001	$4h$	0.00400
135000	0.000667	$\sqrt{2}h$	0.02582
135000	0.000667	$2h$	0.00133
135000	0.000667	$3h$	0.00200
135000	0.000667	$4h$	0.00267
320000	0.0005	$\sqrt{2}h$	0.02236
320000	0.0005	$2h$	0.00100
320000	0.0005	$3h$	0.00150
320000	0.0005	$4h$	0.00200
625000	0.0004	$\sqrt{2}h$	0.02000
625000	0.0004	$2h$	0.00080
625000	0.0004	$3h$	0.00120
625000	0.0004	$4h$	0.00160

Cracks in a model were created by specifying a crack plane and breaking any bond that crosses this plane. Crack configurations and locations are presented in chapter 4.2 Specimens for modal analysis.

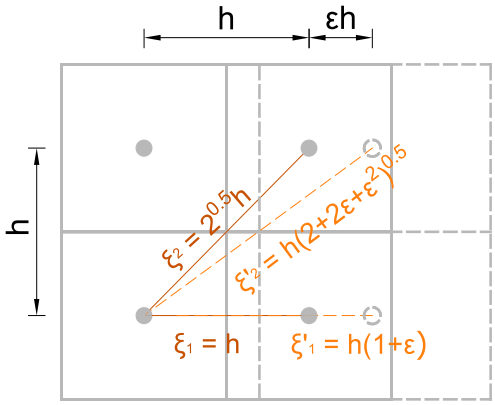

Figure 3.2. A discretized 2D peridynamic model consisting of four nodes. When the object is deformed in the horizontal direction, the bond strain is linear for bonds that are parallel or perpendicular to the direction of the deformation e.g. ξ_1, but nonlinear for all other bonds e.g. ξ_2.

It must be noted that even if the PD material model is linear a nonlinear problem will have to be solved. A linear PD material model is proportional to bond strain, but not necessarily the global strain. Please see figure 3.2 for an illustration. An object is discretized with four nodes and two bonds – ξ_1 and ξ_2 – are showed. When it is linearly deformed in the horizontal direction, some strain ε arises and distance in the horizontal direction between two nodes

increases from h to $h(1+\varepsilon)$. Length of ξ_1 increases linearly, because its direction is parallel to the deformation. However, the length of ξ_2 increases nonlinearly from $\sqrt{2}h$ to $h\sqrt{2+2\varepsilon+\varepsilon^2}$ even though the global strain is linear.

The first 12 modes were computed. The first six were the rigid-body-motion modes, so only the next six were compared with the FE and the experimental results. A total of 144 simulations were made – 16 for each of nine crack configurations. Obtained results are presented and discussed in chapter 5 Verification and validation of peridynamic modal analysis.

Stiffness and mass matrices

The tangent stiffness matrix in Peridigm is built using a central-difference scheme and the exact algorithm stiffness matrix is presented in [84] but it is repeated here for completeness. Tangent stiffness matrix in its discreet form is approximated using a central-difference scheme:

$$K_{ij} \approx \frac{f_i^{int}(\boldsymbol{u}+\boldsymbol{\epsilon}^j) - f_i^{int}(\boldsymbol{u}-\boldsymbol{\epsilon}^j)}{2\epsilon}, \tag{3.1}$$

where K_{ij} – an entry in the stiffness matrix,

f_i^{int} – a component of the internal force vector,

$\boldsymbol{u}$ – displacement vector,

$\boldsymbol{\epsilon}^j$ – a vector containing a single non-zero entry, ϵ, at the position corresponding to the k-th degree of freedom (DOF) in the discretization (perturbation vector).

The tangent stiffness matrix is built by perturbing individual DOFs and summing the resulting global force vector values. The force state is evaluated under a positive perturbation $\epsilon+$ and a negative perturbation $\epsilon-$ obtaining corresponding force densities $\mathbf{T}^{\epsilon+}\langle \boldsymbol{x}_j - \boldsymbol{x}_i\rangle$ and $\mathbf{T}^{\epsilon-}\langle \boldsymbol{x}_j - \boldsymbol{x}_i\rangle$ in a bond $\langle \boldsymbol{x}_j - \boldsymbol{x}_i\rangle$. Then the force densities at a node $\boldsymbol{x}_i$ are summed separately at $\epsilon+$ and $\epsilon-$ states, resulting in the internal force vectors $f_i^{int}(\boldsymbol{u}+\boldsymbol{\epsilon}^k)$ and $f_i^{int}(\boldsymbol{u}-\boldsymbol{\epsilon}^k)$. Stiffness at a node $\boldsymbol{x}_i$ from perturbation of the k-th degree of freedom is computed as the difference between evaluated internal force vectors divided by double the perturbation length.

The default magnitude of the perturbation length is chosen so that it's small relative to the discretization, but large enough so that machine precision is not a significant factor:

$$\epsilon = 1.0e^{-6} \times h, \tag{3.2}$$

where ϵ – perturbation length,

h - nodal spacing.

Peridynamic stiffness matrices are often non-symmetrical, because even though two nodes $\boldsymbol{x}_i$ and $\boldsymbol{x}_j$ are connected by the same in magnitude but opposite bonds $\langle \boldsymbol{x}_j - \boldsymbol{x}_i\rangle$ and $\langle \boldsymbol{x}_i - \boldsymbol{x}_j\rangle$, the force densities in them are influenced by different neighborhoods i.e. $H_{\boldsymbol{x}_i}$ and $H_{\boldsymbol{x}_j}$. Because of the non-symmetrical stiffness matrix, solvers for non-Hermitian problems must be used.

Additionally, PD stiffness matrices are often denser than FE stiffness matrices for the same problems, because in FE analysis a node is only connected to its nearest neighbors, but in PD a node is connected to all nodes within its horizon, which can stretch beyond the closest

neighbors. As a result, for similar problems, a PD solution can be computationally more expensive than an FE solution.

The mass matrix describes the mass that acts on each separate DOF. In PD a node describes some amount of volume around it, therefore, the lumped mass approach is an intuitive way to build the mass matrix:

$$M_{ij} = V_i \rho_i, \tag{3.3}$$

where M_{ij} – an entry in a mass matrix $\boldsymbol{M}$,

V_i – volume described by a node $\boldsymbol{x}_i$,

ρ_i – the density of a node $\boldsymbol{x}_i$.

The peridynamic mass matrix is built by looping over all nodes, multiplying their volumes with their densities and storing them in a separate matrix. This matrix is positive and Hermitian.

3.2 Finite-element implementation

Modal analysis in the finite-element method is well understood and widely used in both research and engineering, therefore, it was a natural choice for verification of PD results. A rectangular plate model with the same measurements as the PD model was created using Ansys FE software. An elastic material model was used, and the material properties were the same as for the PD simulations. Also, its dimensions were the same as for the PD model – 0.10×0.05×0.008 m. The FE model was meshed using SOLID185 8-node cubic elements and contained 664 146 nodes. The Ansys model is shown in figure 3.3.

This kind of problem could have been modeled using shell elements, which would have been computationally less expensive, however, solid elements were chosen for two reasons:

- the author wanted FE and PD meshes to have a similar number of nodes;
- it was possible to create cracks through the depth of the FE model, which would not have been possible if the model was created using shell elements.

Cracks in the FE model were created by not connecting the nodes of solid elements on a crack plane. Such an approach is not ideal, however, it is good enough for verification purposes because as will be showed in chapter 5 the FE results agree with the experimental results well and are, therefore, reliable. Crack configurations and locations are presented in chapter 4.2 Specimens for experimental modal analysis.

Ansys offers several options for modal analyses. The Block Lanczos solver was used to solve the underlying eigenvalue problem. Nodal mass was approximated using the lumped mass method, in which mass matrix is computed assuming that the mass at a node is the mass of the object's part that is closer to that node than any other node.

The first 12 modes were computed. The first six will be rigid-body-motion modes, but the other six can be used for verification. A total of 9 simulations were made, one at reach crack configuration. The results are presented in chapter 5 Verification and validation of peridynamic modal analysis.

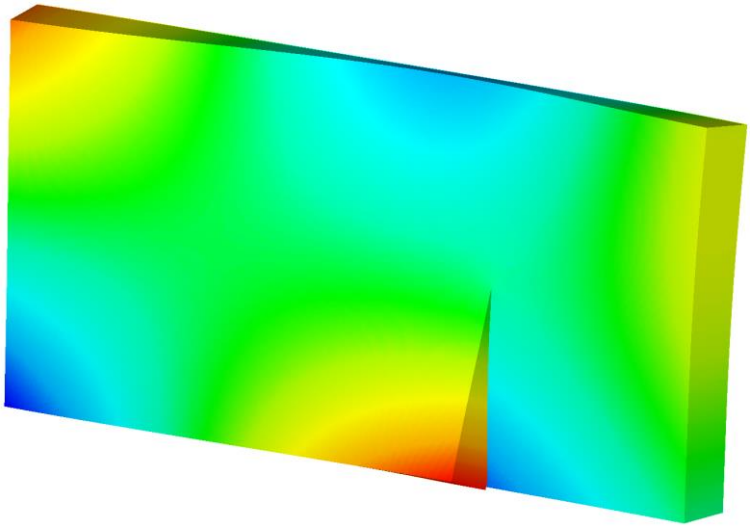

Figure 3.3. 3D finite-element model with a 25 mm deep crack showing the 2nd torsional mode.

3.3 Solver parameter optimization

Solver parameters influence the solve time, memory requirements and whether a simulation will converge at all, therefore, they need to be optimized. Optimization is a problem-dependent issue, so the values presented at the end of this chapter are for problems in this thesis. Better results can be obtained for other problems with a set of different parameter values.

Mathematical optimization is the selection of the best element, with regards to some criterion, from some set of available alternatives. Generally, that means maximizing or minimizing a real function (objective) by changing its input values (parameters) within some boundaries. In this thesis, maximum memory use and computation time are the two objectives that were optimized. Since two objectives are considered this is a multi-objective optimization problem.

Commonly, Pareto optimization is used for multi-objective optimization problems. Pareto optimality is a state of allocation of resources from which it is impossible to reallocate so as to make any one individual or preference criterion better off without making at least one individual or preference criterion worse off. This original definition was developed for use in economics. For the present case, a Pareto optimal would be such a solver parameter combination that it is impossible to change any single parameter without making either the memory use higher or the solve speed slower. Usually, a set – called a Pareto frontier – of such Pareto optimal points can be found. A mathematical definition of Pareto frontier will not be presented here, but frontiers themselves are shown in figures 3.7b through 3.10b.

The maximum amount of physical memory during runtime minus the memory used to store the stiffness matrix was used. This information was gathered from “tracejob” command that is available in the Torque resource management system. For detailed computing cluster description please see the introduction of this chapter.

Peridigm has its own built-in timer, that measures the total runtime and the time spent on different tasks, such as building stiffness matrix, creating preconditioner and solving the modal

problem. Total runtime was used for optimization because we're interested in optimal performance of the whole program not only its different parts.

Table 3.2.

Test cases and their parameters

Case	NEV	Horizon	Number of experiments	Converged	Didn't converge	Exceeded memory
A	1	$\sqrt{2}h$	180	131	15	34
B	10	$\sqrt{2}h$	150	105	7	38
C	1	$3h$	150	142	0	8
D	10	$3h$	150	124	0	26

As is common in computer experiments, there were several factors to test. Test values were selected using Latin-Hypercube sampling technique [101–103]. Four cases – named A through D – were considered. They differed by the number of eigenvalues (NEV) – 1 or 10 – and the length of the horizon – either $\delta = \sqrt{2}h$ or $\delta = 3h$. Specific values are showed in table 3.2. These values were selected to check how the number of eigenvalues required and the sparsity of the stiffness matrix change the solve speed and the required memory. The size of the stiffness matrix was 405 000×405 000, for A and B cases there were 101 371 968 non-zero elements, for C and D cases there were 787 674 132 non-zero elements. An increase of about 7.7 times. A single experiment will be referred to by its case and its number e.g. B17.

Model dimensions, material model, material properties and boundary conditions are described in chapter 3.1 Peridynamic implementation. The model was discretized with 135 000 nodes with a nodal spacing of $h = 0.000667\ m$. The horizon was set to $\delta = 0.000943001$ m for cases A and B, and $\delta = 0.002001$ m for cases C and D.

The author considered nine different parameters with their max and min values shown in table 3.3. The solver tolerances were set to $1e^{-6}$ and $1e^{-4}$ for linear solver and eigensolver respectively.

Table 3.3.

Solver parameter ranges

Factor	Min value	Max value
ILU level of fill	1	20
ILU Drop tolerance	1e-12	1e0
ILU Overlap level	0	4
Linear Solver Max Restarts	0	50
Linear Solver Number of Blocks (LSNB)	500	0.02K[a] (0.05K)[b]
Linear Solver Block Size (LSBS)	1	5
Eigensolver Max Restarts	0	50
Eigensolver Number of Blocks (ESNB)	3	5NEV[c]
Eigensolver Block Size (ESBS)	1	5NEV

a – K = 405 000 – the size of the stiffness matrix
b – 0.05K was the upper limit for A case
c – NEV – number of eigenvalues requested

The total number of simulations, converged, unconverged and the number of simulations that exceeded available memory are shown in table 3.2. In four all cases, the first 60 tests ran

with parameter values selected over a large range. Then additional points were generated in areas that were thought to include the optimal solution. Case A has more tests than the rest because a larger part of them exceeded available memory and was, therefore, killed by the operating system. For cases B, C, and D the upper limit Linear Solver Number of Blocks (LSNB) was decreased to 0.02K, so fewer experiments ended up exceeding the memory limit.

73 %, 70 %, 95 % and 83 % of all simulations converged for cases A through D respectively. For the case, A 8 % and for the case B 5 % of simulations returned unconverged, but all simulations converged for cases C and D. Some simulations exceeded the available memory – 19 %, 21 %, 4 %, 14 % for cases A, B, C, D respectively. Hereafter, only the converged cases are considered.

Preconditioner parameters should be selected to speed up the linear solver while being cheap to compute. Preconditioner creation time varied between 0.52 and 5.11 seconds with an average of 2.07. These times are short when compared to the total time that varied between 305.82 and 4088.34 seconds with an average of 759.15. The average time it takes to create a preconditioner is only 0.27% of the average total time. Therefore, the preconditioner creation time is not considered as a separate optimization objective.

Several relations between solver parameters and simulation time and memory were found, and it was also noticed that many simulations with a low number of linear solver blocks failed to converge.

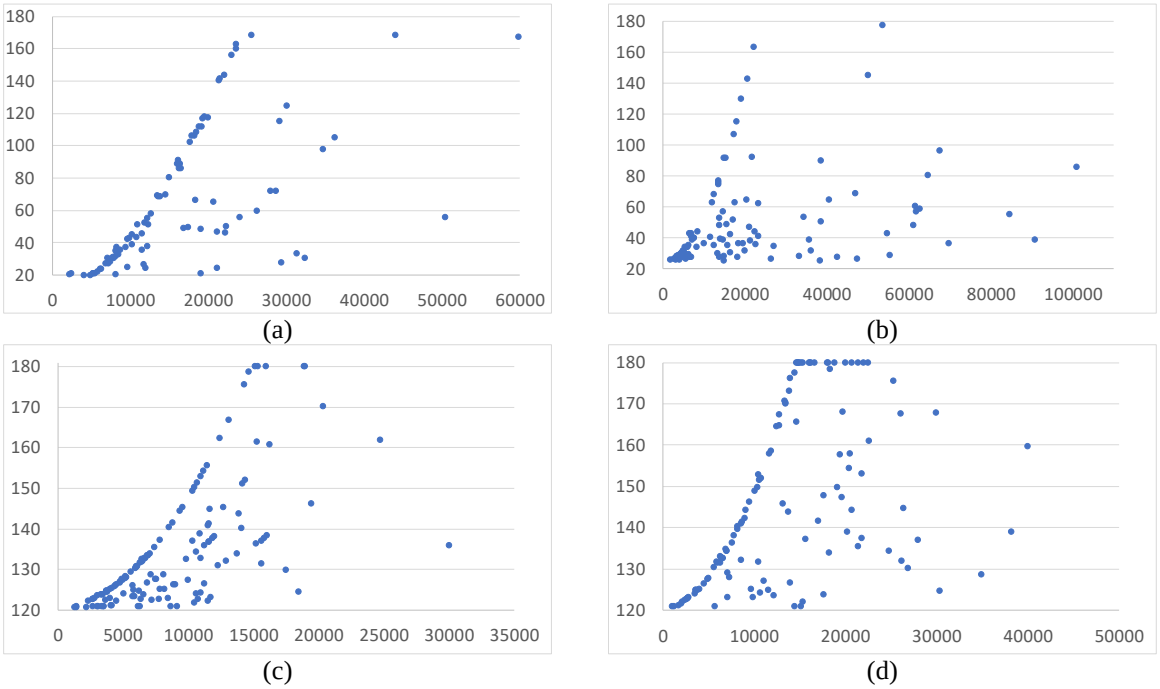

Figure 3.4. LSNB × LSBS vs. the memory used by eigensolver (Gb). a – case A, two points (83470, 91.61) and (96805, 115.59) are not shown, b – case B, c – case C, two points (193116, 76.12) and (214110, 148.68) are not shown, d – case D.

All four cases showed that memory use decreases as the LSNB × Linear Solver Block Size (LSBS) decreases. They are presented in figure 3.4. Such a relationship was expected because LSNB × LSBS is the number of vectors a linear solver would use to solve a given problem. As

it increases, the used memory increases. There are some other factors that influence memory use because multiplication of the number of blocks and the block size should be a linear function and the scattered points show that it is not in this case. The author didn't check what other factors make the memory use not follow the above-mentioned relationship, because the objective wasn't to find the perfect but good enough set of solver parameter values. Additional factors that influence memory use probably are the different preconditioner or eigensolver sizes.

In figure 3.4. few points are grouped around 180 Gb memory value. This is the maximum available memory at one computational node i.e. 36 × 5 Gb = 180 Gb. Simulations exceeding this value were killed by the operating system.

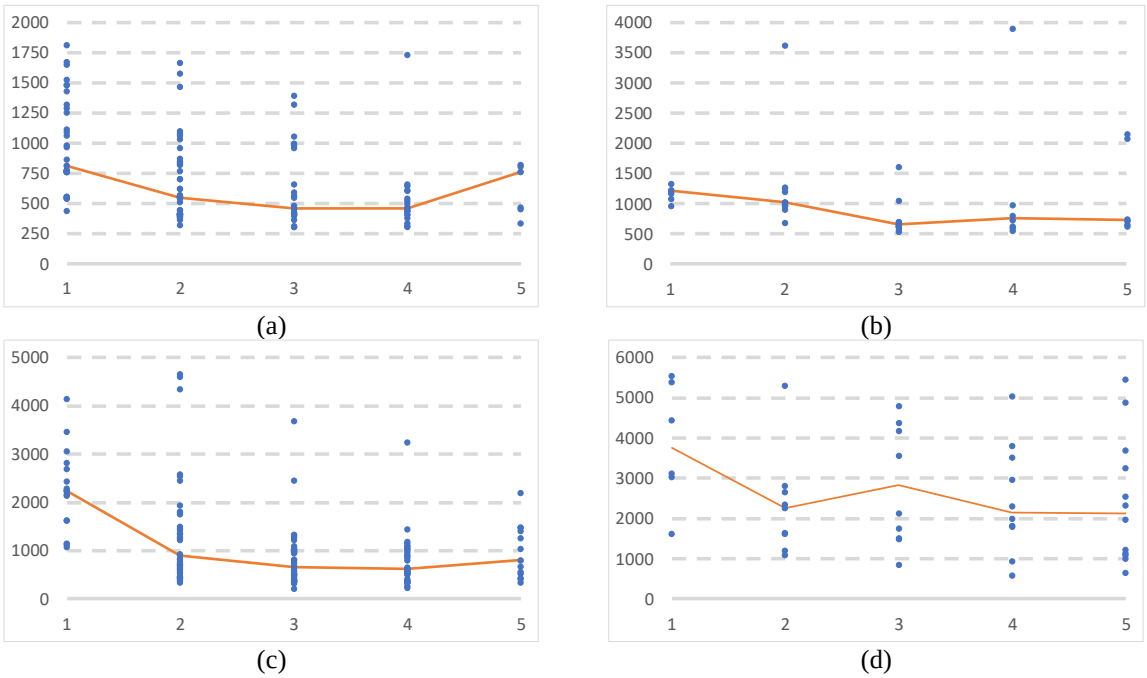

Figure 3.5. LSBS plotted against the solve time (s). The orange line represents the median values. a – case A, two points (3, 4078) and (5, 3705) are not shown, b – case B, c – case C, six points (1, 10966), (1, 11358), (1, 7223), (3, 8309), (4, 10164), (5, 8828) are not shown, d – case D. All points were used to calculate median values.

The results showed that there is a relation between LSBS and the solve time, see figure 3.5. In C and D cases simulations were also run with block sizes larger than five, however, they are not plotted, because larger block sizes were not feasible to use due to large memory requirements, and comparison between cases is easier if the first five sizes are shown in all four plots. Additionally, some points are not shown, because they were far outliers and showing them would make relevant data hard to see, however, these points are taken into median value calculation.

The solve time decreases when the block size is set larger than one i.e. multi-vector instead of single vector iteration. It must be noted that for cases C and D there may be not enough data points to draw robust conclusions because the same amount of experiments was spread over a larger range of LSBS values. The large spread of time values at block size values indicate that there are other factors at play that also considerably influence solve time

.

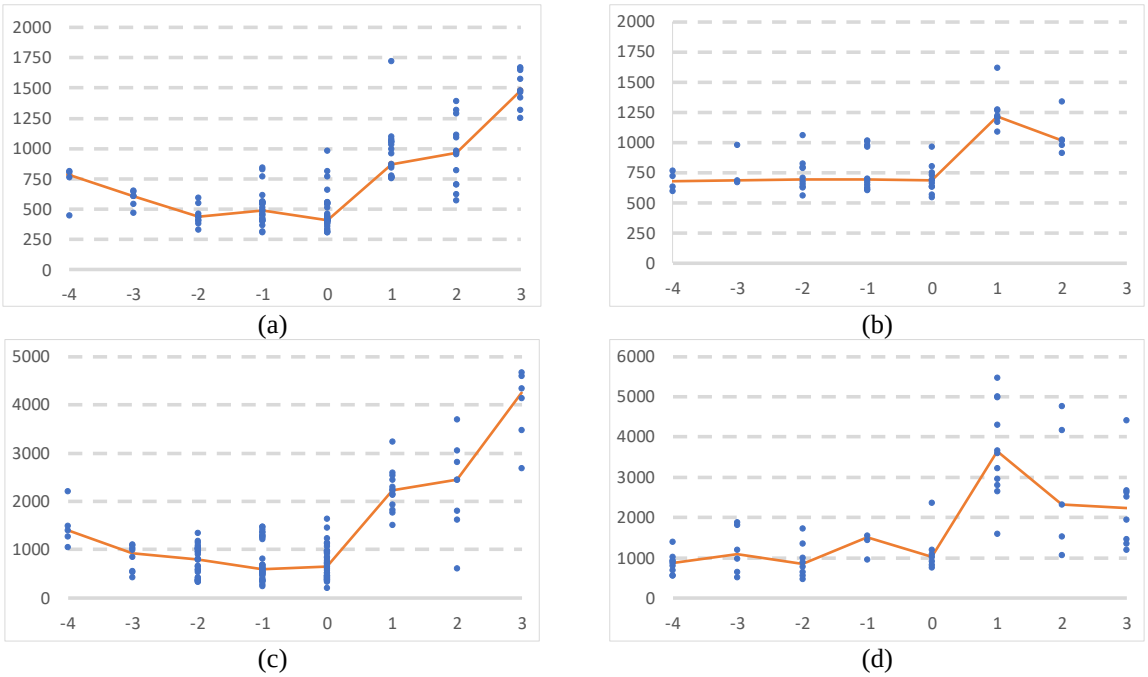

Figure 3.6. ESBS - LSBS plotted against the solve time (s). The orange line represents the median values. a – case A, two points (-2, 3705) and (0, 4077) are not shown, b – case B, c – case C, d – case D, two points (-1, 14804) and (1, 8945) are not shown. All points were used to calculate median values.

Solve time is faster when LSBS is larger than or equal to Eigensolver Block Size (ESBS). This trend can be seen in all four cases and is showed in figure 3.6. The figure only shows values close to zero, although, more were available for cases B and D. They are not shown because few values were available outside of the presented range, therefore, results couldn't be considered reliable. Mostly, this happened, because simulations with large block sizes exceeded available memory and were killed.

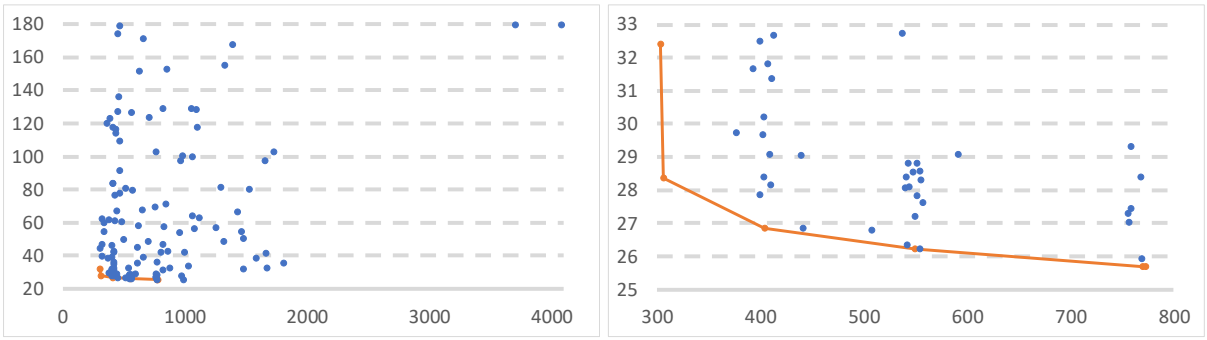

Figure 3.7. Case A physical memory (Gb) used vs. solve time (s). The orange line shows the Pareto frontier. a – all data points, b – area around the Pareto frontier.

Figures 3.7 through 3.10 show all data points and Pareto frontiers for cases A through D respectively. Data points are spread over a large range of values, however, only the first simulations were run with input values over a large range of input values. For later simulations,

the input range was narrowed closer to the area that was thought to contain the optimal solution, so more values are located close to the Pareto frontier. There isn't a single case with a single optimal point, therefore, a reasonable balance between solve time and memory usage had to be considered.

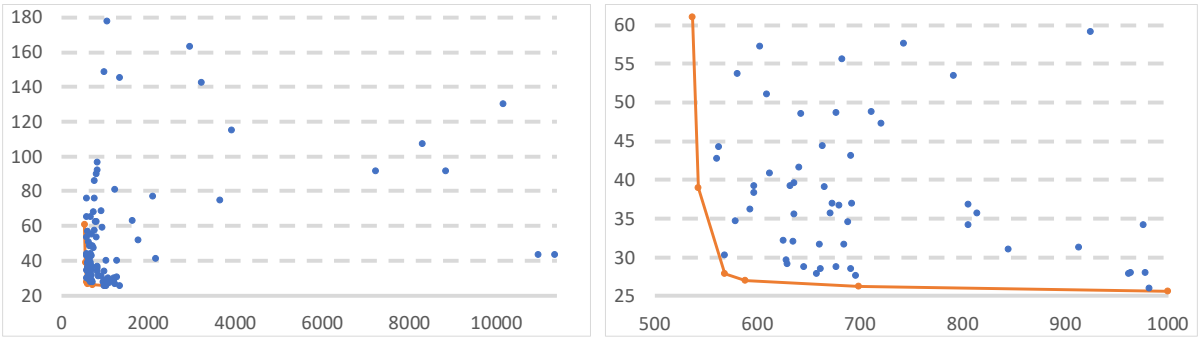

(a) (b)

Figure 3.8. Case B physical memory (Gb) used vs. solve time (s). The orange line shows the Pareto frontier. a – all data points, b –area around the Pareto frontier.

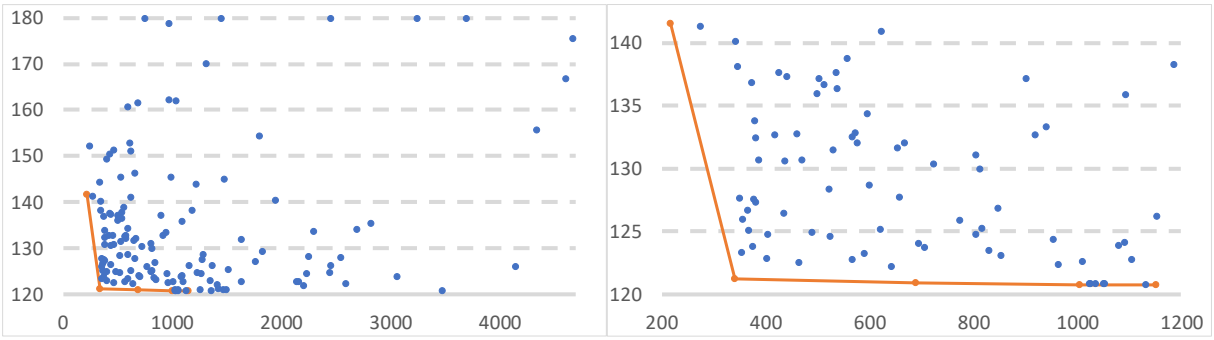

(a) (b)

Figure 3.9. Case C physical memory (Gb) used vs. solve time (s). The orange line shows the Pareto frontier. a – all data points, b – area around the Pareto frontier.

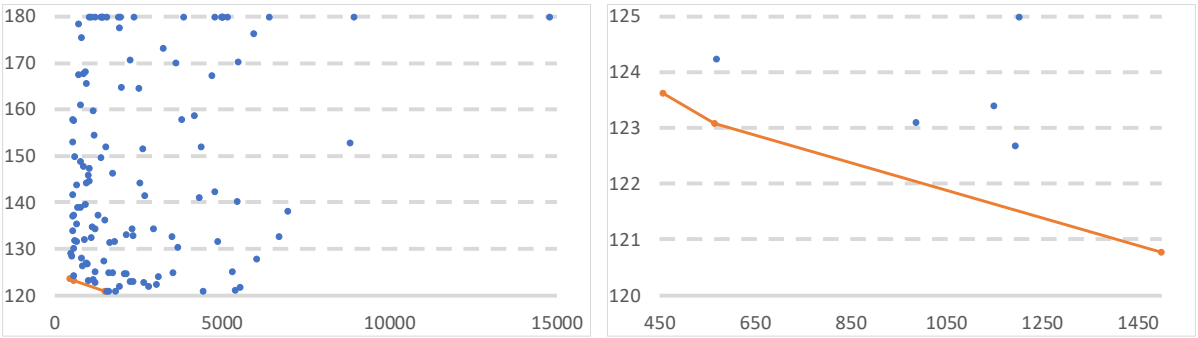

(a) (b)

Figure 3.10. Case D physical memory (Gb) used vs. solve time (s). The orange line shows the Pareto frontier. a – all data points, b – area around the Pareto frontier.

The fastest, the slowest solve times and maximum and minimum memory used in all cases are shown in table 3.4. There is a considerable difference between the slowest and the fastest simulations, which shows what a huge influence the solver properties have. As expected, the fastest solve times are lower for cases A and C, which were solved for 1 eigenvalue and higher

for cases B and D, which were solved for 10 eigenvalues. The minimum amount of memory used was similar between cases A and B, which had sparser stiffness matrices, and cases C and D, which had denser stiffness matrices. This shows that the memory taken by the solver primarily depends on the matrix sparsity, not on the number of requested eigenvalues. Maximum memory used in all cases is close to 180 Gb, because that the maximum available memory at a node and simulations exceeding that would have been killed.

Table 3.4.

Fastest, slowest simulation times and min, max memory used.

Case	Fastest (s)	Slowest (s)	Min memory (Gb)	Max memory (Gb)
A	302.45	4077.61	25.68	180.00
B	536.57	11358.62	25.54	177.89
C	215.99	4668.78	120.76	179.95
D	456.58	14804.14	120.77	179.95

The solver parameter values at the points on Pareto frontiers are shown in table 3.5. Previously, three relations – solve time vs. LSBS, solve time vs. ESBS – LSBS, and the used memory vs. LSNB × LSBS – were discussed.

Table 3.5.

Solver parameters for experiments on the Pareto frontiers

Case	Experiment	Solve Time	Memory used	LSNB	LSBS	ESBS	LSNB × LSBS	ESBS - LSBS
A	137	772.61	25.68	1724	1	2	1724	1
	172	770.20	25.68	1724	1	2	1724	1
	167	549.54	26.21	2214	1	1	2214	0
	134	404.00	26.85	1112	2	2	2224	0
	170	305.59	28.37	1112	3	3	3336	0
	30	302.45	32.40	2025	4	3	8100	-1
B	70	1000.86	25.54	1631	9	1	14679	-8
	132	699.09	26.21	1000	3	2	3000	-1
	113	588.87	26.99	1316	20	2	26320	-18
	99	568.71	27.82	1000	18	3	18000	-15
	139	543.14	38.94	2367	3	3	7101	0
	101	536.58	60.99	3840	16	3	61440	-13
C	108	1151.41	120.76	1362	1	1	1362	0
	123	1003.88	120.77	1526	4	1	6104	-3
	127	689.89	120.86	1736	2	1	3472	-1
	68	341.30	121.18	1000	4	2	4000	-2
	93	215.99	141.57	2913	3	3	8739	0
D	32	1498.95	120.77	1672	9	1	15048	-8
	79	565.17	123.09	1400	7	2	9800	-5
	103	456.58	123.63	1035	17	3	17595	-14

In all four cases, the lowest memory use is achieved when LSNB × LSBS is low when compared to other data points for the same case. This supports the idea that memory related to the value of LSNB × LSBS.

The fastest solve times are achieved when LSBS is larger than the required NEV. It seems faster solve times are achieved when ESBS is larger than one, but not necessarily much larger.

Also, the third idea that the solve time is lower when ESBS is smaller or equal to LSBS is also supported, because the fastest solve times are achieved when ESBS – LSBS is negative.

Table 3.6.

Solver parameters used for peridynamic modal analysis

Parameter	Value
ILU level of fill	1
ILU Drop tolerance	1e-6
ILU Overlap level	0
Linear Solver Max Restarts	10
Linear Solver Number of Blocks	1000
Linear Solver Block Size	6
Eigensolver Max Restarts	10
Eigensolver Number of Blocks	12
Eigensolver Block Size	3

These experiments have shown few relations that will be used to determine solver parameters for next simulations. Table 3.6 shows parameter values that were used for modal simulations in the thesis.

4 SPECIMEN MANUFACTURING AND EXPERIMENTAL SETUP

This chapter provides information on specimen manufacturing and the performed mechanical experiments. The first part describes specimen manufacturing and tensile tests, the second part talks about modal test specimen manufacturing and the third part presents the experimental setup for modal analysis.

4.1 Specimen manufacturing and tensile tests

All specimens were made from polymethyl methacrylate (PMMA), also known as organic glass or Plexiglas. This material was chosen for several of its properties: it is linear for the purposes of modal testing, isotropic, easy to obtain, cheap, easy to cut into shape, easy to work with (not heavy as concrete, smelly as asphalt, abrasive as glass fiber). All specimens were cut from 8 mm thick sheets using laser cutting, see figure 4.1.

Figure 4.1. Tensile specimens cut from a PMMA sheet.

The required mechanical properties were: density, elastic modulus, and Poisson's ratio. The latter two were obtained from tensile tests done according to ASTM D638 standard. Type III specimens were used because the sheet thickness was between 7 and 14 mm, the specimen size is shown in figure 4.2. The height and the width of specimen cross-sections were taken as the average of three measurements, which were done using an electronic caliper with an accuracy of 0.01 mm. Specimen sizes and properties are presented in table 4.1.

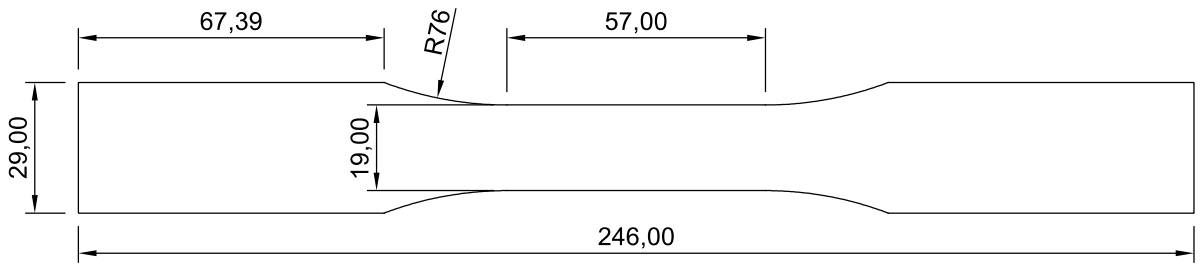

Figure 4.2. ASTM D638 Type III specimen.

Table 4.1.

Tensile specimen size and properties.

Specimen	Height, mm	Width, mm	Area, mm2	Elastic modulus, GPa	Poisson's ratio
1	7.78	18.82	146.42	4.094	0.332
2	7.78	18.80	146.26	5.761	0.342
3	7.76	18.83	146.12	5.488	0.332
4	7.77	18.86	146.54	4.762	0.285
5	7.77	18.69	145.22	5.739	0.345
6	7.77	18.83	146.31	4.425	0.337
7	7.79	18.83	146.69	5.673	0.339
8	7.81	18.83	147.06	5.324	0.380
9	7.77	18.77	145.84	4.789	0.358
Mean	7.778	18.807	146.27	5.348	0.339
Standard deviation	0.015	0.050	0.525	0.617	0.025
Coefficient of variation	0.2%	0.3%	0.4%	12.1%	7.5%

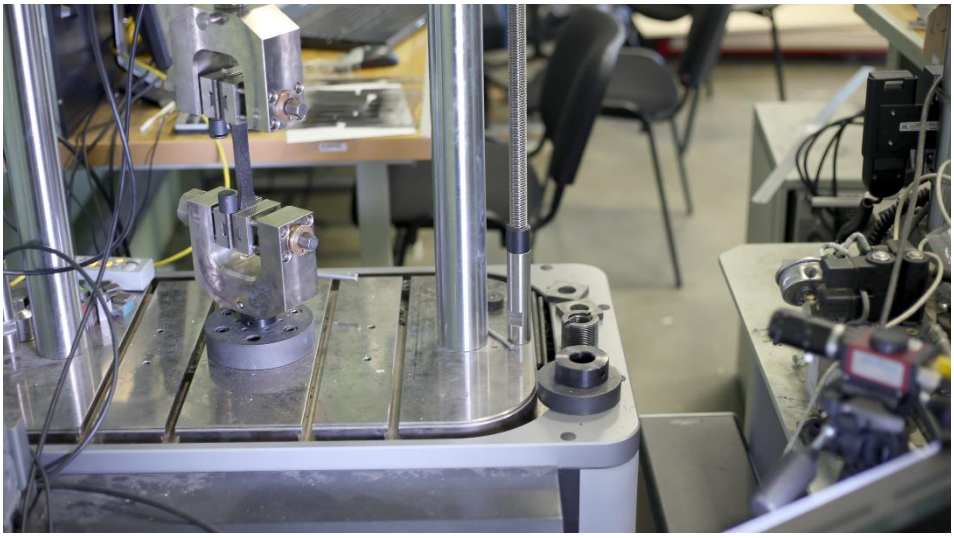

Figure 4.3. Test setup. Testing machine and a specimen (left), DIC camera and a light projector (bottom right).

Tests were done at Riga Technical University using an Instron E10000 Universal testing machine with a test speed of 5 mm/min. The test setup is showed in figure 4.3. The strain was measured using an Imetrum 2D digital image correlation (DIC) system. A DIC system consists of a camera connected to a testing machine. The camera films a specimen as it is deformed and follows several clusters of pixels called targets, please see figure 4.4. Targets and the size of a single pixel are defined at the reference state. Then as a specimen deforms due to some applied

loading, its deformation is calculated depending on how many pixels have these clusters moved. For an overview of DIC systems, the author recommends [104].

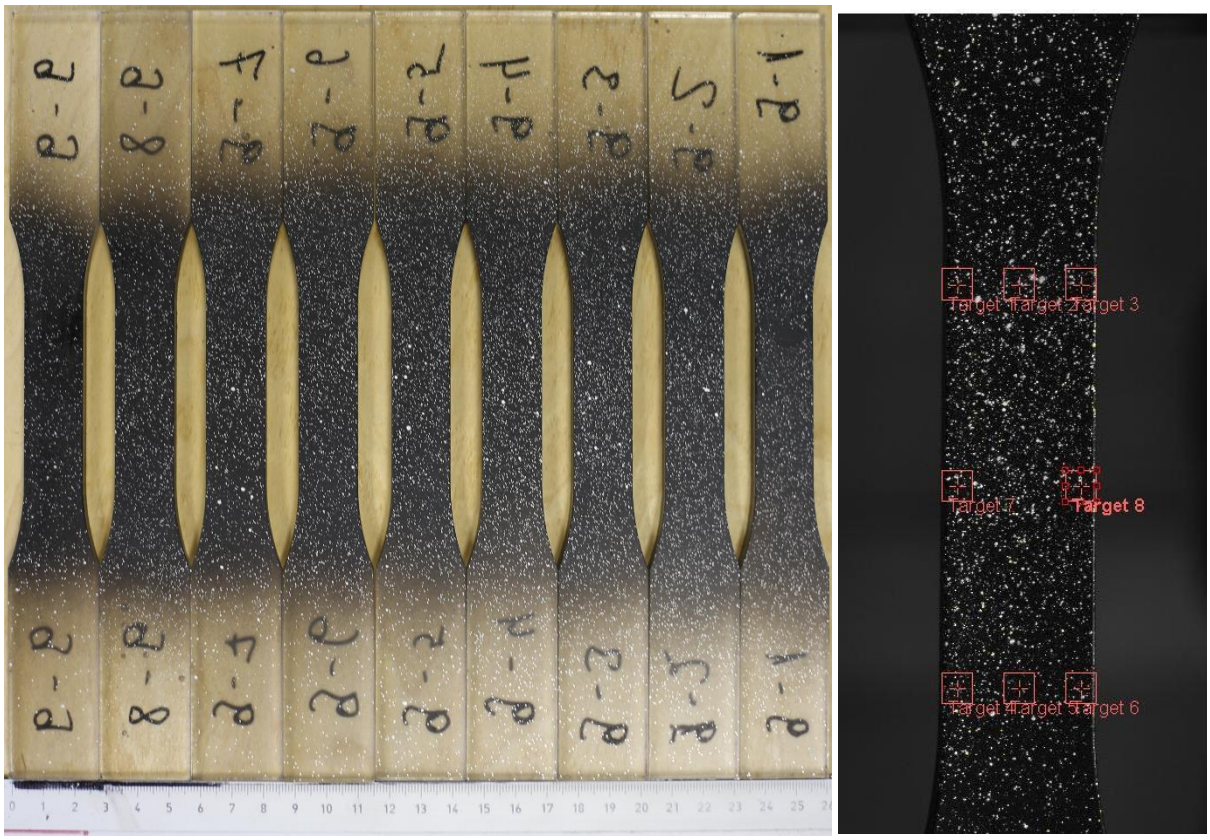

(a) (b)

Figure 4.4. Tensile test specimens. a – all nine prepared specimens, b – DIC targets: 1, 2, 3 (top row); 7, 8 (middle); 4, 5, 6 (bottom).

To enhance the precision of the DIC system, specimen surface was painted black with silver dots as showed in figure 4.4. The applied load was obtained from the testing machine, specimen deformation was calculated by the DIC system as the longitudinal strain between two targets in the middle of a specimen (targets 2 and 5 in figure 4.4.). Elastic modulus was calculated as the slope in $\sigma - \varepsilon$ plot between the lowest measurement with positive σ and positive ε and 0.0001 strain. Poisson's ratio was calculated as

$$\nu = -\frac{\varepsilon_{tr}}{\varepsilon_{lon}}, \tag{4.1}$$

where ν – Poisson's ratio,

ε_{tr} – transversal strain (between DIC targets 7 and 8),

ε_{lon} – longitudinal strain (between DIC targets 2 and 5).

Table 4.1 presents the average values of Poisson's ratios from measurements between 0.001 and 0.003 strain.

Coefficient of variation, defined as

$$CoV = \frac{\sigma}{\mu}, \tag{4.2}$$

where CoV – coefficient of variation,

σ – standard deviation,

μ – average value,

was used to judge the accuracy of tests and calculations. For elastic modulus and Poisson's ratio, it was 12.1% and 7.5% respectively. Per definition, this means that the standard deviation of elastic modulus is 12.1% of its mean value and for Poisson's ratio 7.5% of its mean value. These are reasonably accurate results (the author would consider value below 15% to be sufficiently accurate).

4.2 Specimens for experimental modal analysis

Specimens with a shape of a plate and dimensions of 0.1×0.05×0.008 m were manufactured from several large PMMA sheets using laser cutting as described in chapter 4.1. Specimens before testing are showed in figure 4.5. Their size was measured using an electronic caliper with an accuracy of 0.01 mm and their mass was measured using an electronic scale with an accuracy of 0.1 g. PMMA density was then calculated as a plate's mass divided by its volume. These measurements are presented in table 4.2.

Table 4.2.

PMMA plate size, mass, and density.

Specimen	Thickness, mm	Width, mm	Length, mm	Mass, g	Density, kg/m3
1	7.730	50.150	99.717	45.800	1184.806
2	7.720	50.143	99.603	45.800	1187.849
3	7.693	50.137	99.463	45.700	1191.196
4	7.710	49.933	99.580	45.500	1186.846
5	7.710	50.137	99.643	45.700	1186.474
Mean	7.713	50.100	99.601	45.700	1187.434
Standard deviation	0.014	0.093	0.093	0.122	2.372
Coefficient of variation	0.2%	0.2%	0.1%	0.3%	0.2%

Undamaged specimens and specimens with two kinds of cracks in their cross-section were considered. Hereafter, specimens without any cracks will be called Healthy configuration specimens (see figure 4.5), and damaged specimens will be called either T crack configuration specimens (see figures 4.6 and 4.8) or S crack configuration specimens (see figures 4.7 and 4.8). Moreover, five specimens were tested at each configuration to assess the influence of slightly different material properties and manufacturing imprecisions.

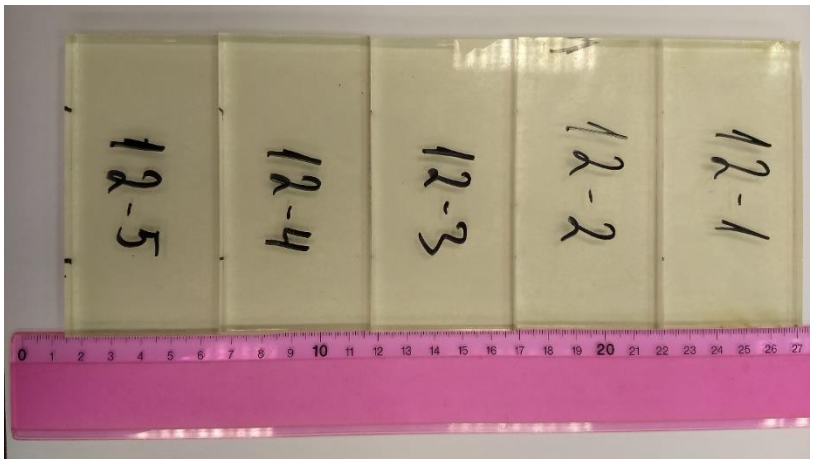

Figure 4.5. PMMA plates before modal testing. The yellow background is the paper tape applied to prevent the laser beam from shining through.

The damage was introduced as a cut crack in the cross-section of a specimen. Four approaches to crack creation were considered:

- laser cutting;
- using a jeweler's saw;
- using a sharp razor blade;
- growing a fatigue crack.

The method has to be fast and precise, it must be possible to extend a crack later. Moreover, the loss of mass has to be as low as possible. Jewelers saw, razorblade and fatigue crack growth created roughly but not exactly the same crack path in all specimens. Furthermore, the crack length when a crack was extended was not sufficiently similar across all five specimens. So only laser cutting fit all four criteria.

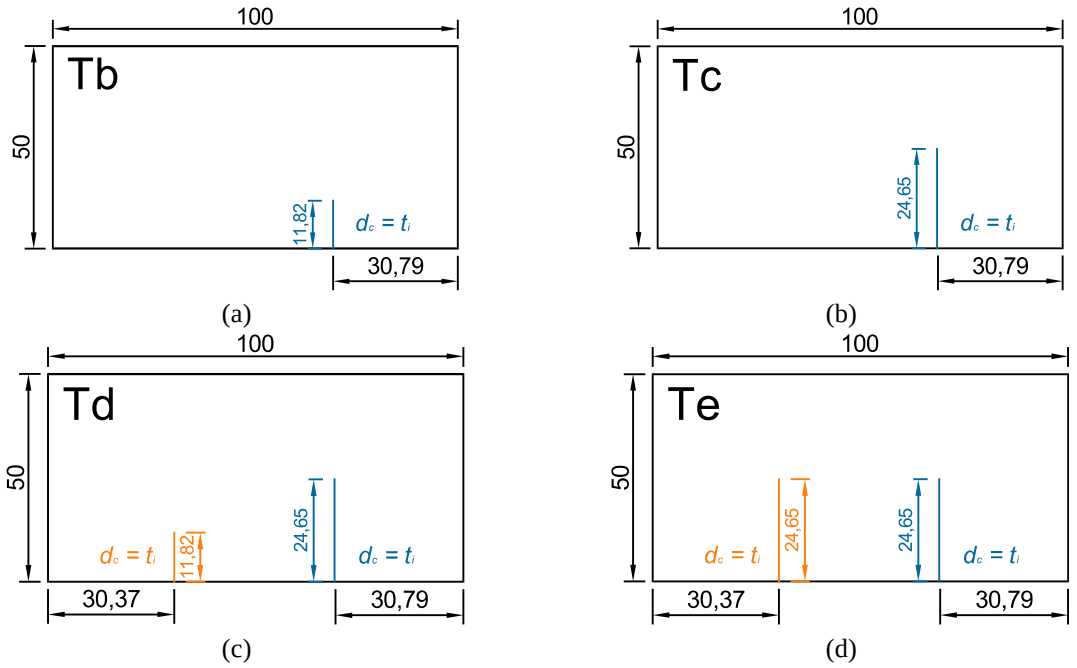

Figure 4.6. Crack location, length, and depth for the four T crack configuration specimens. d_c – depth of a crack, t_i – the thickness of a plate.

Laser cutting works by melting the material under the beam, which leaves some residual material in the cut, so a paper sheet was slid through the crack to ensure that it is clear of any leftovers. It was not possible to measure the exact crack opening, however, a sheet of paper is about 0.12 mm thick, so the crack opening was slightly larger.

The first – T crack configuration – had cracks through the thickness of a specimen, the second – S crack configuration – had cracks on the back face of a specimen. Actual crack length, depth, and location are showed in figure 4.6 and figure 4.7 for T and S crack configurations respectively. The nominal length of T configuration cracks was 12.5 mm and 25.00 mm. These lengths were used in computational simulations.

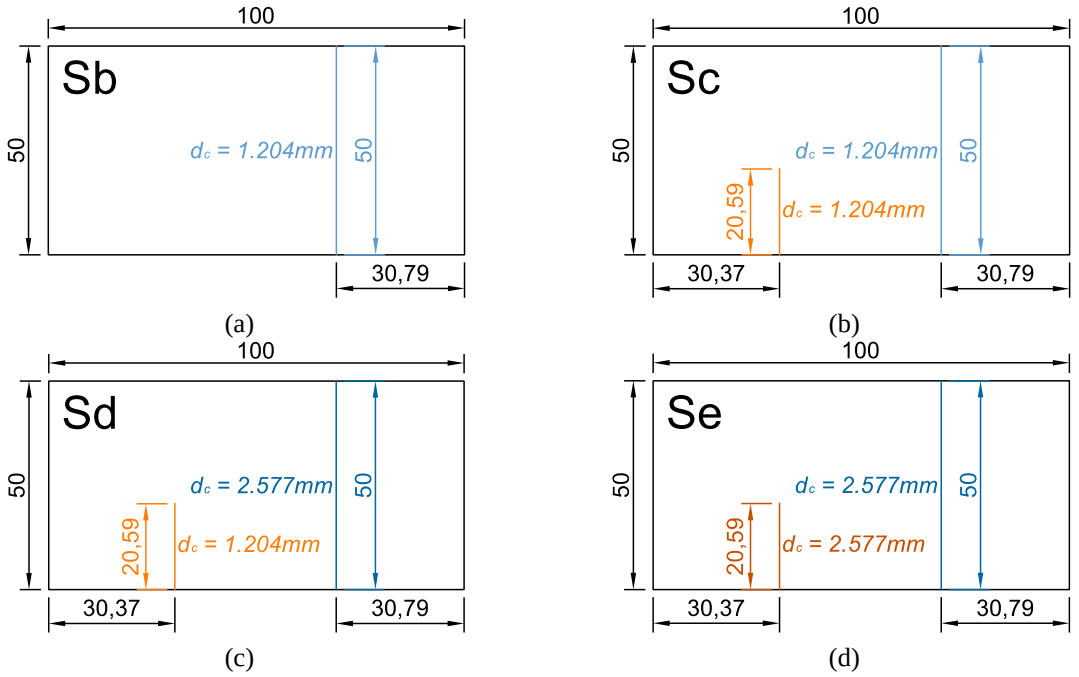

Figure 4.7. Crack location, length, and depth for the four S crack configuration specimens. d_c – depth of a crack.

Four different crack configurations – showed in figure 4.6 and named Tb, Tc, Td, Te – were tested for the T case. Four different crack configurations – showed in figure 4.7 and named Sb, Sc, Sd, Se – were tested for the S case. The process of creating and testing these specimens was as follows:

1. Take the ten specimens and create a crack corresponding to Tb configuration in five of them and create a crack corresponding to Sb configuration in the other five;
2. Apply a paper tape on them to prevent the laser from shining through and make a cut in where the tape is on top of a crack;
3. Perform experimental modal analysis using these ten specimens;
4. Extend cracks in the existing plates to correspond to the next configuration e.g. Tb → Tc or Sb → Sc;
5. Repeat experimental modal analysis;
6. Repeat steps 4 and 5 for all crack configurations.

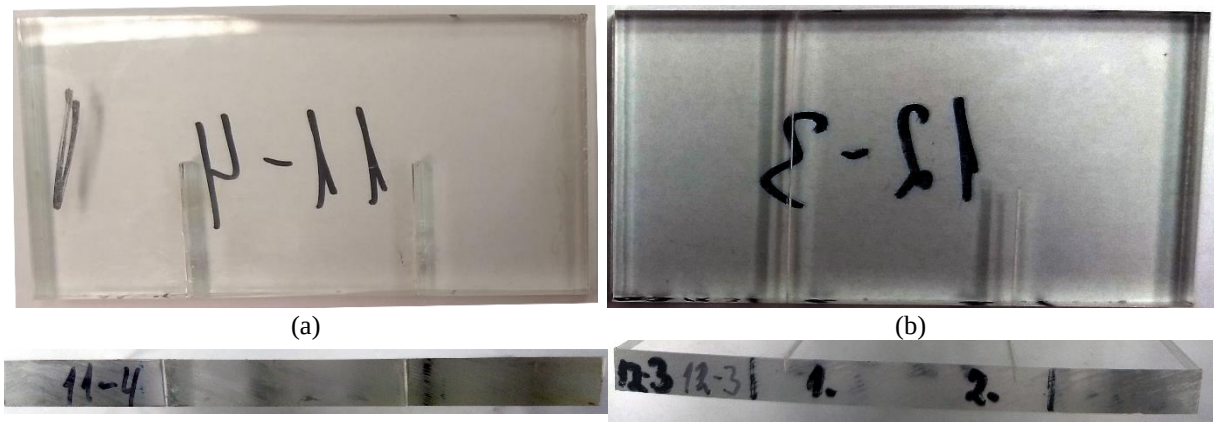

(a) (b)

(c) (d)

Figure 4.8. PMMA specimens. a, c – Te crack configuration; b, d – Se crack configuration. Specimens don't appear fully rectangular, because they were photographed at an angle to make cracks more visible.

Crack length in T and S configuration specimens was measured on the face of a specimen using an electronic caliper. Crack depth in T configuration specimens is equal to specimen's thickness. In S crack configuration's specimens, it was measured by taking a picture of the bottom side of a specimen, see figure 4.8d, counting pixels along the crack depth and along plate's thickness, then calculating crack depth as a ratio between counted pixels multiplied by the known plate's thickness:

$$d_c = \frac{n_c^{px}}{n_t^{px}} \times t_i, \tag{4.3}$$

where d_c – crack depth,

n_c^{px} – number of pixels along the crack depth,

n_t^{px} – number of pixels along the thickness,

t_i – specimen thickness.

Exact crack length and depth is showed in figures 4.6 and 4.7 for T and S cases respectively.

4.3 Experimental modal analysis

The experimental modal analysis test setup is showed in figure 4.9. Test specimens were suspended from an aluminum frame in two loops made from cotton thread to allow specimens to move as free as possible, thus creating Free-Free boundary conditions (BC).

2D Polytec PSV-400 laser vibrometer measured specimen speed at several hundred points on their surface. Since PMMA is translucent, a single layer of paper tape was applied on the surface facing the vibrometer, to prevent the laser beam from shining through. Tape increased specimen mass and thickness by less than 1 %, so the effect on measured modal properties can be considered negligible. Shallow marks were made at the bottom of plates at 25 mm distance from either end, to have the two cotton loops always positioned at the same place. This was done to ensure that BCs between all tests were as similar as possible.

Specimens were excited using a loudspeaker that was repositioned depending on which modes – bending or torsional – needed to be excited. This was done because it is easier to distinguish between a real mode and a background noise if the object is excited near a point of maximum displacement. For bending modes maximum displacement occurs at either end of a specimen, but for torsional modes at either corner of a specimen. For example, figure 4.9b shows a specimen that is being excited at one corner to measure torsional modes.

(a)

(b)

Figure 4.9. Experimental modal analysis test setup. a – measuring head of a 2D Polytec laser vibrometer (front right), loudspeaker and a suspended specimen (back right), test frame (back right), acquisition system, amplifier and a computer (left). b – loudspeaker (center left), specimen suspended in cotton threads (center right), aluminum frame (top and right).

Measurement range was between 1000 and 8000 Hz with measurement step $\Delta f = 2.5$ Hz. Each point was measured for 400 ms and velocity decoder VD-07 1 mm/s/V was used.

A total of 48 modes were measured for each specimen:

- 5 modes for each of five specimens at Healthy configuration;
- 23 modes for each of five specimens at T crack configurations;
- 20 modes for each of five specimens at S crack configurations.

All experimental modal analysis results are presented in chapter 5 Verification and validation of peridynamic modal analyses.

5 VERIFICATION AND VALIDATION OF PERIDYNAMIC MODAL ANALYSIS

The first part of this chapter presents results of peridynamic, finite-element, and experimental modal analyses. PD data are verified against the finite-element data and validated against the experimental data. Additionally, the frequency shift due to increasing damage is discussed. The second part starts with a comparison between the PD and the FE mode shapes and then discusses the PD and the experimental mode shapes.

Specimens are grouped by their crack configurations – Healthy, Tb through Te, and Sb through Se. For exact details on these configurations please see chapter 4 Specimen manufacturing and experimental setup. The mode order changed between different crack configurations, so it was not possible to refer to individual modes by their number in the order of appearance, hence, modes will be referred to by their type and number within that type e.g. 2nd bending mode, 1st torsional mode, etc.

5.1 Modal frequencies

Results of the peridynamic modal analysis

Peridynamic simulations were done for the four different mesh densities and the four different horizon lengths presented in table 3.1. 96 modes were computed for specimens at the Healthy configuration, 384 for T crack configuration and 384 for S crack configuration specimens. These numbers exclude the rigid-body-motion modes. Modal frequencies at Healthy configuration are presented in table 5.1, but the frequencies at other configurations are presented in appendix A.

Only the 625 000 node model's results are used in this chapter. Computational results converge when the mesh density increases so the largest model gives the most accurate results. Two kinds of convergences can be noticed. The δ-convergence, in which the computed frequencies converge as the length of the horizon shrinks, and the δm-convergence, in which the frequencies converge as the mesh spacing and the horizon shrinks simultaneously. Both convergences are discussed in chapter 6 Convergence studies.

Results of the finite-element modal analysis

Six modes were obtained using FE modal analysis for specimens at each crack configuration. A total of 54 modes were computed. The modal frequencies at Healthy and T crack configurations are presented in table 5.2. Frequencies at the Healthy and S crack configurations are presented in table A.9 in appendix A. Healthy configuration data are repeated in both tables because it makes the comparison between simulations with and without damage easier.

Table 5.1.

PD modal frequencies (Hz) at Healthy configuration.

Nodes in a model	Horizon	Mode					
		1st bending	1st torsional	2nd torsional	2nd bending	1st TB[a]	1st IPB[b]
40000	$\sqrt{2}h$	1656.45	1961.24	4213.43	4421.60	6463.92	6855.45
40000	$2h$	1666.51	1882.92	4071.67	4436.87	6457.59	6847.60
40000	$3h$	1603.36	1854.61	4005.40	4287.40	6236.04	6774.63
40000	$4h$	1563.82	1838.27	3969.13	4194.43	6121.37	6705.49
135000	$\sqrt{2}h$	1683.39	1969.31	4236.11	4486.55	6545.51	6860.09
135000	$2h$	1685.50	1932.26	4167.42	4486.55	6529.10	6853.90
135000	$3h$	1652.78	1915.10	4127.09	4407.38	6410.84	6844.82
135000	$4h$	1629.52	1904.87	4103.94	4352.56	6337.13	6832.72
320000	$\sqrt{2}h$	1693.15	1972.27	4244.60	4510.37	6575.51	6861.73
320000	$2h$	1693.18	1950.68	4203.86	4507.07	6559.73	6856.69
320000	$3h$	1673.29	1939.48	4177.27	4458.10	6486.29	6851.13
320000	$4h$	1657.96	1932.48	4160.81	4421.19	6434.47	6842.54
625000	$\sqrt{2}h$	1697.80	1973.73	4248.81	4521.83	6590.00	6862.49
625000	$2h$	1697.13	1959.60	4221.73	4517.77	6576.06	6858.35
625000	$3h$	1683.75	1951.75	4202.95	4484.41	6525.83	6854.47
625000	$4h$	1672.78	1946.68	4190.64	4457.51	6486.96	6847.84

a – transversal bending mode
b – in-plane bending mode

Results of the experimental modal analysis

25 modes were measured experimentally at Healthy configuration, 115 at T crack configurations and 100 at S crack configurations. All measured frequencies are shown in table 5.3 and in appendix A. Values of the Healthy configuration are presented in both tables, so that healthy and damaged plate modal frequencies can be compared easily.

Five modal frequencies were measured for all configurations except Tc, Td, and Te for which six frequencies were measured. One more mode was in the measurement range because another mode shifted into the frequency measurement range when the stiffness decreased due to damage.

Conversely, a set number of modes rather than all modes within a frequency range were computed. This will be discussed in more detail later, but it is noted that at each S crack configuration all experimental modes had a corresponding PD mode, however, at each T crack configuration only the first two bending and the first two torsional modes had a corresponding PD mode.

Modal frequency coefficient of variation (CoV) was computed for all modes to assess the quality of crack manufacturing method and reliability of the experimental results. Lower CoV would imply that the spread of the experimental results is lower, therefore, the mean value is more representative of the whole group. The author would consider CoV under 5 % an excellent result. Individual CoV values are presented in table 5.3 and table A.10.

Table 5.2.

FE modal frequencies (Hz) at Healthy and T crack configurations.

Mode	Mode type	f, Hz
	Healthy configuration	
1st	1st bending	1706.50
2nd	1st torsional	1976.50
3rd	2nd torsional	4256.80
4th	2nd bending	4543.00
5th	1st in-plane bending	6614.50
6th	1st transversal bending	6863.60
	Tb crack configuration	
1st	1st bending	1639.20
2nd	1st torsional	1903.90
3rd	2nd torsional	4045.50
4th	2nd bending	4286.80
5th	1st in-plane bending	5699.70
6th	1st transversal bending	6581.50
	Tc crack configuration	
1st	1st bending	1404.30
2nd	1st torsional	1642.20
3rd	1st In-plane bending	3178.20
4th	2nd torsional	3365.80
5th	2nd bending	3766.10
6th	3rd torsional	5610.30
	Td crack configuration	
1st	1st bending	1377.10
2nd	1st torsional	1612.10
3rd	1st in-plane bending	3138.20
4th	2nd torsional	3186.20
5th	2nd bending	3556.00
6th	3rd torsional	5365.90
	Te crack configuration	
1st	1st bending	1268.10
2nd	1st torsional	1459.40
3rd	2nd torsional	2592.90
4th	1st in-plane bending	2716.50
5th	2nd bending	3099.40
6th	2nd in-plane bending	4405.80

Table 5.3.

Experimental modal frequencies (Hz) at Healthy and T crack configurations.

Mode	Mode type	Specimen					μ	σ	CoV
		1	2	3	4	5			
Healthy configuration									
1	1st bending	1665.00	1677.50	1665.00	1665.00	1662.50	1667.00	5.97	0.36%
2	1st torsional	1925.00	1927.50	1927.50	1925.00	1925.00	1926.00	1.37	0.07%
3	2nd torsional	4200.00	4197.50	4197.50	4197.50	4197.50	4198.00	1.12	0.03%
4	2nd bending	4522.50	4527.50	4507.50	4515.00	4507.50	4516.00	8.94	0.20%
5	1st trans. bending	6467.50	6472.50	6460.00	6527.50	6457.50	6477.00	28.85	0.45%
Tb crack configuration									
1	1st bending	1610.00	1592.50	1590.00	1590.00	1590.00	1594.50	8.73	0.55%
2	1st torsional	1850.00	1850.00	1850.00	1850.00	1837.50	1847.50	5.59	0.30%
3	2nd torsional	3977.50	3987.50	3955.00	3987.50	3960.00	3973.50	15.27	0.38%
4	2nd bending	4265.00	4250.00	4280.00	4272.50	4280.00	4269.50	12.55	0.29%
5	1st trans. bending	6455.00	6432.50	6400.00	6480.00	6417.50	6437.00	31.39	0.49%
Tc crack configuration									
1	1st bending	1370.00	1370.00	1355.00	1370.00	1370.00	1367.00	6.71	0.49%
2	1st torsional	1587.50	1582.50	1582.50	1582.50	1582.50	1583.50	2.24	0.14%
3	2nd torsional	3327.50	3337.50	3287.50	3352.50	3312.50	3323.50	24.85	0.75%
4	2nd bending	3750.00	3732.50	3722.50	3750.00	3732.50	3737.50	12.12	0.32%
5	3rd torsional	5567.50	5567.50	5507.50	5587.50	5567.50	5559.50	30.33	0.55%
6	1st trans. bending	6462.50	6480.00	6477.50	6540.00	6485.00	6489.00	29.72	0.46%
Td crack configuration									
1	1st bending	1345.00	1350.00	1345.00	1365.00	1347.50	1350.50	8.37	0.62%
2	1st torsional	1562.50	1570.00	1570.00	1580.00	1570.00	1570.50	6.22	0.40%
3	2nd torsional	3137.50	3155.00	3155.00	3192.50	3155.00	3159.00	20.20	0.64%
4	2nd bending	3607.50	3600.00	3570.00	3607.50	3607.50	3598.50	16.26	0.45%
5	3rd torsional	5292.50	5332.50	5330.00	5412.50	5332.50	5340.00	43.95	0.82%
6	1st trans. bending	6507.50	6510.00	6497.50	6575.00	6507.50	6519.50	31.39	0.48%
Te crack configuration									
1	1st bending	1245.00	1250.00	1245.00	1250.00	1250.00	1248.00	2.74	0.22%
2	1st torsional	1400.00	1430.00	1400.00	1450.00	1430.00	1422.00	21.68	1.52%
3	2nd torsional	2522.50	2550.00	2540.00	2587.50	2550.00	2550.00	23.78	0.93%
4	2nd bending	3087.50	3105.00	3105.00	3107.50	3105.00	3102.00	8.18	0.26%
5	3rd torsional	5240.00	5225.00	5210.00	5237.50	5240.00	5230.50	13.04	0.25%
6	1st trans. bending	6485.00	6455.00	6445.00	6517.50	6455.00	6471.50	29.77	0.46%

CoV values for specimens at Healthy configuration ranged between 0.07 % and 0.45 %, for specimens at T crack configurations between 0.14 % and 1.52 % and for specimens at S crack configurations between 0.00 % and 0.78 %. All CoV values except one – 1st torsional mode at Te crack configuration – were below 1 %. The author considers such low CoV values an excellent result, which shows that the experimental modal frequencies were spread within a narrow window around the average value. Thus the influence of the crack manufacturing

process and the testing process on each separate result was minuscule. Figure 5.1 presents the changes in CoV values at different crack configurations and the average CoV value as the damage progresses.

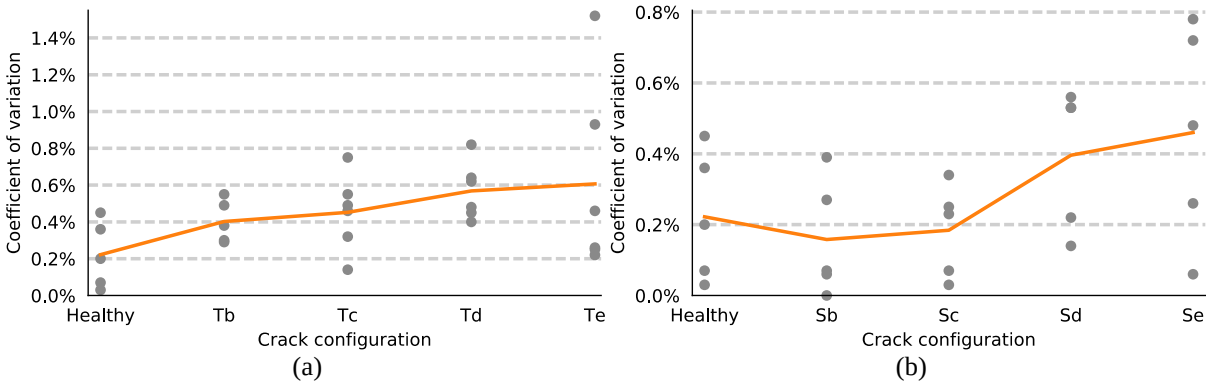

Figure 5.1. The experimental modal frequency CoV values at different crack configurations. Gray dots show the CoV values and the orange line shows the average value. a – T crack configuration, b – S crack configuration.

The CoV value is larger at later crack configurations. The average CoV is 0.22 % at Healthy configuration. Then for T crack configuration specimens, it grows to 0.61 % at Te configuration, see figure 5.1a, but for S crack configuration specimens the average CoV value increases to 0.46 % at Se configuration, see figure 5.1b. There is a slight decrease to 0.16 % at Sb crack configuration. Most likely the drop happened because the specimen BCs were more similar between the separate Sb configuration tests than between the Healthy configuration tests. These two graphs show that manufacturing imprecisions between the specimens increased as they were re-manufactured into new crack configurations. This was expected because it is impossible to perfectly replicate the manufacturing process across for all specimens. Still, the CoV values are reasonably low for both T and S crack configuration specimens.

It would be hard to use modal frequencies of each specimen, moreover, it was showed that the spread around each mode's average modal frequency was acceptably low, thus average values were fairly representative. Therefore, the average modal frequency value at each mode, not the separate specimen frequencies will be used hereafter.

Verification and validation of the PD modal frequencies

This section verifies the obtained PD results against the FE results and validates them against the experimental results. The finite-element analysis results were used as the benchmark because it is the most widely used computational method for modal analysis. It is, therefore, well understood and its results are trusted by both researchers and engineers. Validations against experimental results will also be presented. Both PD and FE results were compared with experimental results to see which computational method best agrees with them. Exact modal frequency values with calculated percent differences are presented in tables in appendix B.

Not all modes were computed at all crack configurations. Only the 1st and the 2nd bending and the 1st and the 2nd torsional modes were computed with PD and FE analysis at all four T crack configurations. Other modes, such as the 1st transversal bending mode, were computed

only at Healthy and Tb configurations, but not at other configurations. Five modes – the 1st and the 2nd bending, the 1st and the 2nd torsional and the 1st transversal bending – were computed at all S crack configurations. This happened because the mode order was different for different crack configurations.

As will be showed in chapter 6 Convergence Studies larger computational models converge to some expected value. So the computational results used in this chapter are taken from the PD simulations with the 625 000 node model. Additionally, only the results computed with the shortest horizon $\delta = \sqrt{2}h$ and the longest horizon $\delta = 4h$ will be used for comparison. This will show a comparison of the most local and the most non-local result while keeping figures easy to read. Results with other horizon values are used for convergence studies in chapter 6.

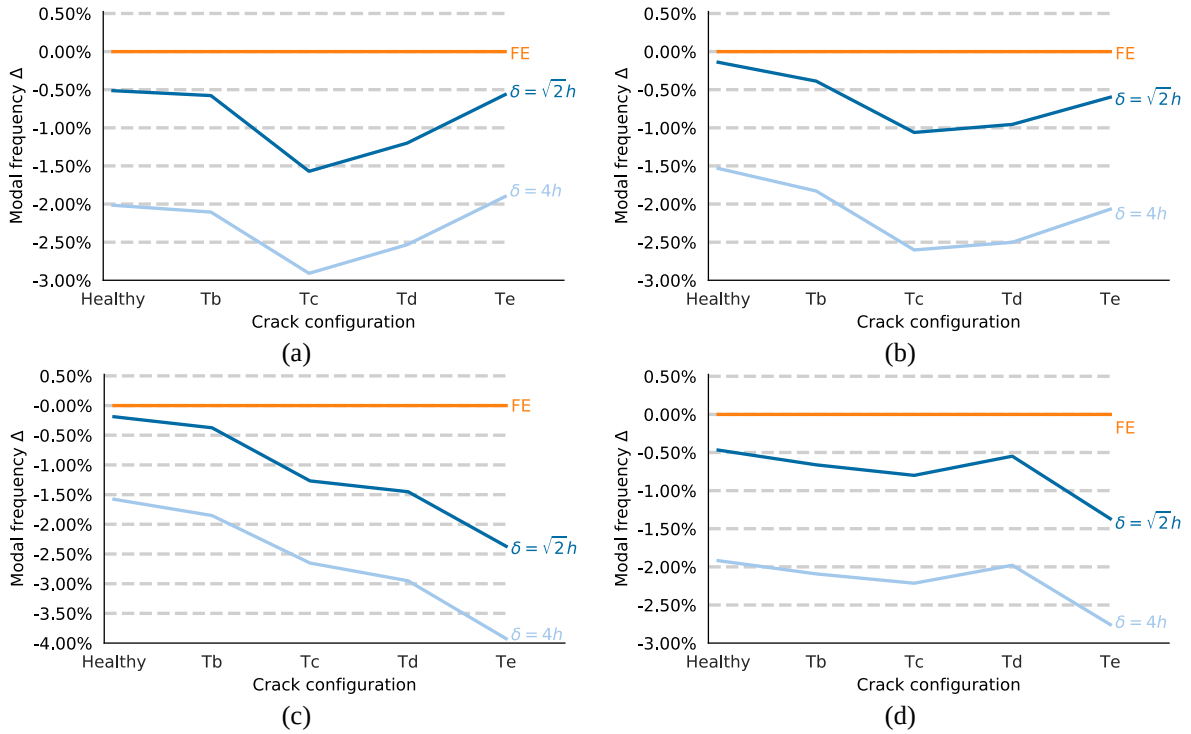

Figure 5.2. The percent difference between PD modal frequencies and FE modal frequencies at T crack configurations. a – 1st bending mode, b – 1st torsional mode, c – 2nd torsional mode, d – 2nd bending mode.

The percent difference between PD modal frequencies and FE modal frequencies at Healthy and T crack configurations are presented in figure 5.2 and table B.1 in Appendix B. Some differences between the PD and the FE results were expected because the same problem was solved using two different mechanics theories, but the results clearly show a very good agreement The largest difference between modal frequencies when $\delta = \sqrt{2}h$ at Healthy configuration is -0.51 % for the 1st bending mode, at Tb crack configuration -0.66 % for the 2nd bending mode, at Tc crack configuration -1.57 % for the 1st bending mode, at Td crack configuration -1.45 % for the 2nd torsional mode, and at Te crack configuration -2.37 % for the 2nd torsional mode. When $\delta = 4h$ the largest difference at Healthy configuration is -2.02 %, at Tb – -2.10 %, at Tc – -2.91 % all for the 1st bending mode, at Td – -2.95 % for the 2nd torsional mode, at Te crack configuration -3.92 % for the 2nd torsional mode.

PD modal frequencies were lower than FE modal frequencies at Healthy and all T crack configurations, see figure 5.2. The PD and the FE mass matrices were created using the same lumped-mass approach, material density was the same and the total volume of the model was the same. The biggest difference between the matrices was that the FE mass matrix was larger because there were more nodes in the FE model. Therefore, the differences in computed modal frequencies most likely occurred due to different stiffness matrices. The PD stiffness matrix is denser and its bandwidth is higher than for the FE equivalent for the same problem, these two differences are explained in more detail in chapter 3.1. Since the PD frequencies were lower, the PD computational stiffness must have been lower than the FE computational stiffness.

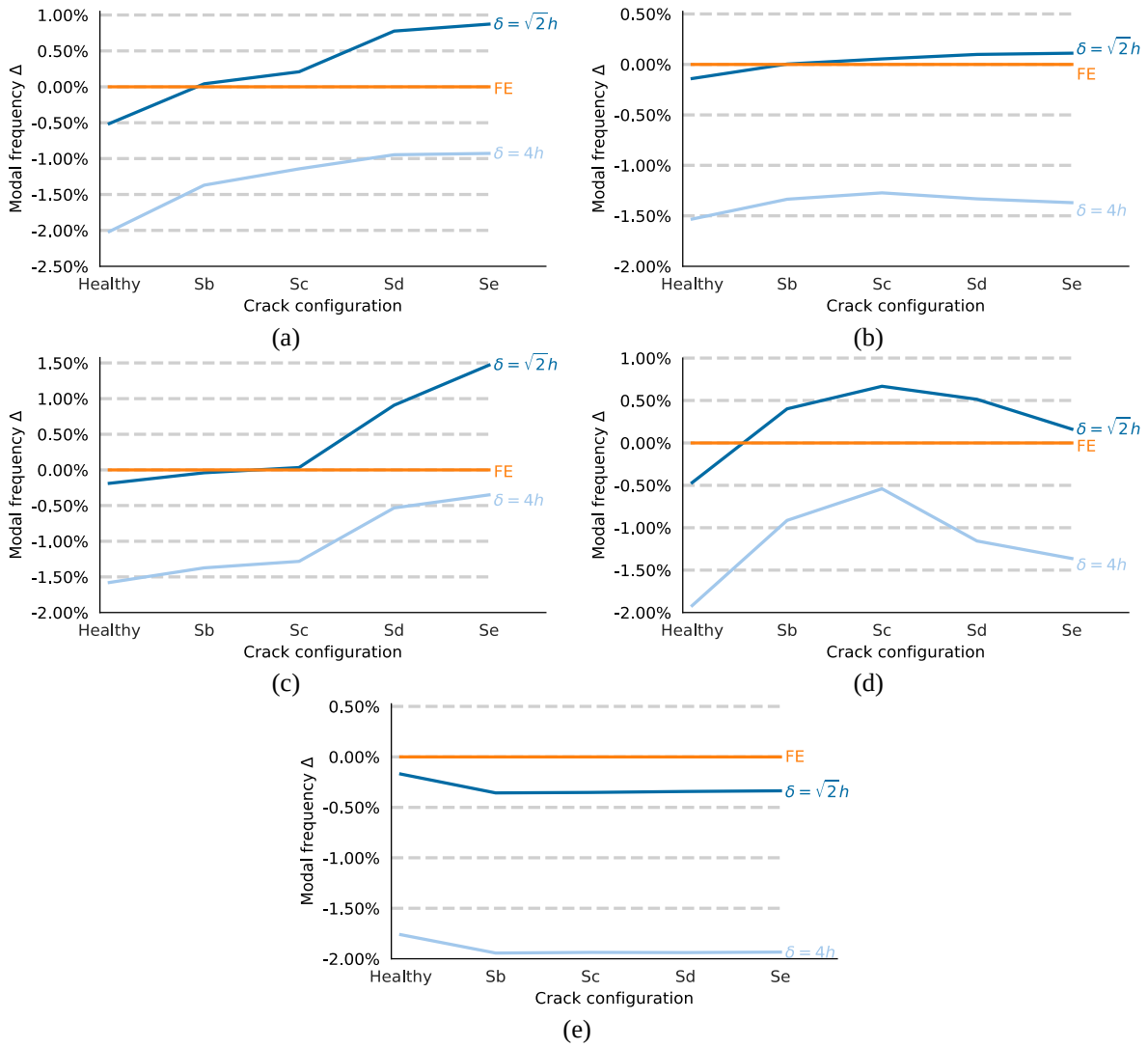

Figure 5.3. The percent difference between PD modal frequencies and FE modal frequencies at S crack configurations. a – 1st bending mode, b – 1st torsional mode, c – 2nd torsional mode, d – 2nd bending mode, e – 1st transversal bending mode.

The percent difference between PD modal frequencies and FE modal frequencies at Healthy and S crack configurations are presented in figure 5.3 and table B.2. The percent difference between PD and FE results at Healthy configuration ranged from -2.02 % to -0.14 %, at Sb configuration between -2.02 % and 0.40 %, at Sc between -1.94 % and 0.67 %, at Sd between

-1.94 % and 0.67 %, at Se between -1.93 % and 1.47 %. These results show an excellent agreement between the PD and the FE modal analyses in models with and without cracks.

FE modal frequencies were not always higher at S crack configurations like they were at T crack configurations, which means that the non-local PD computational stiffness isn't always lower than the local FE computational stiffness. But the PD frequencies computed with longer horizon being lower than frequencies computed with shorter horizon still holds true.

Also, PD results with the horizon $\delta = \sqrt{2}h$ agreed better with the FE results than simulations with the horizon $\delta = 4h$ at most but not all crack configurations. The exceptions being the 2nd torsional mode at Sd and Se configurations and the 2nd bending mode at Sc crack configurations. This shows that the difference between FE stiffness and the PD stiffness is changing depending on the crack configuration, which was expected because the cracks in the models are created differently.

Moreover, PD simulations with the horizon $\delta = 4h$ resulted in lower modal frequencies than PD simulations with $\delta = \sqrt{2}h$. This shows that the computational stiffness is influenced by the length of the horizon and that it is lower when longer horizon values are used. Additionally, the agreement between PD and FE results is closer when the horizon is shorter. This was expected because the FE analysis gives a local solution, which should be better approximated by a shorter horizon i.e. $\delta = \sqrt{2}h$. Moreover, it has been shown that under sufficiently smooth motion, constitutive model, and non-homogeneities the non-local PD solution approaches the local solution when the horizon shrinks to zero [23].

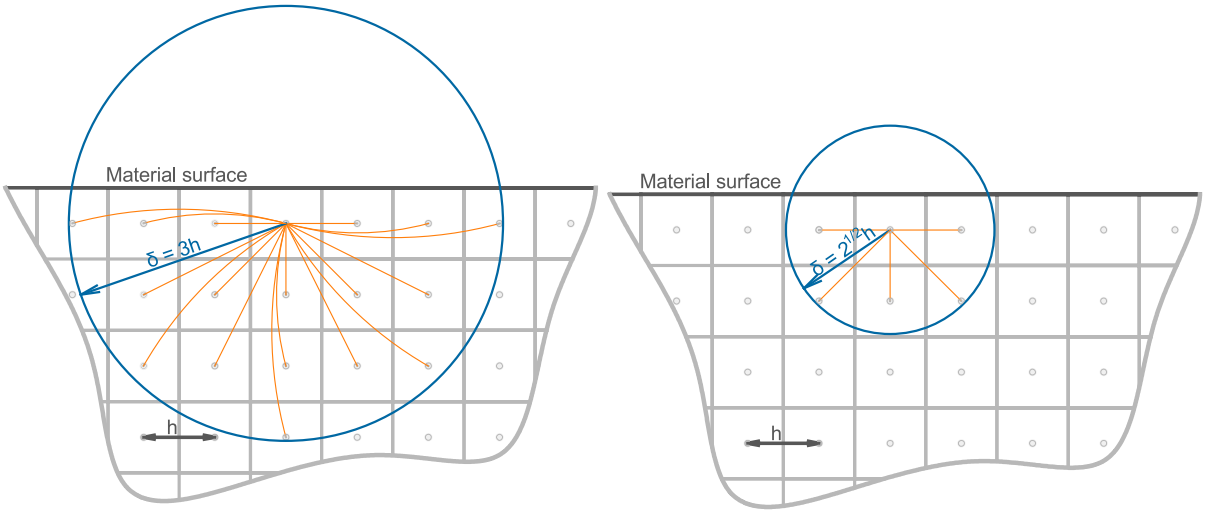

(a) (b)

Figure 5.4. The "surface effect" of a PD node. A node is located on a material surface, so its neighborhood is only partially filled. Some bonds are curved to avoid overlapping. a – $\delta = 3h$, 60.71 % of the neighborhood filled, b - $\delta = \sqrt{2}h$, 62.50 % of the neighborhood filled.

The reduced stiffness in models with a longer horizon is caused by the so-called peridynamic "surface effect". PD material models are derived for a node in bulk of a model i.e. it is assumed that the neighborhood of a node is full with other nodes. When a node is located near an edge of a model or a material surface, its neighborhood is "missing" some nodes and therefore in ordinary state-based PD theory the model may be stiffer or softer on surface than

in bulk along with being slightly anisotropic even when trying to model isotropic material, under non-homogenous deformations [105].

In a 2D PD object, showed in figure 5.4, a node with $\delta = 3h$ (figure 5.4a) next to a material surface has its neighborhood filled by 60.71 %, but, if it's horizon is reduced to $\sqrt{2}h$ (figure 5.4b), then its neighborhood is filled 62.50 %. Since the material model was derived under the assumption of 100 % full neighborhood, stiffness of nodes with a longer horizon are reduced more than the stiffness of nodes with a shorter horizon.

Several studies have tried to remedy this effect to greater or lesser success. The most well-known methods include: the volume method [28], the force density method [27,106], the energy method [27,39,106], the force normalization method [68], position-aware linear solid constitutive model [107], the fictitious nodes method [27,108,109] . For a comparison between different methods, please see [105]. Most of the methods mentioned previously are ad-hoc solutions and their effect depends on the model's geometry, applied BCs, etc. Recently, a promising method that eliminates the need for ad-hoc solutions has been presented in [110].

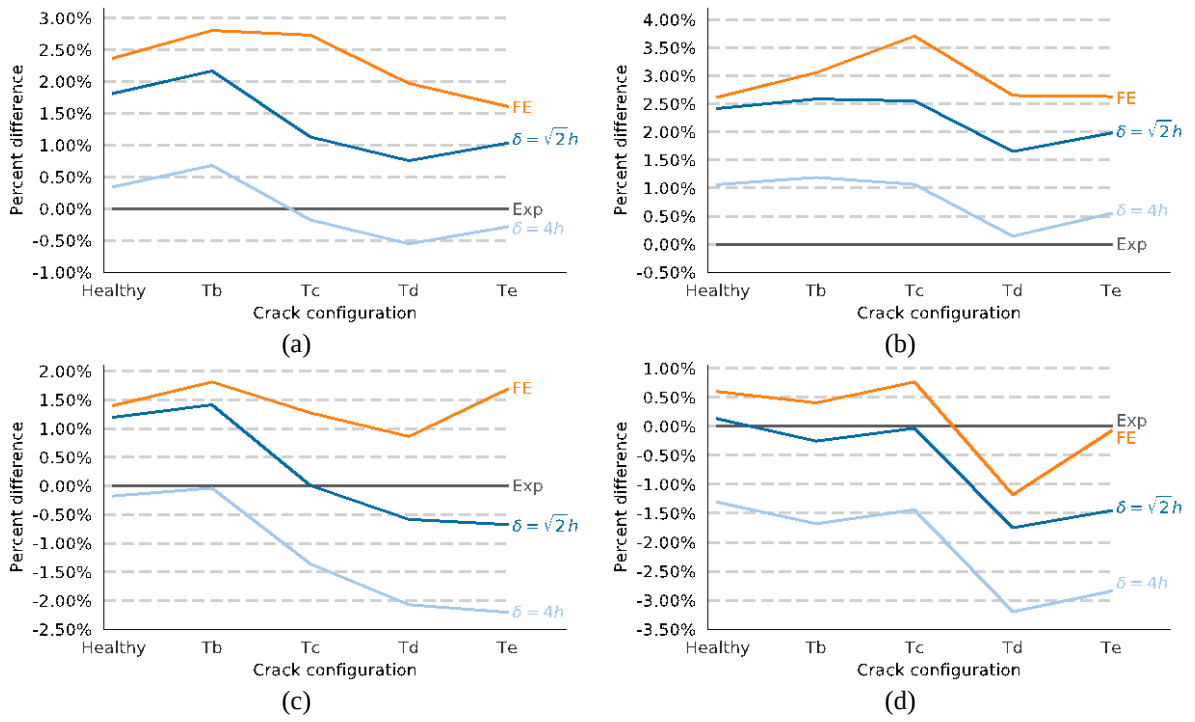

Figure 5.5. The percent difference between PD, experimental, and FE modal frequencies at T crack configurations. a – 1st bending mode, b – 1st torsional mode, c – 2nd torsional mode, d – 2nd bending mode.

The percent difference between PD, experimental and FE modal frequencies at Healthy and T crack configurations are presented in figure 5.5 and table B.3. PD results at Healthy configuration were within a range of -1.31 % to 2.42 %, at Tb configuration within -1.68 % to 2.59 %, at Tc configuration within -1.44 % to 2.55 %, at Td configuration within -3.20 % to 1.65 %, and at Te crack configuration within -2.84 % to 1.98 % of the experimental modal frequencies. The differences between the PD results and the experimental results are very low, which shows that PD modal analysis closely reflects the modal behavior of the test specimens.

PD results are similarly close to the experimental results as the FE results. The difference between PD and experimental results were within -3.20 % to 2.59 %, but between FE and experimental results within -1.20 % to 3.57 %. These ranges are reasonably close, therefore, PD modal analysis is at least just as accurate as FE modal analysis for these test conditions. If separate crack configurations and modes are considered, then the FE results are closer to the experimental results than the PD results only for the 2nd bending mode at Td and Te crack configurations.

Computational models are an idealized representation of test specimens as they do not contain surface cracks, microvoids, and other imperfections. So it was expected that their stiffness would be higher, hence, computed frequencies should be higher. This was not true for all PD frequencies. The computational mass and the specimens' mass should have been almost equal because the computational model and test specimens had roughly the same size (nominal not real dimensions were used for computational models) and the density used in simulations was calculated from the mass measurements, see chapter 4.2. Therefore, the computational stiffness in some cases must have been lower than the real specimen stiffness.

Moreover, the difference between the experimental results and the PD results for the same mode but at different crack configurations were not constant, which means the stiffness reduction in computational models and the specimens must have been different. Most likely it's related to the differences in crack length. Computational models used the nominal crack length, which was different from the crack length in the test specimens. But the differences in results are not large, at most less than two percent-points, so they can be neglected for validation purposes.

The percent difference between PD, experimental and FE modal frequencies at Healthy and S crack configurations are presented in figure 5.6 and table B.4. PD results at Healthy configuration were within the range of -1.31 % to 2.42 %, at Sb configuration within -1.57 % to 2.01 %, at Sc configuration within -1.81 % to 2.12 %, at Sd configuration within -0.20 % to 3.06 %, and at Se crack configuration within -0.10 % to 3.17 % of the experimental modal frequencies. Results for S crack configurations show a lower difference between the PD and the experimental data than the results at T crack configurations. Again confirming that PD modal analysis results closely reflect the experimental modal behavior.

At S crack configurations the difference between the PD and the experimental results ranged between -1.81 % and 3.06 %, but between FE and experimental results between -1.26 % and 2.96 %. While the FE range is smaller, the differences are minuscule. So the accuracy of both numerical methods is roughly the same.

The difference at a single mode between the PD and the experimental results is not constant, therefore, the stiffness reduction from cracks for the computational model and the test specimens is not the same at each crack configuration. The same behavior can be seen in T configuration results. Most likely this is caused by the difference between the nominal and the real crack length.

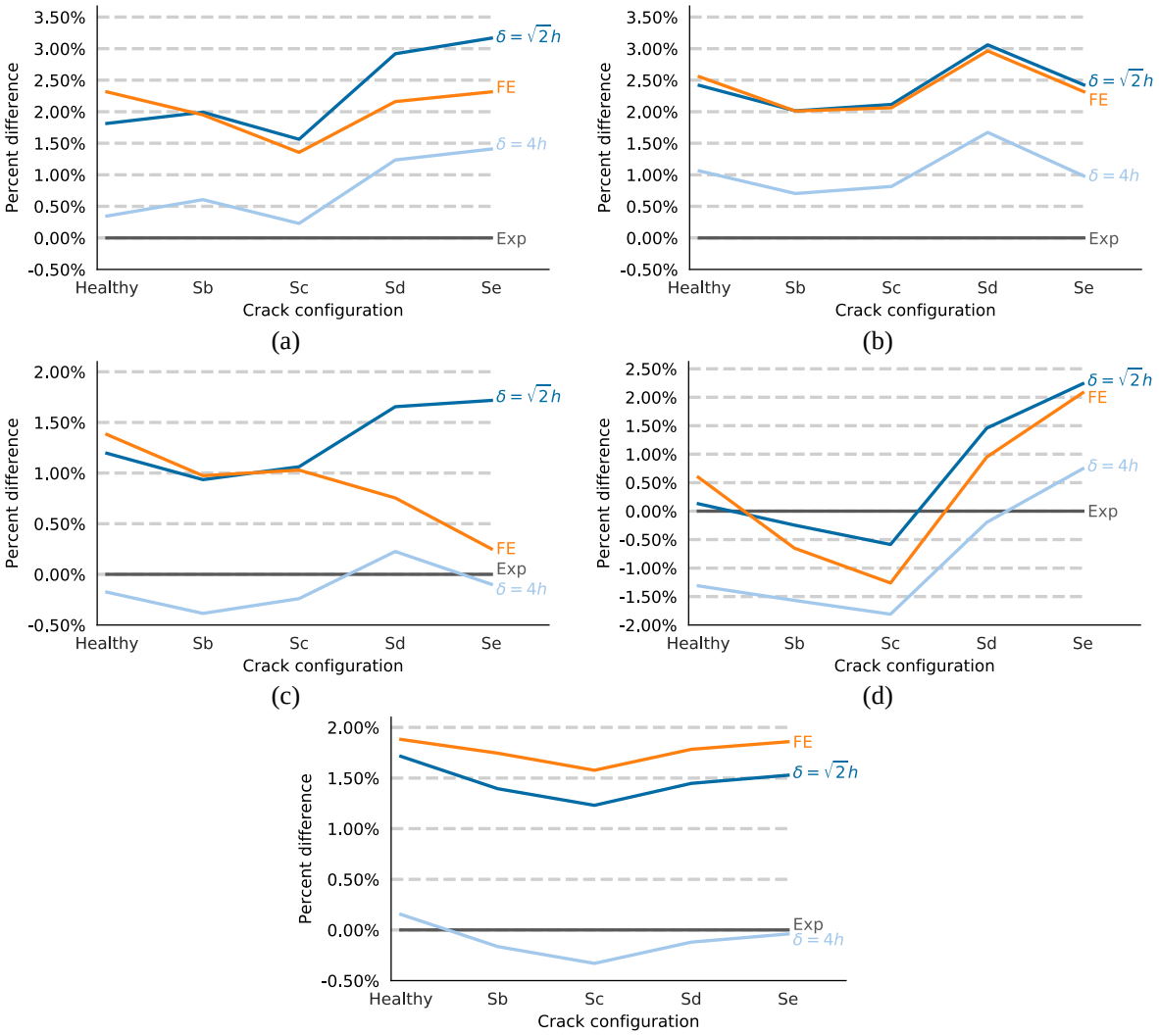

Figure 5.6. The percent difference between PD, experimental, and FE modal frequencies at S crack configurations. a – 1st bending mode, b – 1st torsional mode, c – 2nd torsional mode, d – 2nd bending mode, e – 1st transversal bending mode.

Simulations of the 1st transversal bending mode showed little change in the normalized frequencies between different crack configurations. Since S crack configuration cracks, please see figures 4.7 and 4.8 for details, were parallel to the transversal direction, the effect of them being shallower or deeper on the relevant moment of inertia was very small.

Only six normalized modal frequencies – all four frequencies of the 1st transversal bending mode and the 1st torsional mode's frequencies computed with $\delta = 3h$ or $\delta = 4h$ – were lower at Se crack configuration than at Healthy configuration. Author expected Se crack configuration frequencies to be lower, because both experimental and computational results would experience frequency shift, but only the computational stiffness would be reduced by the PD "surface effect". As the figure 5.5 shows, that is not the case. It is not possible to say why the expected behavior can't be seen, but the likeliest explanation is that the influence of the "surface effect" on the stiffness is small compared to the influence of crack depth. Therefore, differences in crack depth used in simulations and experiments mask the "surface effect".

Frequency shift

The frequency shift is the change in modal frequencies when an object's stiffness changes due to the introduction of damage or other influences. The shift occurs, because an object's material properties or geometric properties have changed. In the presented cases, material properties stayed the same, but the introduced cracks changed the geometrical properties of the computational models or the test specimens.

As will be showed in chapter 6 Convergence studies, models' with denser mesh agree with experimental results better, so this section presents the results from the 625 000 node PD model and from the 664 146 node FE model

Modal frequencies vary between 1000 Hz and 7000 Hz, so their absolute values and the difference between them would depend on the mode in question, therefore, relative frequency shifts will be presented. Modal frequencies were normalized against their respective modal frequency at Healthy configuration and the difference between normalized modal frequency at Healthy configuration and at some other crack configuration was calculated. This way the results are comparable between different modes and crack configurations. For example, for the 1st bending mode when $\delta = \sqrt{2}h$ at Tc crack configuration the value was calculated as

$$\nu_{Tc,n}^{\delta=\sqrt{2}h} = \frac{\nu_{Tc}^{\delta=\sqrt{2}h}}{\nu_{H}^{\delta=\sqrt{2}h}} - 1 = \frac{1382.59}{1697.80} - 1 = 0.8143 - 1 = -18.57\%, \qquad (5.1)$$

where $\nu_{Tc,n}^{\delta=\sqrt{2}h}$ – the relative modal frequency shift at Tc crack configuration,

$\nu_{Tc}^{\delta=\sqrt{2}h}$ – modal frequency computed with $\delta = \sqrt{2}h$ for Tc crack configuration,

$\nu_{H}^{\delta=\sqrt{2}h}$ – modal frequency computed with $\delta = \sqrt{2}h$ for Healthy configuration.

The mode order changed as more damage was introduced, therefore, not the same six modes were computed at all crack configurations. For example, the 1st transversal bending mode was computed only at Healthy and Tb configurations. At Tc, Td, Te configuration other modes such as the 1st in-plane bending mode took its place between the six simulated modes. Four modes – the 1st and 2nd bending mode and the 1st and 2nd torsional mode – were computed at Healthy and all T crack configurations, so these four were studied. The aforementioned four and the 1st transversal bending mode was computed at Healthy and all S crack configurations, so the frequency shift in these five was studied.

Relative frequency shifts at Healthy and T crack configurations are presented in figure 5.7 and table 5.4. The PD results show a very clear frequency shift. At the most damaged – Te – crack configuration the largest shift is for the 2nd torsional mode -40.46 %, but the smallest shift is for the 1st bending mode -25.61 %. The results show a rather large 14.85 percentage point difference. This means that crack influence on the PD models stiffness differs considerably depending on the mode considered.

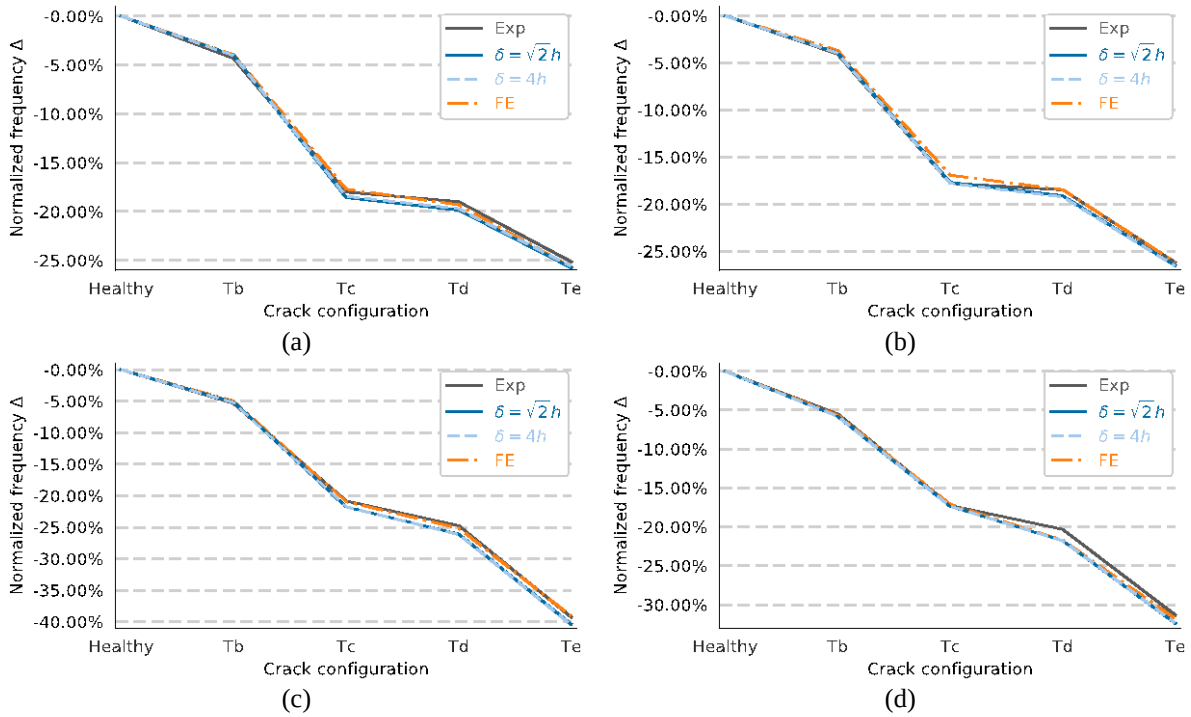

Figure 5.7. Relative frequency shift in T crack configuration specimens. a – 1st bending mode, b – 1st torsional mode, c – 2nd torsional mode, d – 2nd bending mode.

Table 5.4.

The relative frequency shift of the PD, FE, and experimental modal frequencies at Healthy and T crack configurations.

Mode Type		Crack configuration				
		Healthy	Tb	Tc	Td	Te
1st bending	Peridynamic, $\delta = \sqrt{2}h$	0.00%	-4.01%	-18.57%	-19.85%	-25.73%
	Peridynamic, $\delta = 4h$	0.00%	-4.03%	-18.42%	-19.71%	-25.61%
	Finite-element	0.00%	-3.94%	-17.71%	-19.30%	-25.69%
	Experimental	0.00%	-4.35%	-18.00%	-18.99%	-25.13%
1st torsional	Peridynamic, $\delta = \sqrt{2}h$	0.00%	-3.91%	-17.67%	-19.10%	-26.50%
	Peridynamic, $\delta = 4h$	0.00%	-3.95%	-17.78%	-19.21%	-26.55%
	Finite-element	0.00%	-3.67%	-16.91%	-18.44%	-26.16%
	Experimental	0.00%	-4.08%	-17.78%	-18.46%	-26.17%
2nd torsional	Peridynamic, $\delta = \sqrt{2}h$	0.00%	-5.14%	-21.77%	-26.08%	-40.39%
	Peridynamic, $\delta = 4h$	0.00%	-5.22%	-21.76%	-26.15%	-40.46%
	Finite-element	0.00%	-4.96%	-20.93%	-25.15%	-39.09%
	Experimental	0.00%	-5.35%	-20.83%	-24.75%	-39.26%
2nd bending	Peridynamic, $\delta = \sqrt{2}h$	0.00%	-5.82%	-17.37%	-21.79%	-32.38%
	Peridynamic, $\delta = 4h$	0.00%	-5.80%	-17.34%	-21.77%	-32.33%
	Finite-element	0.00%	-5.64%	-17.10%	-21.73%	-31.78%
	Experimental	0.00%	-5.46%	-17.24%	-20.32%	-31.31%

The length of the horizon had a minuscule influence on the PD frequency shift. For the 1st bending mode it was -25.73 % and -25.61 %, for the 1st torsional mode -26.50 % and -26.55 %,

for the 2nd torsional mode -40.39 % and -40.46 %, for the 2nd bending mode -32.38 % and -32.33 % when $\delta = \sqrt{2}h$ and $\delta = 4h$ respectively. Since cracks in a PD model means that there are more material surfaces, the PD "surface effect" should be larger for models with longer cracks and longer horizons. Most likely that is the case, but the stiffness reduction from decreasing cross-section is much larger than from increasing "surface effect".

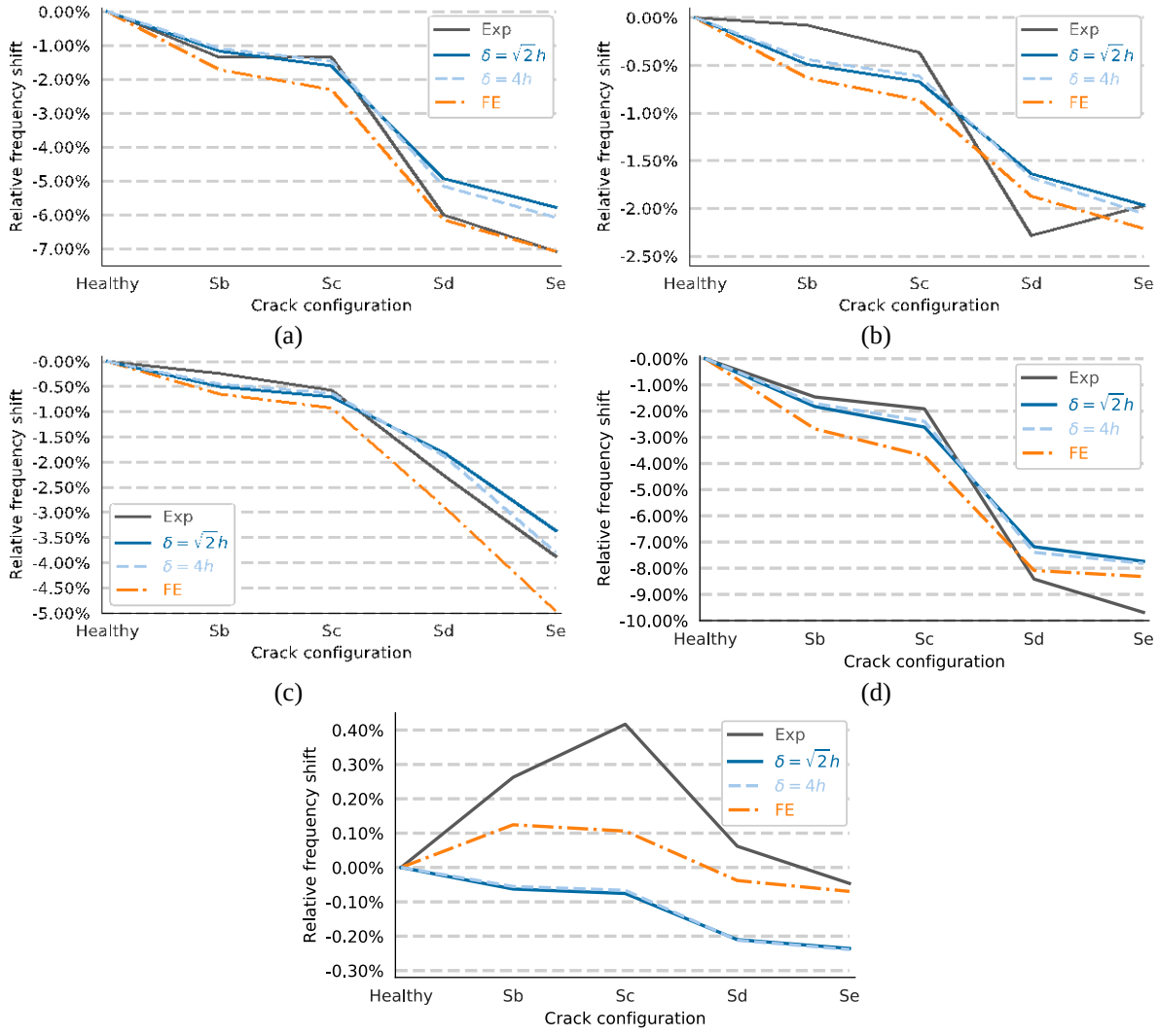

Figure 5.8. Relative frequency shift in S crack configuration specimens. a – 1st bending mode, b – 1st torsional mode, c – 2nd torsional mode, d – 2nd bending mode, e – 1st transversal bending mode.

The agreement between the PD and the FE frequency shift was excellent. The differences between PD and FE frequency shifts ranged between -1.38 and -0.04 percentage points for the 2nd torsional and the 1st bending mode both at Te crack configuration respectively. Such small differences indicate that the stiffness reduction from damage is very similar in PD and FE analyses. However, the peridynamic frequency shift was larger than finite-element frequency shift for all mode-configuration-horizon combinations except one – the 1st bending mode at Te crack configuration with $\delta = 4h$. This shows that the PD stiffness is generally lower than the FE stiffness.

The frequency shifts of the PD and the experimental modal frequencies also agreed very well. The difference between the PD and the experimental relative frequency shifts ranged between -1.47 and +0.34 percentage points for the 2nd bending mode at Td crack configuration and the 1st bending mode at Tb crack configuration respectively. Relative frequency shift differences within such a small range show that PD frequency shifts closely mimic frequency shifts of the experimental test specimens.

Figure 5.8 and table 5.5 presents relative modal frequency shifts at Healthy and S crack configurations. The PD results show a clear frequency shift for all considered modes. The largest PD frequency shift at Se configuration was for the 2nd bending mode -7.82 %, but the smallest was for the 1st transversal bending mode -0.24 %. Similarly, as for T crack configuration results, there is a large 7.58 percentage point difference between the largest and the smallest shift at Te crack configuration, which shows that the stiffness reduction is quite different for different modes.

Table 5.5.

The relative frequency shift of the PD, FE, and experimental modal frequencies at Healthy and S crack configurations.

Mode Type		Crack configuration				
		Healthy	Sb	Sc	Sd	Se
1st bending	Peridynamic, $\delta = \sqrt{2}h$	0.00%	-1.17%	-1.60%	-4.93%	-5.78%
	Peridynamic, $\delta = 4h$	0.00%	-1.09%	-1.47%	-5.15%	-6.08%
	Finite-element	0.00%	-1.72%	-2.31%	-6.15%	-7.08%
	Experimental	0.00%	-1.35%	-1.35%	-6.00%	-7.08%
1st torsional	Peridynamic, $\delta = \sqrt{2}h$	0.00%	-0.49%	-0.67%	-1.64%	-1.96%
	Peridynamic, $\delta = 4h$	0.00%	-0.44%	-0.61%	-1.68%	-2.05%
	Finite-element	0.00%	-0.63%	-0.87%	-1.87%	-2.21%
	Experimental	0.00%	-0.08%	-0.36%	-2.28%	-1.97%
2nd torsional	Peridynamic, $\delta = \sqrt{2}h$	0.00%	-0.50%	-0.71%	-1.81%	-3.36%
	Peridynamic, $\delta = 4h$	0.00%	-0.45%	-0.64%	-1.87%	-3.80%
	Finite-element	0.00%	-0.65%	-0.93%	-2.88%	-4.96%
	Experimental	0.00%	-0.24%	-0.57%	-2.26%	-3.87%
2nd bending	Peridynamic, $\delta = \sqrt{2}h$	0.00%	-1.83%	-2.61%	-7.18%	-7.74%
	Peridynamic, $\delta = 4h$	0.00%	-1.71%	-2.39%	-7.40%	-7.82%
	Finite-element	0.00%	-2.68%	-3.71%	-8.09%	-8.32%
	Experimental	0.00%	-1.46%	-1.92%	-8.41%	-9.69%
1st transversal bending	Peridynamic, $\delta = \sqrt{2}h$	0.00%	-0.06%	-0.08%	-0.21%	-0.24%
	Peridynamic, $\delta = 4h$	0.00%	-0.06%	-0.07%	-0.21%	-0.24%
	Finite-element	0.00%	0.12%	0.11%	-0.04%	-0.07%
	Experimental	0.00%	0.26%	0.42%	0.06%	-0.05%

For S crack configuration simulations just as for T configurations' simulations, different horizon lengths didn't influence the PD frequency shifts much. The largest difference between PD shifts when $\delta = \sqrt{2}h$ and when $\delta = 4h$ is 0.44 percentage points at 2nd torsional mode. It

is larger than at T crack configurations, but still small. Which shows that stiffness reduction due to peridynamic "surface effect" is smaller than the reduction due to created cracks.

The agreement between the PD and the FE results was similar to that at T crack configurations. The difference in relative modal frequency shifts ranged between -0.19 and 1.30 percentage points for the 1st transversal bending mode at Sb configuration and the 1st bending mode at Se configuration respectively. This shows that the stiffness reduction from cracks in PD models is close to the stiffness reduction in the FE models. PD and FE graphs in figure 5.8 might seem to agree worse than in figure 5.7, however, when a numerical difference is calculated, it can be seen that the agreement is similar. Plots in figure 5.7 show much wider relative frequency shift range on the y scale thus making any differences between PD and FE results less noticeable.

The differences between the PD and the experimental relative frequency shifts were within -0.70 to +1.95 percentage point range showing an excellent agreement. The difference between the PD and the experimental shifts grows as the cracks with each sequential crack configuration. The 1st transversal bending mode is an exception, which is discussed below. The average difference between all PD relative frequency shifts and all experimental relative frequency shifts increased from 0.21 percentage points at Sb configuration to 0.33, 0.57, and 0.63 percentage points at configurations Sc, Sd, and Se respectively. Therefore, the stiffness reduction caused by cracks is slightly different between the PD analysis and the experimental tests.

For the 1st transversal bending mode, the PD modal frequencies were lower at each sequential crack configuration. This is the behavior that the author expected because as the crack become longer and deeper the stiffness is reduced thus modal frequencies decrease. However, the experimental and FE modal frequencies increased between Healthy, Tb, and Tc configurations. The increase in the experimental modal frequencies could be explained by slightly different BCs in different tests, but this explanation doesn't work for the increase in FE modal frequencies because no BCs were applied. At present, the author can't explain this behavior. But it is noted that the frequency shift for the 1st transversal mode was much lower than for other modes. The PD frequencies shifted only by -0.24 percentage points. The cracks ran parallel to the bending direction, therefore, the reduction in the transversal bending stiffness caused by cracks would have been limited.

5.2 Mode shapes

This subchapter verifies and validates PD mode shapes against FE and experimental mode shapes. First, mode shapes at different crack configurations will be presented, followed by a discussion about the mode order and its changes as the damage increases. 864 mode shapes were computed using PD analysis, 54 – using FE analysis, and 240 mode shapes were measured with the testing equipment.

Three different computer programs – Paraview, Ansys, and Polytec Scan Viewer – were used to visualize the PD, FE and experimental mode shapes respectively. The programs used

similar, but not completely identical, color schemes. The color distribution in the mode shapes, therefore, can appear slightly different.

Verification of PD mode shapes

Mode shapes for Healthy, Tc, Te, Sc, and Se crack configurations will be presented. The author chose to not present them at all crack configurations because little useful information would be added so they would take up too much space in the thesis without adding extra information. These five crack configurations were chosen because they represent the undamaged case, the two most damaged cases and two cases between them.

For some modes, the PD and the FE mode shapes are similar but inverse. As an example, please see figures 5.10a and 5.10g. The mode in question is the 1st bending mode. Both the PD and the FE shape show the same bending form, yet they are bent towards opposite directions. Such a situation happens because an eigensolver can converge to either of two distinct eigenvectors (mode shapes) for a single eigenvalue (modal frequency). These vectors have the same values in magnitude, but opposite signs, so one vector will be denoted with a (+) sign but the other one with a (-) sign. The FE solver converged to the (+) eigenvector, whereas PD solver converged to the (-) eigenvector. Mode shapes (+) and (-) represent the exact same shape only at different extremes.

Figures 5.10 through 5.14 show the PD and the FE mode shapes at Healthy, Tc, Te, Sc, and Se configurations respectively. A color legend with numerical values can't be provided, because a mode shape is a dimensionless representation of a structure vibrating at a modal frequency. Figures presenting mode shapes show the displacement field in the model for a particular mode shape. Red color shows the extreme displacements, but blue color shows displacements close to zero, the whole color scheme is shown in figure 5.9.

Figure 5.9. The color scheme used in figures 5.10. through 5.14.

PD modal analysis and FE modal analysis yielded the same mode shapes at all crack configurations. At Healthy configuration, in figure 5.10, the mode order was: the 1st bending, the 1st torsional, the 2nd torsional, the 2nd bending, the 1st transversal bending and the 1st in-plane bending mode. The mode shape displacement field is regular and the zero displacement areas (in blue) are roughly parallel or orthogonal to the three coordinate axes.

At Tc crack configuration, figure 5.11, the mode order was: the 1st bending, the 1st torsional, the 1st in-plane bending, the 2nd torsional, the 2nd bending, the 3rd torsional mode.

At Te crack configuration, figure 5.12, the mode order was: the 1st bending, the 1st torsional, the 2nd torsional, the 1st in-plane bending, the 2nd bending, the 2nd in-plane bending mode.

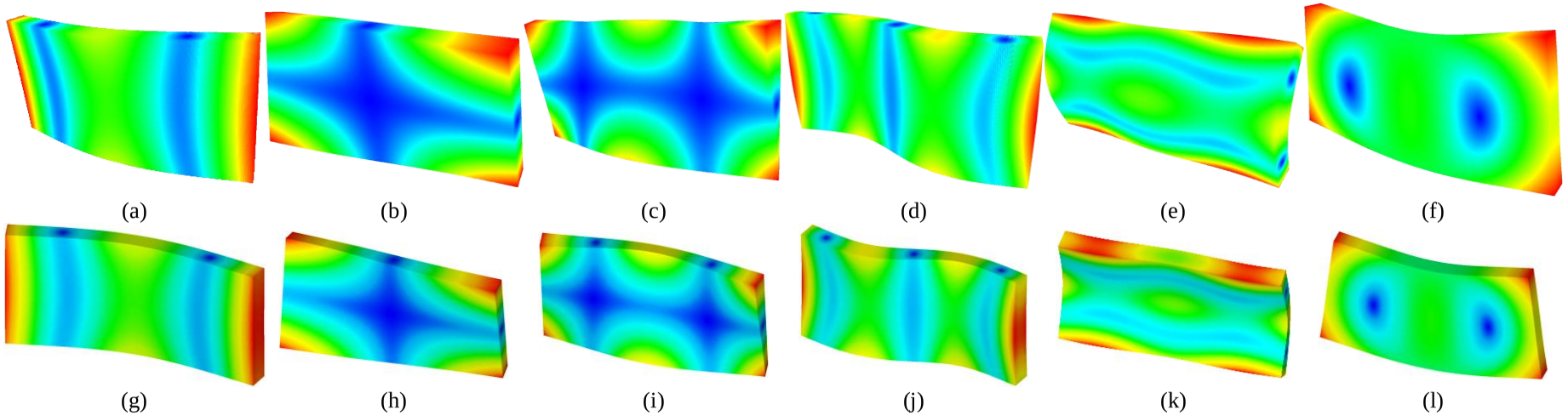

Figure 5.10. PD and FE mode shapes at Healthy configuration. Top – PD mode shapes, bottom – FE mode shapes. a, g – 1st bending mode, b, h – 1st torsional mode, c, i – 2nd torsional mode, d, j – 2nd bending mode, e, k – 1st transversal bending mode, f, l – 1st in-plane bending mode.

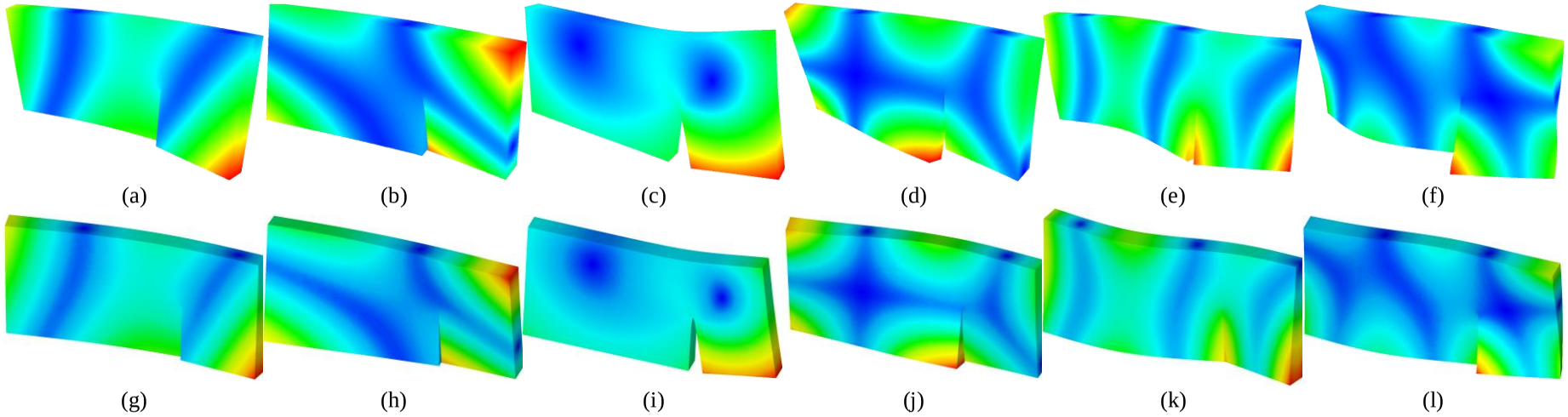

Figure 5.11. PD and FE mode shapes at Tc configuration. Top – PD mode shapes, bottom – FE mode shapes. a, g – 1st bending mode, b, h – 1st torsional mode, c, i – 1st in-plane bending mode, d, j – 2nd torsional mode, e, k – 2nd bending mode, f, l – 3rd torsional mode.

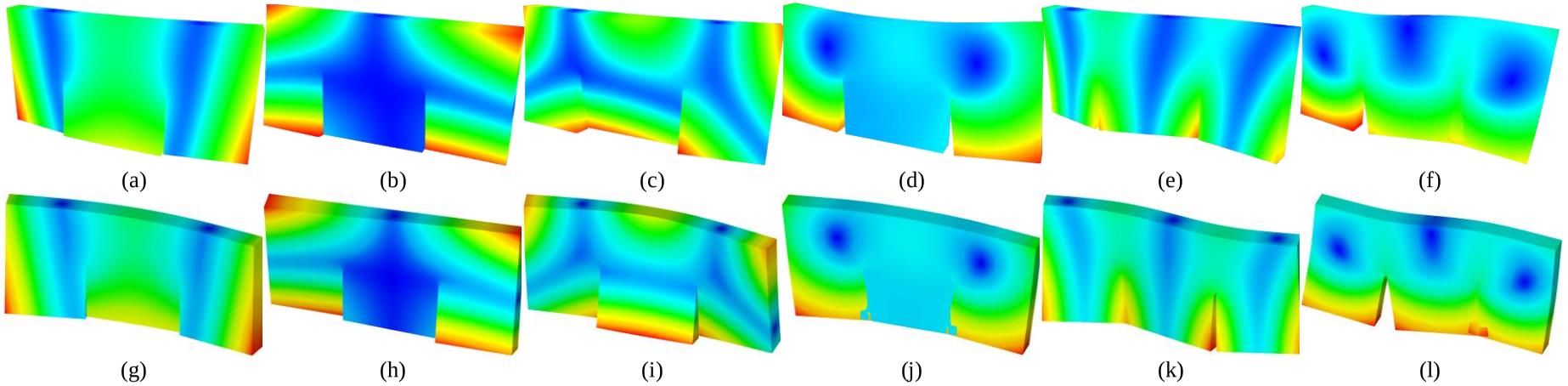

Figure 5.12. PD and FE mode shapes at Te configuration. Top – PD mode shapes, bottom – FE mode shapes. a,g – 1st bending mode, b, h – 1st torsional mode, c, i – 2nd torsional mode, d, j – 1st in-plane bending mode, e, k – 2nd bending mode, f, l – 2nd in-plane bending mode.

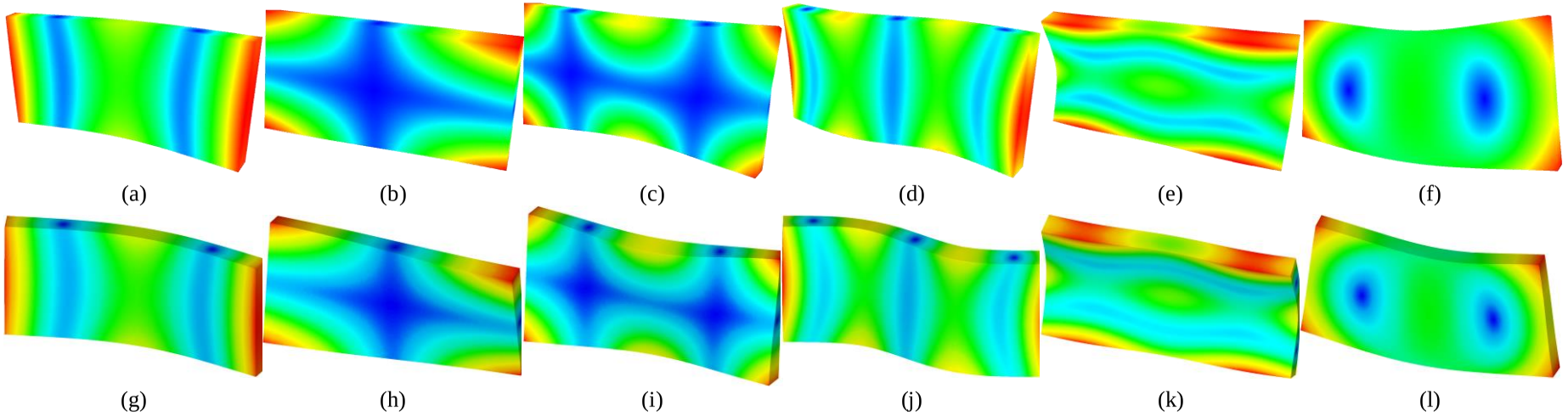

Figure 5.13. PD and FE mode shapes at Sc configuration. Top – PD mode shapes, bottom – FE mode shapes. a,g – 1st bending mode, b, h – 1st torsional mode, c, i – 2nd torsional mode, d, j – 2nd bending mode, e, k – 1st transversal bending mode, f, l – 1st in-plane bending mode.

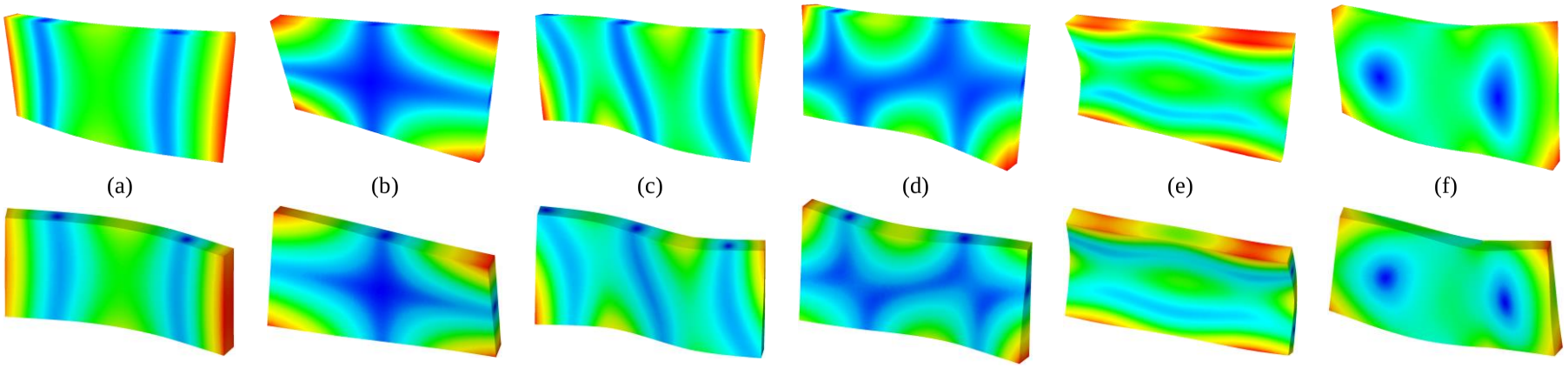

Figure 5.14. PD and FE mode shapes at Se configuration. Top – PD mode shapes, bottom – FE mode shapes. a,g – 1st bending mode, b, h – 1st torsional mode, c, i – 2nd bending mode, d, j –2nd torsional mode, e, k – 1st transversal bending mode, f, l – 1st in-plane bending mode.

The mode order at Healthy, Tc, and Te crack configurations is different. However, it is the same in PD and FE results at every single crack configuration. Introduced cracks changed the model's stiffness, but stiffness acting against different kinds of deformations was changed differently. The in-plane bending stiffness was reduced more than other stiffness, therefore, in-plane bending mode's modal frequencies experienced larger frequency shift and the 1st in-plane bending mode shifted from being the sixth mode at Healthy configuration to the third position at Tc configuration and the fourth position at the Te configuration. Similarly, the 2nd in-plane bending mode, which wasn't between the six simulated modes at Healthy and Tc crack configurations, appeared at Te crack configuration and the 3rd torsional mode appeared in the Tc crack configuration results.

The introduced cracks created a sudden discontinuity in the displacement field and the displacement field shifted in response. As an example, please see figures 5.10b, 5.10h, 5.11b, 5.11h, and 5.12b, 5.12h. For the 1st torsional mode at Healthy configuration the maximum displacements are located at the four corners of the model, at Tc configuration they are located at the top right and the bottom left corner and to the right from the created crack, lastly at Te configuration maximum displacements again are located at the two top corners, and also at the whole bottom side to the left from the left crack and to the right from the right crack. Such changes in the displacement can be seen for all mode shapes at T crack configurations.

At Sc crack configuration, figure 5.13, the mode order was: the 1st bending mode, the 1st torsional mode, the 2nd torsional mode, the 2nd bending mode, the 1st transversal bending mode, the 1st in-plane bending mode.

At Se crack configuration, figure 5.14, the mode order was: the 1st bending mode, the 1st torsional mode, the 2nd bending mode, the 2nd torsional mode, the 1st transversal bending mode, the 1st in-plane bending mode.

The mode order at Healthy and Sc crack configuration is the same, but the 2nd torsional and the 2nd bending mode switched places between the third and the fourth position. Still, the PD analysis and the FE analysis resulted in the same mode order at each separate crack configuration.

Also at S configurations, the displacement fields shifted as a result of the introduced cracks, however, not for all modes. There is no visible change in the 1st bending, the 1st torsional, and the 1st transversal bending modes. For the 2nd torsional mode at Se crack configuration, figures 5.14d and 5.14j, the zero displacement area to the left has visibly shifted downwards when compared the Healthy and Sc configurations.

Cracks were visible in all PD and FE mode shapes at T crack configurations. That was not the case at S crack configurations. They were not visible, but only because the cracks were located on the back face of the model. Had the mode shapes been presented differently they would have been visible. Ultimately, the way the mode shapes were presented doesn't impact the results.

Validation of the PD mode shapes

Only 2D modes could be obtained from the experimental analysis due to limitations of the available equipment. The author chose to present also the PD modes in 2D so that they can be

compared with the experimental data more easily. Moreover, the in-plane bending modes couldn't be captured, because the available 2D laser vibrometer can only measure in the out-of-plane dimension. They will not be presented in the PD results either.

The color scheme used in this subchapter represents displacement in the out-of-plane direction (z-axis), but in the previous subchapter, it represented the sum of all displacements. Therefore, the color scheme used here is different. Numerical values can't be used for the reasons that were discussed in the previous subchapter. The color scheme is presented in figure 5.15.

Figure 5.15. The color scheme used in figures 5.16 through 5.20.

Five specimens were measured in experimental modal analysis, but only one mode shape from them will be presented. The one that, based on the author's opinion, best illustrates the expected mode shape.

Mode shapes will be presented in separate modes like in chapter 5.1 Modal frequencies not in separate crack configurations like the previous subchapter. This way was chosen because it is better for checking if the changes in the displacement fields from the evolving damage are similar between the PD and the experimental analysis.

Experimental and PD mode shapes at Healthy and T crack configurations are presented in figures 5.16 through 5.19 for the 1st bending, the 1st torsional, the 2nd bending and the 2nd torsional mode respectively. The reasons for presenting only these four are discussed in subchapter Verification and validation of the PD modal frequencies.

Figure 5.16 presents mode shapes of the 1st bending mode at Healthy, Tb, Tc, Td, and Te crack configurations. Both mode shapes at Healthy configuration appear similar. The extreme displacements are located in the middle and at both ends. At Tb crack configuration locations of the extreme displacements have not moved, but a crack is clearly visible in the PD mode shape. Next, at Tc and Td crack configurations both experimental and PD mode shapes present a clear crack as a sudden jump in displacement. On the right side, from the bottom till the middle, but on the left side, the crack is present only at Td crack configuration and is visible only in the PD modes shape. The displacement field is skewed towards the crack on the right side in both experimental and PD shapes compared to displacements of the respective mode shapes at Healthy configuration. Additionally, extreme displacements at both ends of the specimens have shifted to corners. Last, at Te crack configuration mode shapes are slightly asymmetric because the two cracks were not positioned symmetrically against the centerline. Cracks are visible in both experimental and PD shapes as a sudden jump in displacements. The extreme displacements on both ends of the plate are not located just in corners anymore but are more spread out along the short side.

Mode shapes of the 1st torsional mode are shown in figure 5.17. Both mode shapes at Healthy configuration are similar to the extreme displacements in the four corners. At Tb

configuration the introduced crack can be seen in PD shape, but not in the experimental one. Also, the displacement areas (in blue) adjacent to the corner with the crack are visibly smaller than in the Healthy configuration. Next, mode shapes at Tc and Td configurations are significantly different from mode shapes at Healthy and Tb configurations. The crack on the right side is clearly visible in both experimental and PD results. Also, the shorter crack on the left at Td configuration can be seen in both results. Contrary to mode shapes of Healthy and Tb configuration, extreme displacements have moved from the lower right corner towards the longest crack. Lastly, mode shapes at Te configuration appear symmetric. Both cracks are visible in mode shapes as sharp drops in displacement. Extreme displacements again are located in the corners of a specimen.

Figure 5.18 shows the experimental and PD mode shapes for the 2nd torsional mode. Introduced cracks can be seen in both experimental and PD mode shapes at all configurations. Furthermore, displacements are similar between respective experimental and PD mode shapes at each crack configuration. At Tb crack configuration extreme displacements are located at four corners and in the middle of the long edges of a model. However, as the crack becomes longer extreme displacement locations move towards the crack. At configurations, Tc and Td displacement areas at the top of a specimen have moved slightly to the right. Additionally, displacement areas at top left corner and top middle have become larger, but the area at the top right corner has shrunk. At Te crack configuration both top corner areas are stretched downward, but the top middle displacement area has shrunk.

Lastly, the mode shapes of the 2nd bending mode are presented in figure 5.18. Displacement field in both PD and experimental mode shapes skews slightly when cracks are introduced. Additionally, PD mode shapes show extreme displacements at the same locations as experimental mode shapes.

Cracks were clearly visible in all PD mode shapes, but not in all experimental mode shapes. Displacement values in the experimental mode shapes were computed at specified points on the surface of a specimen and the values between these points were interpolated. When displacement values on both sides of a crack are similar, the discontinuity will not be clear, because it will be smoothed by interpolation between the measurement points. As an example, please see figures 5.19b and 5.19g. A crack is clearly visible in the PD mode shape but can’t be seen in the experimentally measured mode shape. Measurement points were positioned on both sides of the crack. but, since the crack is located close to the extreme displacement, measured values are similarly large on both sides, so there is no clear jump in displacements between the two sides of the crack.

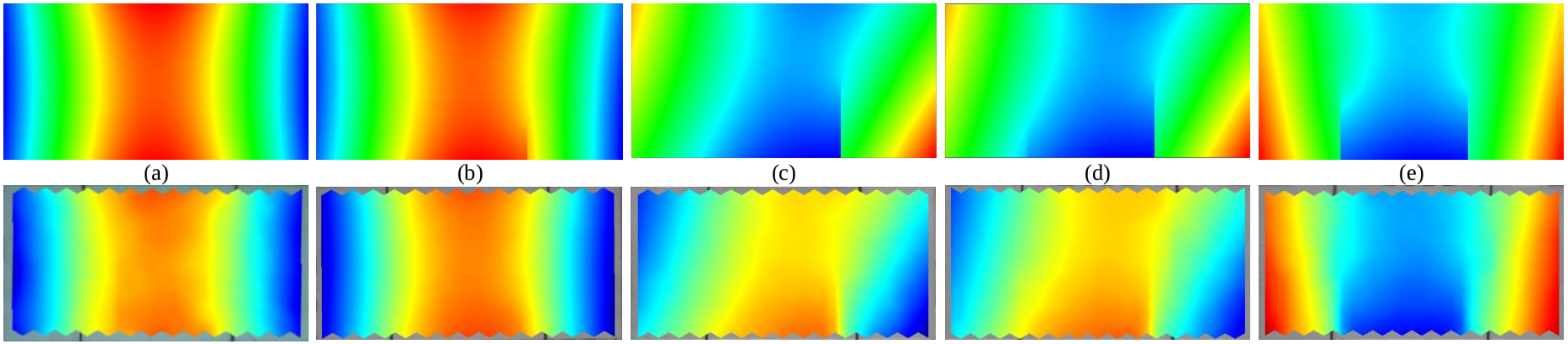

Figure 5.16. Mode shapes of the 1st bending mode. Top – PD mode shapes, bottom – experimental modes shapes. a, f – Healthy; b, g – Tb; c, h – Tc; d, i – Td; e, j – Te configuration

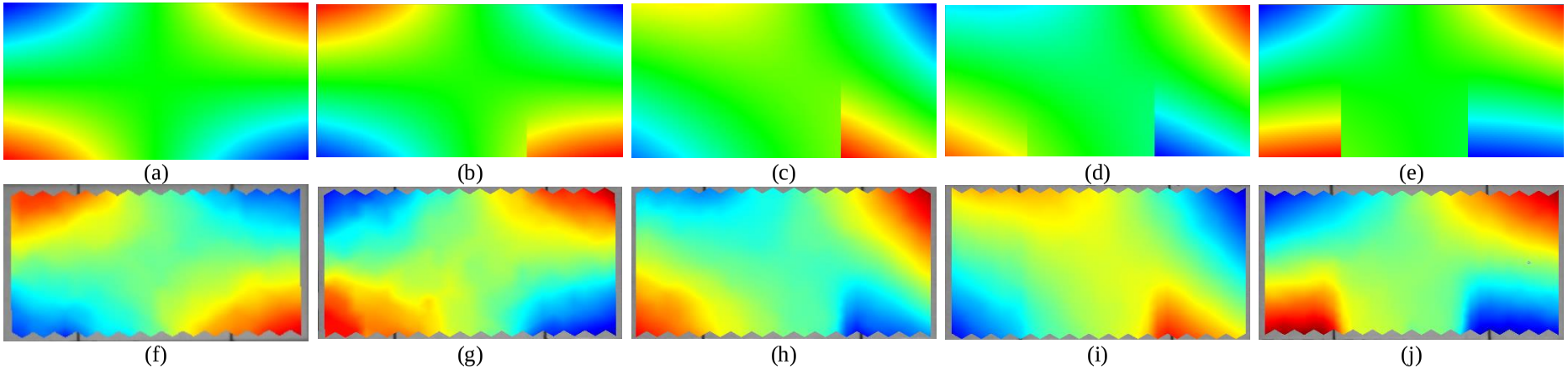

Figure 5.17. Mode shapes of the 1st torsional mode. Top – PD mode shapes, bottom – experimental modes shapes. a, f – Healthy; b, g – Tb; c, h – Tc; d, i – Td; e, j – Te configuration.

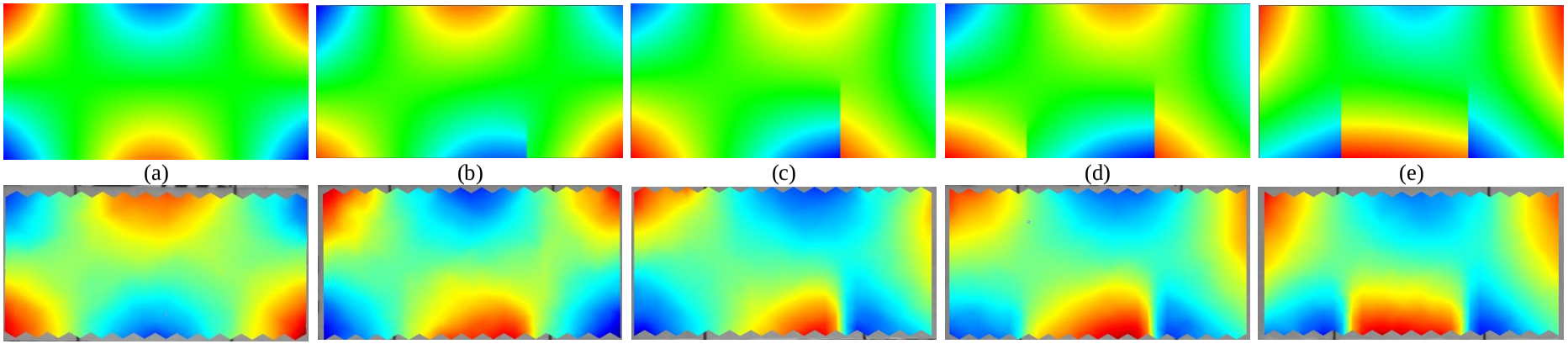

Figure 5.18. Modes shapes of the 2nd torsional mode. Top – PD mode shapes, bottom – experimental modes shapes. a, f – Healthy; b, g – Tb; c, h – Tc; d, i – Td; e, j – Te configuration.

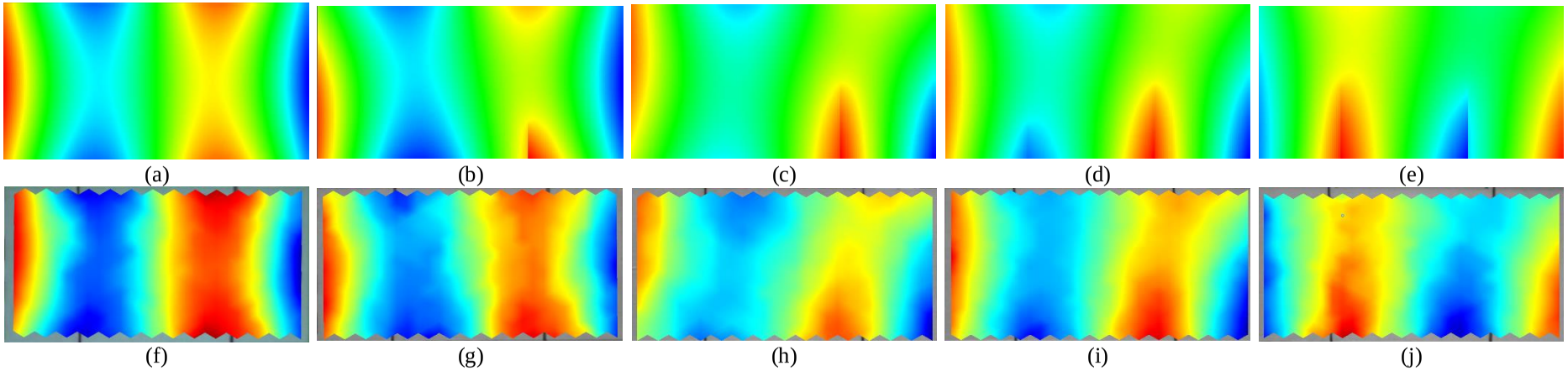

Figure 5.19. Mode shapes of the 2nd bending mode. Top – PD mode shapes, bottom – experimental modes shapes. a, f – Healthy; b, g – Tb; c, h – Tc; d, i – Td; e, j – Te configuration.

Conversely, when a crack is not located at an extreme, then a discontinuity in displacements is visible. Such as in figures 5.18c and 5.18h. The crack on the right side of a specimen is clear in both the experimental and the PD mode shapes. The difference in values measured on both sides of the crack has been large enough that clear jump between them can be seen.

Possibly better results could be achieved with finer measurement mesh because it would reduce interpolation lengths and the more distinct features of the displacement field could be seen. On the other hand, it would also increase the measurement time. Ultimately, whether or not discontinuities are captured in the experimental mode shapes is not important because the aim was to validate the PD mode shapes and they agree with the experimental mode shapes well.

Cracks in S configurations were manufactured into the back face of a specimen, not through specimen thickness. Therefore, they didn't appear on the specimen surface, so they would not appear as a jump in displacements. Their effect on the modal properties will only be visible if they cause a shift in the displacement field.

Figures 5.20, 5.21 and 5.22 presents mode shapes for the 1st bending mode, the 1st torsional mode and the 1st transversal bending mode respectively. For these three modes, no clear changes in the mode shape between Healthy and other crack configurations can be seen.

Figure 5.23 shows the mode shapes of the 2nd torsional mode. Healthy, Sb and Sc crack configuration mode shapes all appear similar with no visible changes. At Sd crack configuration the crack on the right side of a specimen is deepened from 1.204 mm to 2.577 mm and a visible shift appears in the PD mode shape. Displaced areas at the top middle and bottom middle of a specimen move slightly to opposite sides, see figure 5.23b second from right. However, such a shift is not clearly visible in the experimental mode shape. Lastly, at Se crack configuration all cracks are 2.577 mm deep and not only PD mode shape has visibly shifted, but also the top middle and bottom middle displacement areas have shifted slightly to opposite sides in the measured mode shape.

Figure 5.24 presents the mode shapes of the 2nd bending mode. Healthy and Sb crack configuration mode shapes show little change between them. The experimental mode shape at the Sb configuration is skewed slightly towards the left side. Contrary, such a shift is not clearly visible in the PD mode shape. When the cracks are deepened at Sd and Se crack configurations a clear change in mode shapes can be seen. Maximum displacement zones that were parallel to specimens' long edge have now slightly moved to the right.

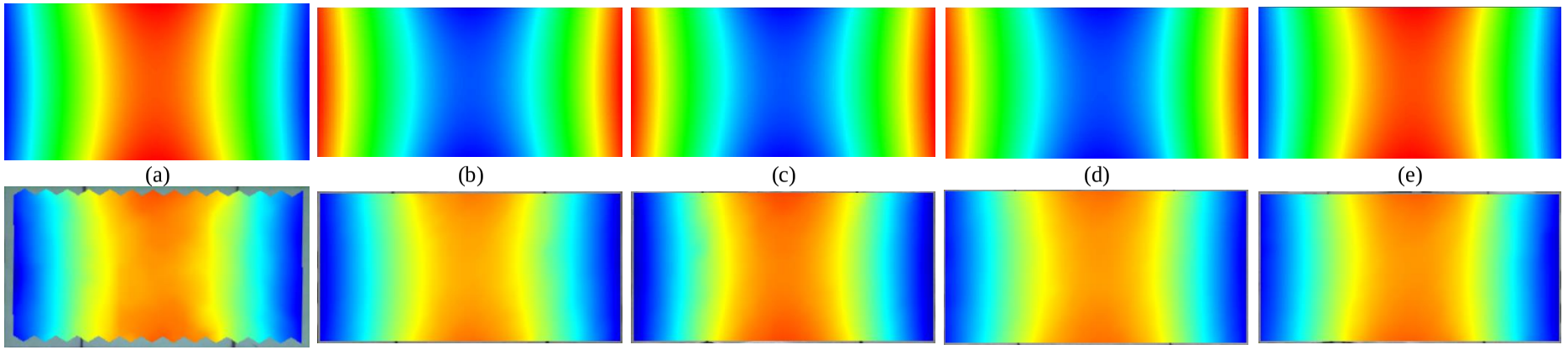

Figure 5.20. Mode shapes of the 1st bending mode. Top – PD mode shapes, bottom – experimental modes shapes. a, f – Healthy configuration; b, g – Sb configuration; c, h – Sc configuration; d, i – Sd configuration; e, j – Se configuration.

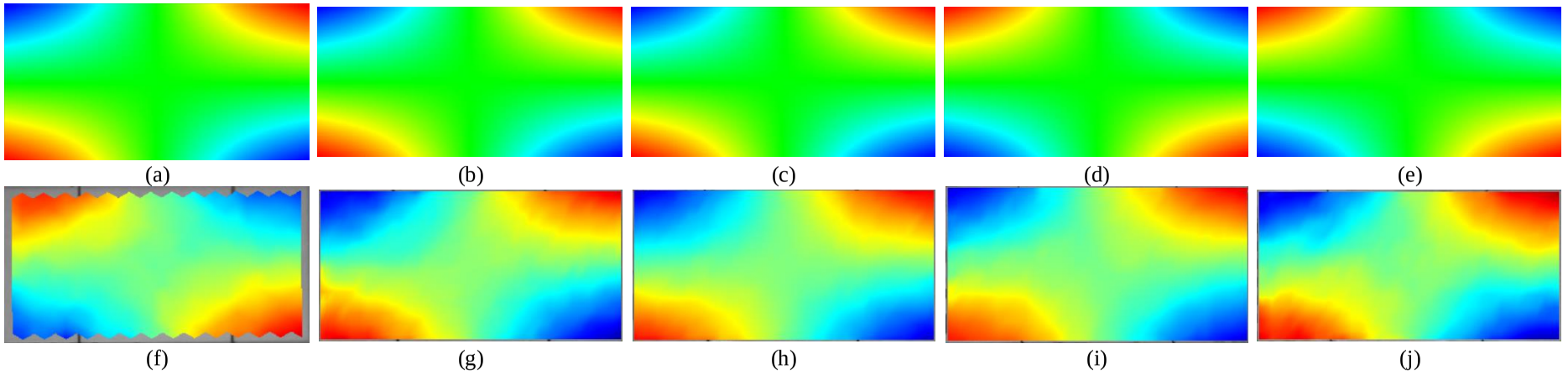

Figure 5.21. Mode shapes of the 1st torsional mode. Top – PD mode shapes, bottom – experimental modes shapes. a, f – Healthy configuration; b, g – Sb configuration; c, h – Sc configuration; d, i – Sd configuration; e, j – Se configuration.

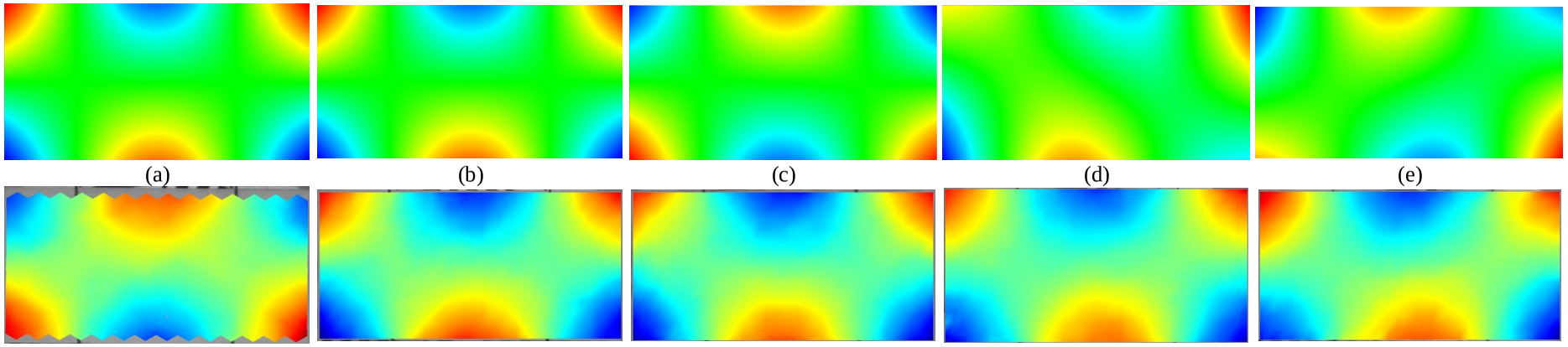

Figure 5.22. Mode shapes of the 2nd torsional mode. Top – PD mode shapes, bottom – experimental modes shapes. a, f – Healthy configuration; b, g – Sb configuration; c, h – Sc configuration; d, i – Sd configuration; e, j – Se configuration.

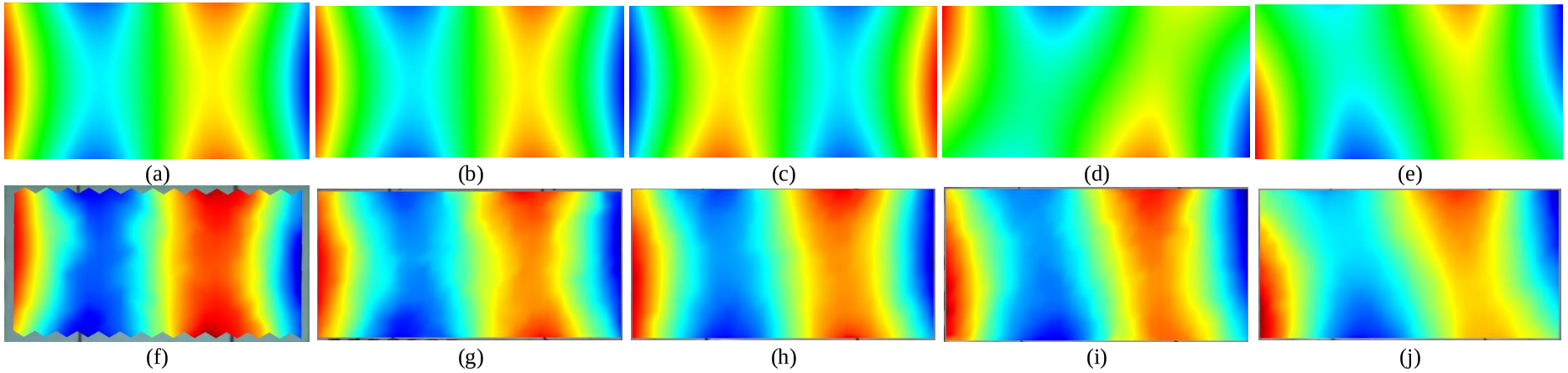

Figure 5.23. Mode shapes of the 2nd bending mode. Top – PD mode shapes, bottom – experimental modes shapes. a, f – Healthy configuration; b, g – Sb configuration; c, h – Sc configuration; d, i – Sd configuration; e, j – Se configuration.

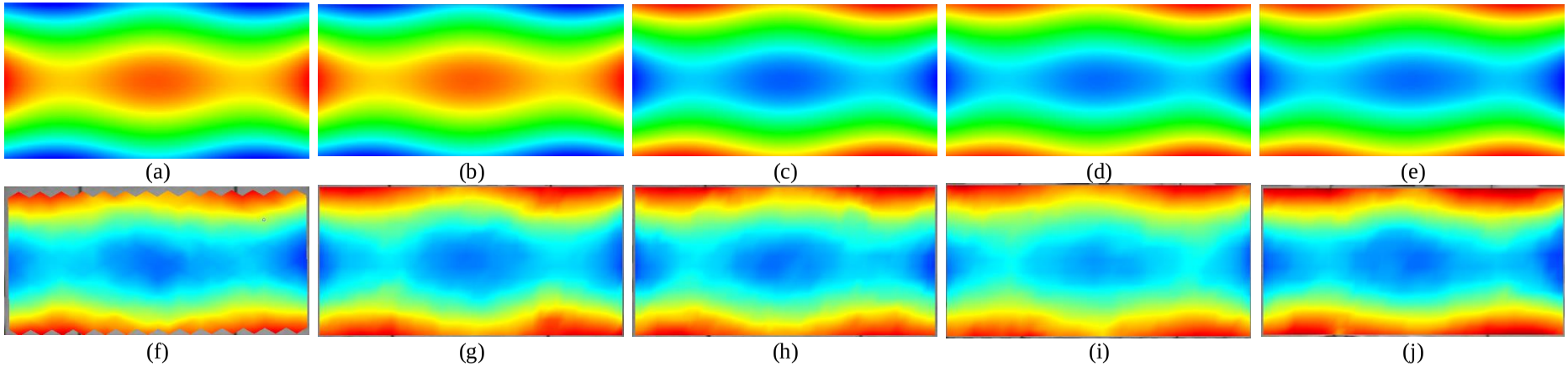

Figure 5.24. Mode shape of the 1st transversal bending mode. Top – PD mode shapes, bottom – experimental modes shapes. a, f – Healthy configuration; b, g – Sb configuration; c, h – Sc configuration; d, i – Sd configuration; e, j – Se configuration.

6 CONVERGENCE STUDIES

Every acceptable numerical method should converge or at least tend to the exact local or non-local solution, thus meshes with a higher number of nodes i.e. a smaller node spacing should produce more accurate results at an increased computational cost. Mesh or grid convergence is, therefore, studied to determine the lowest number of nodes in a model with an acceptable discretization error.

In the numerical analysis, the term "convergence" is commonly used in two different ways. One is the mesh convergence, which is related to errors arising from model discretization, and the other one is the iterative convergence, which is related to the accuracy or the speed of the numerical solution. In this chapter, only the mesh convergence is considered.

6.1 Discretization error

A model has some number of nodes m and the inverse property – mesh spacing – is h. If mesh spacing is the same along all three coordinate axes, the so called "cubic" nodes, then:

$$m = \frac{V}{h^3}, \tag{6.1}$$

where V – the volume of a model. Conventionally, a mesh with a lower number of nodes is called coarse or less dense and a mesh with a higher number of nodes is called fine or denser.

Discretization error is an error that arises when a function of a continuous variable is represented by a finite number of evaluations. As the mesh spacing decreases i.e. $h \to 0$ the discretization error should asymptotically approach zero and only computer round-off errors should remain. Discretization error can be written as

$$E = |f_0 - f(h)|, \tag{6.2}$$

where E – discretization error,

f_0 – computed value at zero mesh spacing (continuum value),

$f(h)$ – computed value at current mesh spacing.

An excellent review of uncertainty, which includes discretization errors in numerical analysis, is available in [111,112].

The order of convergence p can be computed from

$$E = |f_0 - f(h)| = Ch^p, \tag{6.3}$$

where C – a constant,

p – order of convergence.

Moreover, convergence is asymptotic, thus (6.3) has to hold only when $h \to 0$, so it is unlikely that a single C and p such that (6.3) holds for every h will be found. In practical applications, researchers are only interested in finding sufficiently small h values, so that discretization error is negligible. This is called the asymptotic range of convergence and it is obtained when the

mesh spacing is so small that various mesh spacings h and errors E results in the constancy of C, where

$$C = \frac{E}{h^p}. \tag{6.4}$$

In PD three types of convergence can be defined [113]:

- The δm-convergence where $\delta \to 0$ and m increases as δ decreases, with m increasing faster than δ decreases. The numerical PD solution will converge to the analytical PD solution and converge to the local continuum mechanics solution.
- The m-convergence where δ is fixed and $m \to \infty$. In this case, the PD solution converges to the exact non-local PD solution for a given δ.
- The δ-convergence where $\delta \to 0$ and m is fixed or increases with decreasing δ. In this case, the PD solution converges to and approximation of the continuum mechanics solution.

It must be noted that in a computational model the horizon δ is required to cover more than its own node, so it cannot shrink to zero. In these thesis the shortest horizon used is $\delta = \sqrt{2}h$.

Two convergence studies – δ and δm – were done. All mesh and horizon combinations are showed in table 3.1. In the δ-convergence study, mesh density was held constant at either 40 000, 135 000, 320 000 or 625 000 nodes while the horizon shrank from $\delta = 4h$ to $\delta = \sqrt{2}h$. But in the δm-convergence study the horizon was held constant at either $\delta = \sqrt{2}h$, $\delta = 2h$, $\delta = 3h$ or $\delta = 4h$ while the mesh density increased from 40 000 to 625 000 nodes. Since mesh spacing h decreases as the mesh density m grows, the absolute value of the horizon also decreases. For example, if the horizon $\delta = \sqrt{2}h$ and the mesh density increases from 40 000 nodes to 625 000 nodes then the absolute value of the horizon shrinks from 0.03162 m to 0.02 m.

For many practical problems, it is impossible to compute the value at zero mesh spacing due to prohibitive computational cost. Richardson extrapolation can be used in such cases to obtain a higher order estimate of the value at zero mesh spacing from a series of lower-order discrete values. A computed value $f(h)$ is expressed in a general form by the series expansion:

$$f(h) = f_0 + a_1 h + a_2 h^2 + a_3 h^3 + \cdots, \tag{6.5}$$

where a_i – constants and then:

$$f_0 = f(h) - a_1 h - a_2 h^2 - a_3 h^3 - \cdots. \tag{6.6}$$

For δ-convergence studies, where the horizon shrinks while mesh spacing is constant, f_0 should be the same for all δ values at constant mesh spacing h. Similarly, for δm-convergence studies, where the horizon shrinks and mesh spacing increases, f_0 should be the same regardless of δ and h combination. Consider a case, in which mesh density increases from 40 000 to 625 000 nodes (h decreases from 0.001 m to 0.0004 m), then the f_0 value should be the same

for each separate horizon – $\delta = \sqrt{2}h$, $\delta = 2h$, $\delta = 3h$ and $\delta = 4h$. This can be used to compute f_0 value for all convergence cases.

There are several unknowns in (6.6). For a single convergence case f_0 and a_i should be the same and only $f(h)$ and h should change, it follows that f_0 and a_i can be found from a system of non-linear equations. Such a system would have five equations in δ-convergence cases (one for each mesh density) or four equations in δm-convergence cases (one for each horizon value). These systems were solved separately by requiring a_i to be the same in all equations and minimizing the mean squared error between f_0 of each equation and the average f_0. These values were computed using a Python programming language script that employed the Scipy library [114–116].

The convergence order p can be found by minimizing the difference between the left-hand side and the right-hand side in (6.3). Only the asymptotic range of convergence is of interest. This is the range with the smallest mesh spacing, therefore, only the p computed with the 625 000 node model ($h = 0.0004$ m) will be presented.

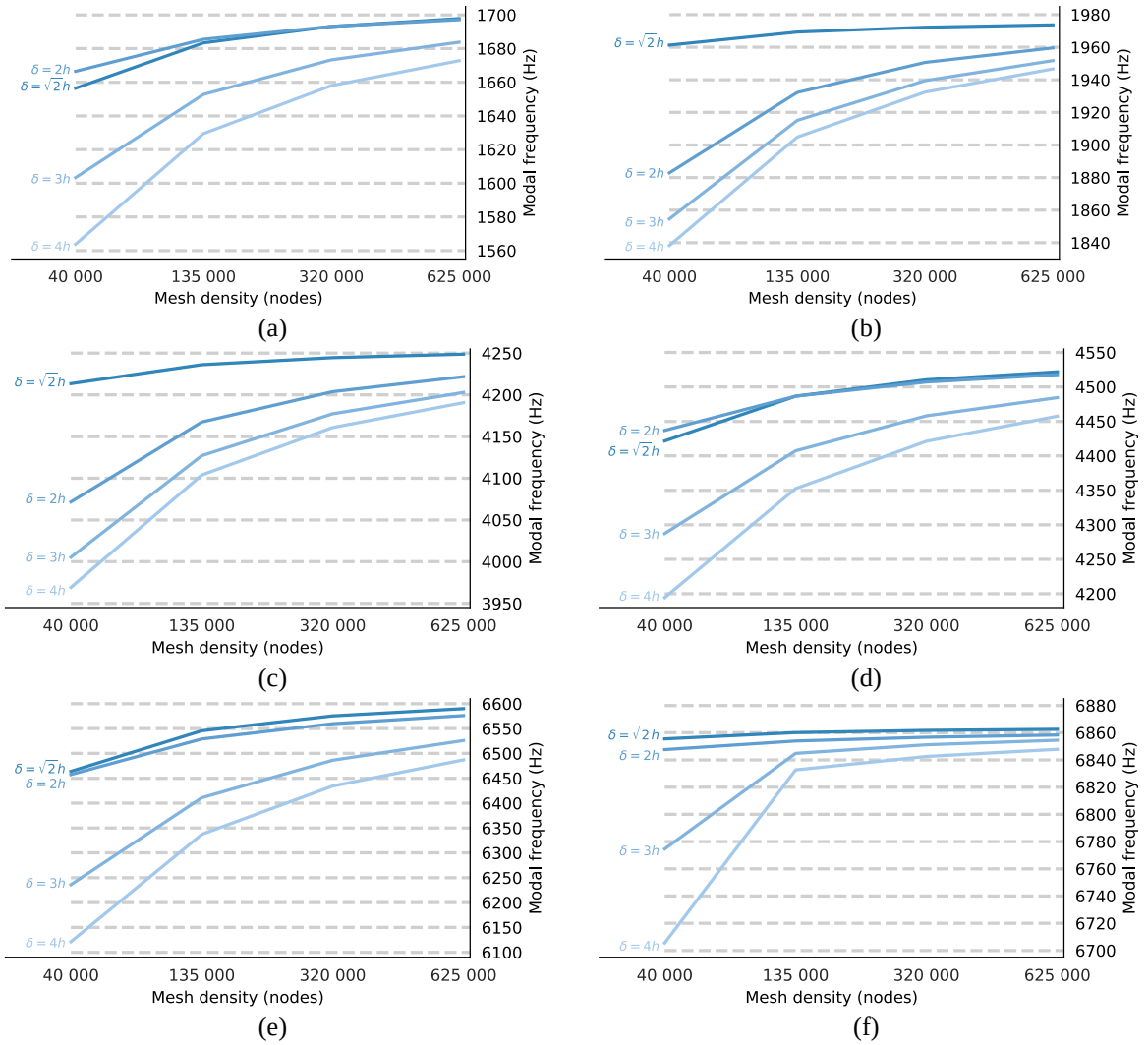

Figure 6.1. δm-convergence at Healthy configuration. a – 1st bending mode, b – 1st torsional mode, c – 2nd torsional mode, d – 2nd bending mode, e – 1st transversal bending mode, f – 1st in-plane bending mode.

6.2 Results

Convergence studies are presented for simulations at Healthy configuration because the same meshes and horizon lengths were used for all crack configurations, so the differences in convergence were small. δm-convergence and δ-convergence plots are presented in figures 6.1 and 6.2 respectively.

δm-convergence plots for the first six modes are presented in figure 6.1. All presented plots show that the computed modal frequencies approach the continuum value asymptotically as the mesh density increases. Generally, simulations with longer horizon result in lower modal frequencies. There are a few exceptions. When 40 000 and 135 000 node meshes are used, then the simulations with $\delta = 2h$ result in higher frequencies than simulations with $\delta = \sqrt{2}h$ for the 1st bending and the 2nd bending modes. Most likely this is caused by numerical approximation errors, where low density models' do not represent the actual objects behavior well enough.

Table 6.1

δm-convergence orders p and the percent difference between the values of the constant C for the 320 000 and 625 000 node models Δ_C.

	Mode					
	1st bending	1st torsional	2nd torsional	2nd bending	1st transversal bending	1st in-plane bending
$p_{\delta=\sqrt{2}h}$	1.815	1.593	1.597	1.767	1.743	1.989
$p_{\delta=2h}$	1.496	1.759	1.706	1.445	1.368	0.975
$p_{\delta=3h}$	1.591	1.632	1.557	1.508	1.474	0.728
$p_{\delta=4h}$, Hz	1.513	1.533	1.438	1.423	1.363	0.702
$\Delta_C^{\delta=\sqrt{2}h}$, %	1.30%	2.94%	2.41%	1.44%	1.61%	0.09%
$\Delta_C^{\delta=2h}$, %	1.30%	1.00%	1.00%	1.19%	0.94%	1.63%
$\Delta_C^{\delta=3h}$, %	0.17%	0.18%	0.32%	0.16%	0.02%	11.58%
$\Delta_C^{\delta=4h}$, %	0.45%	0.41%	0.77%	0.27%	0.09%	11.59%

The computed δm-convergence orders are presented in table 6.1. In all cases, convergence is not linear, but of some higher order $p > 1$, which means that even little increase in mesh density gives a large gain in accuracy. Generally, it is between 1 and 2 so it doesn't reach quadratic convergence.

The Δ_C values in table 6.1 show the absolute percent difference between two values of the constant C for the 320 000 and 625 000 node models. Please see equation (6.4) for calculation details. When the change in the constant C between two mesh densities is sufficiently small, it can be said that the asymptotic range of mesh convergence is reached. Most differences were within 0 % to 3 % range, which shows that the 625 000 node model has a low numerical error.

There were two exceptions – results for the 1st in-plane bending mode when $\delta = 3h$ or $\delta = 4h$. For both the percent difference between C values is about 11 %. However, the figure 6.1f shows that there is very little difference between computed frequencies with the 320 000 or the 625 000 node model. The convergence order values p were computed using the frequency values at all four studied mesh densities so they describe convergence over all mesh densities . There is a large jump between values from the 40 000 node model and the 135 000 node model,

but at higher mesh densities the results change little. Equation (6.4) doesn't take this into account, so the percent differences are larger than they would be if convergence orders were calculated only using the denser models.

δ-convergence plots are presented in figure 6.2 Horizon on the x axis is showed in decreasing order from $\delta = 4h$ to $\delta = \sqrt{2}h$, because commonly we read from left to right and showing convergence in the same direction presents the data more clearly. In mesh convergences, as the number of nodes increase, the computed value tends to the continuum value because the numerical error is smaller with every step, therefore the process is asymptotic. The δ-convergence, however, shows how a non-local solution tends to a local solution. The numerical error due to mesh density stays the same as the horizon shrinks, therefore, this process need not be asymptotic. The convergence is asymptotic for the 1st in-plane bending mode (figure 6.2f), but is not asymptotic for other modes in figures 6.2a through 6.2e. This shows that the difference between the non-local and the local solution does not shrink smoothly with decreasing horizon length.

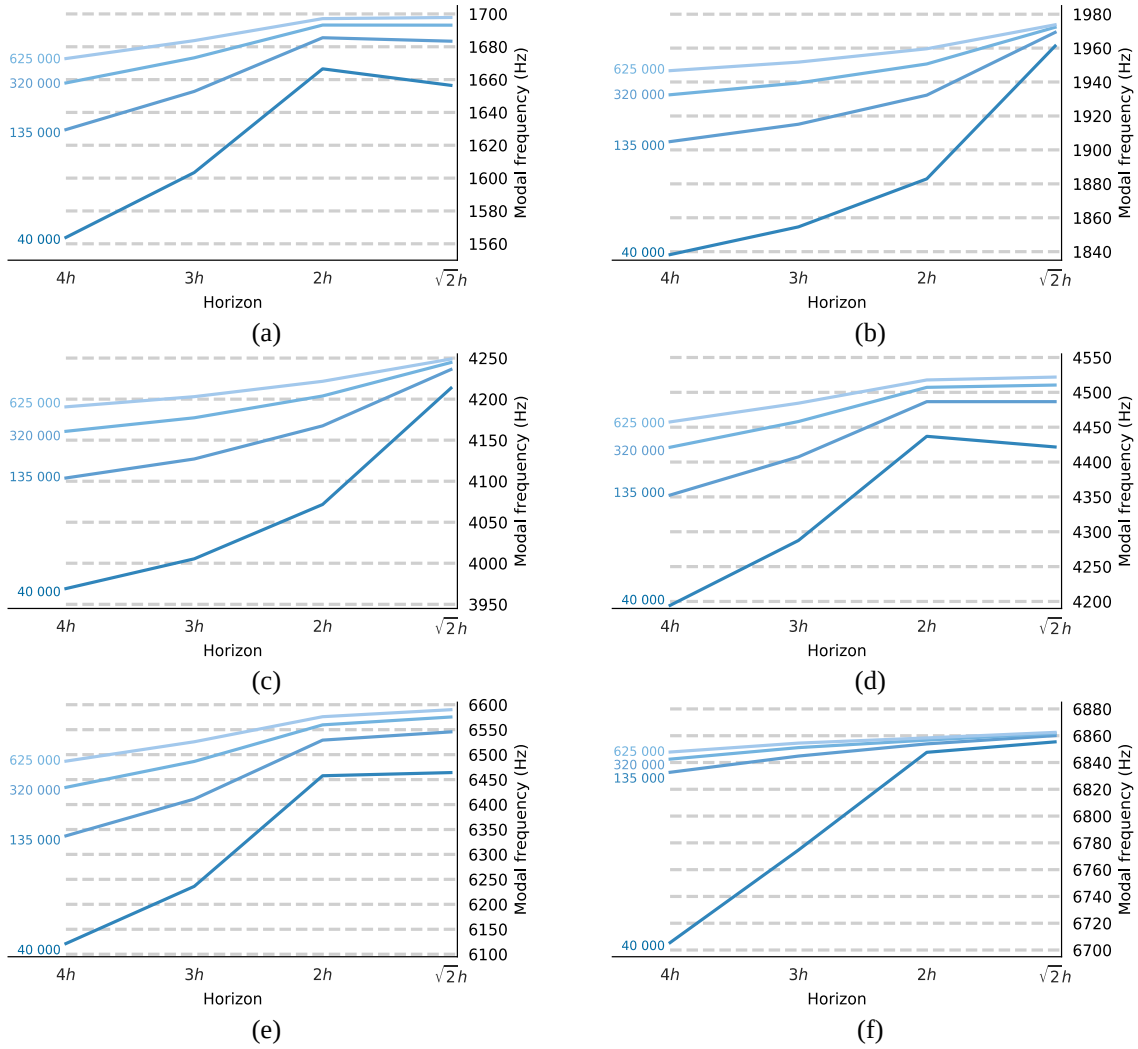

Figure 6.2. δ-convergence at Healthy configuration. a – 1st bending mode, b – 1st torsional mode, c – 2nd torsional mode, d – 2nd bending mode, e – 1st transversal bending mode, f – 1st in-plane bending mode.

For the first two bending modes and the 1st transversal bending mode in figures 6.2a, 6.2d and 6.2e values converge rapidly till $\delta = 2h$ and do not change significantly when horizon decreases to $\delta = \sqrt{2}h$. The 1st and the 2nd torsional mode's results tend to a single value at $\delta = \sqrt{2}h$ with no exceptions. Lastly, the results of the 1st in-plane bending mode converge in the same way as results for other modes.

7 DEMONSTRATION OF PERIDYNAMIC MODAL ANALYSIS APPLICATION

This chapter demonstrates how the peridynamic modal analysis can be used together with damage models. First, the modal parameters for an undamaged model will be obtained, then a fatigue damage simulation will be run, lastly, the modal analysis will be run again to obtain the modal parameters of a damaged model.

7.1 Computational model

A simple dog-bone tensile test specimen was used for demonstration. Its dimensions are presented in figure 7.1. Peridigm doesn't have an internal mesh generator, therefore, the mesh has to be supplied in a text file. Its format is described in chapter 3.1 Peridynamic implementation. The current model was first created in Ansys FE software using 8-node solid elements. The centroid coordinates of these elements and their volumes were then exported and transformed into a single text file that was used as the mesh file for Peridigm. The node size was not constant throughout the model, because it had an irregular form. Nodes were smaller closer to the narrowest part. The horizon was set to 0.0015001 m and there were 204 000 nodes in the model.

Steel data from [117] were used for the material parameters. Simulations were run using an elastic material model. Although steel is an elastic-plastic material, deformations were kept below the elastic limit, so an elastic model was accurate. The material parameters were:

- Density – 7850.0 kg/m^3;
- Poisson's Ratio – 0.30;
- Young's Modulus – 189.9 GPa.

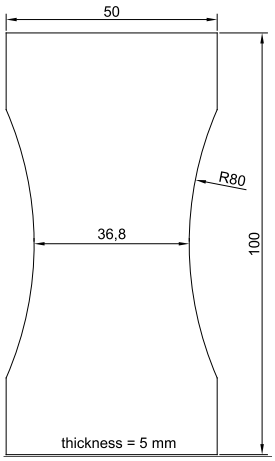

Figure 7.1. The model used in the demonstration.

The first 12 modes were computed, and no boundary conditions were applied in both modal analyses. The first six were rigid-body motion modes that will not be used hereafter.

In the fatigue simulation, constant displacement of 9e^{-5} m was applied at both ends in the opposite y directions. Boundary conditions were applied to groups of nodes within one horizon from either end. Additionally, the damage was disabled for any node within 3δ from both ends

to avoid any unphysical behavior close to the BCs. Fatigue damage model parameters are presented in table 7.1. Linear time mapping, please see the definition in chapter 7.1 Fatigue damage model, was used with τ values of $1e^{-5}$ for the first three time steps and $1e^{-4}$ for the next 57 time steps.

7.2 Fatigue damage model

The PD fatigue damage model used in this thesis was introduced in [47] and used in [48,118,119]. Other researchers have also developed fatigue damage models [78,120], however, these models use bond-based peridynamic theory and simulate only the crack growth phase. A small overview of the model is given here for completeness.

A body undergoes some cyclic deformation between two extremes + and -, then bond strains at each extreme are s_{ij}^{+} and s_{ij}^{-}, but the cyclic bond strain ε_{ij} is:

$$s_{ij}^{+} = \frac{\left|\boldsymbol{Y}^{+}\langle\boldsymbol{\xi}_{ij}\rangle\right| - \left|\boldsymbol{\xi}_{ij}\right|}{\left|\boldsymbol{\xi}_{ij}\right|}, \qquad s_{ij}^{-} = \frac{\left|\boldsymbol{Y}^{-}\langle\boldsymbol{\xi}_{ij}\rangle\right| - \left|\boldsymbol{\xi}_{ij}\right|}{\left|\boldsymbol{\xi}_{ij}\right|}, \qquad \varepsilon_{ij} = \left|s_{ij}^{+} - s_{ij}^{-}\right|. \tag{7.1}$$

For each bond define a variable called the "remaining life" $\lambda_{ij}(\boldsymbol{x}_i, \boldsymbol{\xi}_{ij}, N)$. It degrades at each loading cycle N, and a bond breaks when the remaining life is reduced to zero:

$$\lambda_{ij}(N) \leq 0. \tag{7.2}$$

At the beginning when $N = 0$:

$$\lambda_{ij}(0) = 1, \tag{7.3}$$

at each cycle, in the crack nucleation phase (phase I) the change of λ is given by

$$\frac{d\lambda_{ij}}{dN}(N) = \begin{cases} -A_I\left(\varepsilon_{ij} - \varepsilon_{\infty}\right)^{m_I} & , if\ \varepsilon_{ij} > \varepsilon_{\infty} \\ 0 & , if\ \varepsilon_{ij} \leq \varepsilon_{\infty} \end{cases}, \tag{7.4}$$

where ε_{∞} - fatigue limit under which no fatigue damage occurs,

A_I, m_I – parameters for phase I. In the phase II the remaining life changes according to:

$$\frac{d\lambda_{ij}}{dN}(N) = -A_{II}\varepsilon_{ij}^{m_{II}}, \tag{7.5}$$

where A_{II}, m_{II} – parameters for phase II.

The transition from phase I to phase II is handled by applying phase I model to bonds connected to $\boldsymbol{x}_i$ till there is a node $\boldsymbol{x}_j$ in $H_{\boldsymbol{x}_i}$ with damage

$$\phi(\boldsymbol{x}_j) \geq \phi_c, \tag{7.6}$$

where ϕ_c – damage at which phase II begins. Then reset the remaining life of bonds connected to $\boldsymbol{x}_i$ to 1 and switch to phase II model.

The natural damage growth is an advantage in PD over the classical mechanics theory. A damage model is prescribed to some nodes and, as the bonds between them break, the load is distributed to other yet unbroken bonds. Thus the applied forces are distributed over a smaller and smaller number of bonds. When this number becomes too low, a catastrophic failure occurs. No special elements or an *a priori* defined damage path is necessary for realistic damage simulations.

Hereafter, the procedure to obtain the damage model parameters is described, it was originally presented in [47], but is included for completeness. This study uses steel data from Fig. 4(a) and Fig. 5 in [117]. Although [117] presents quite old data, it contains ε-N (strain-life), K-da/dN (Paris law) data and material properties. This is beneficial because it assures that data is for the same material. Fatigue damage model parameters are shown in table 7.1.

Parameters for phase I ($A_I, m_I, \varepsilon_\infty$) are found from functions fitted to the ε-N plot, see figure 7.2. The fitted power law function take the same form, $y = ax^b$, as the phase I damage model in (7.4). So parameter m_I is the inverse of slope b:

$$b = -\frac{1}{m_I} \tag{7.7}$$

and parameter A_I is calculated from the value of intercept:

$$a = \frac{-logA_I}{m_I} \Rightarrow A_I = \frac{1}{a^{m_I}}. \tag{7.8}$$

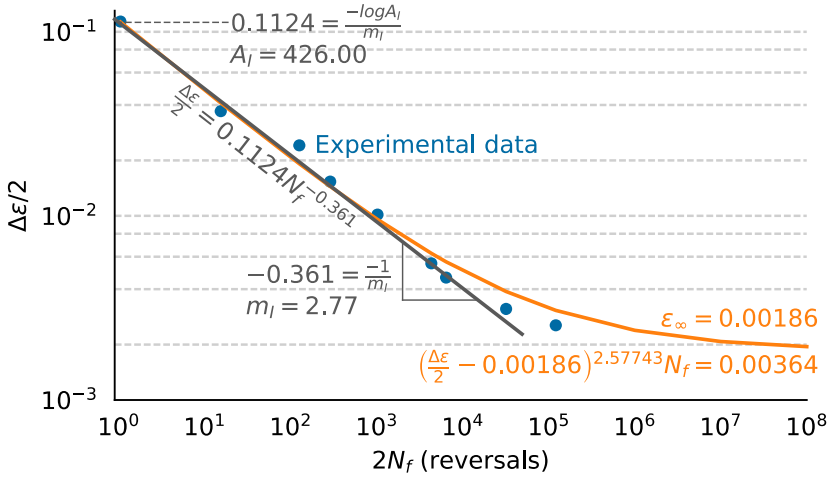

Figure 7.2. ε-N data, fitted functions and damage model parameters for phase I.

Fatigue limit of the steel was determined from function:

$$\left(\frac{\Delta\varepsilon}{2} - \varepsilon_\infty\right)^{\xi} N = C, \tag{7.9}$$

where $\frac{\Delta\varepsilon}{2}$ – strain amplitude,

ε_∞ – fatigue limit,

N – number of cycles,

ξ, C – constants.

A Paris law plot is required to find parameters for phase II. In this study R=0.05, Moist air data from figure 5 in [117] were used. The plot is replicated in figure 7.3. Fatigue damage model in (7.5) has the same form as the Paris law for crack growth:

$$\frac{da}{dN} = c\Delta K^M, \tag{7.10}$$

where $\frac{da}{dN}$ – crack growth speed,

c, M – constants,

ΔK - cyclic stress intensity factor.

ΔK is proportional to bond strain at the crack tip (in [47] called ε_{core}), therefore, $m_{II} = M$, so this parameter can be obtained directly from a Paris law plot. Remaining parameter A_{II}, however, cannot. Instead, a simulation with some trial value A'_{II} has to be run to obtain trial crack growth speed $\left(\frac{da}{dN}\right)'$. Then the real A_{II} value can be found from [47]:

$$A_{II} = A'_{II} \frac{\frac{da}{dN}}{\left(\frac{da}{dN}\right)'}. \tag{7.11}$$

To find A_{II}, a single edge notch (SEN) specimen with a pre-crack in uniaxial tension is simulated. The stress intensity at a crack tip is given by:

$$K_I = \sigma\sqrt{\pi a} F\left(\frac{a}{b}\right), \tag{7.12}$$

$$F\left(\frac{a}{b}\right) = 1.122 - 0.231\left(\frac{a}{b}\right) + 10.550\left(\frac{a}{b}\right)^2 - 21.710\left(\frac{a}{b}\right)^3 + 30.382\left(\frac{a}{b}\right)^4, \tag{7.13}$$

where σ – applied stress,

a – crack length,

b – specimen width.

The crack tip location was defined as the maximum x coordinate at which all nodes through the depth of the model has damage of at least 0.385.

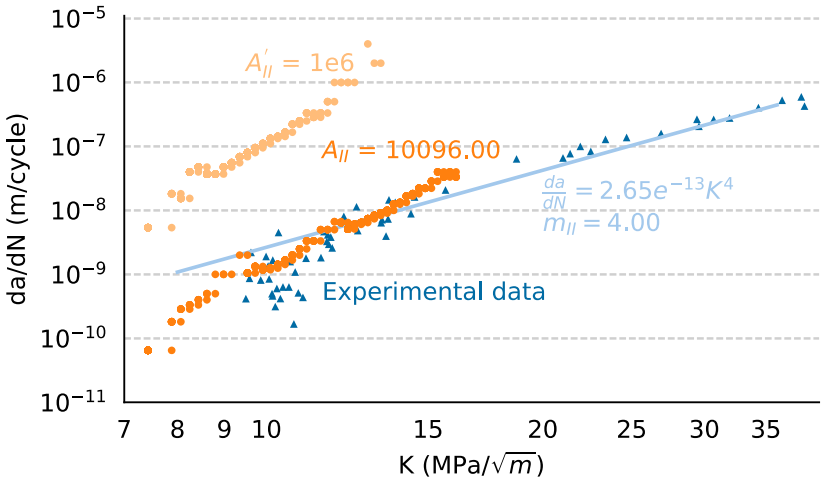

Figure 7.3. Experimental and simulated crack speed growth data and phase II parameters.

The SEN model's size was 0.05×0.008×0.003 m. It was discretized with 150'000 nodes with a spacing of 0.0002 m using the meshfree method described in [76]. The horizon is set to little over three times nodal spacing – 0.0006001. The model has a 0.005 m long pre-crack on the left side, to ensure that equation (7.12) is applicable. Force density of 6.25e10 N/m3 (equivalent to 50 MPa) has been applied to nodes within one δ of both top and bottom, and the damage is disabled for nodes within 3δ from top and bottom, to avoid unphysical behavior near boundary conditions.

Crack growth speed data only from phase II are required, so switching to phase II at low damage reduces simulation time. Damage required for the transition from phase I to phase II has been, therefore, set to 0.017. For the trial simulation $A'_{II} = 1e6$ and $m_{II} = 4.00$.

LPS material model with the same parameters as for the demonstration model was used. The first simulation (with A'_{II}) ran for 163 100 cycles after which crack turned upward, so the equation (7.12) is no longer accurate; the second simulation runs for 13 275 999 cycles till the crack splits in two. Figure 7.4 shows a simulation with A_{II} at cycle 3 099 99 (top) and step 13 275 999 (bottom). The number of cycles is large, because low applied stress causes fatigue damage to increase slowly.

Since a crack grows in discrete jumps between nodes, crack growth speed between two cycles m and n with such jumps has been calculated as the difference in crack length divided by difference between current cycle and the cycle at which the previous jump occurred:

$$\left(\frac{da}{dN}\right)' = \frac{a_n - a_m}{N_n - N_m}, \tag{7.14}$$

where a – crack length,

N – number of cycles.

(a)

(b)

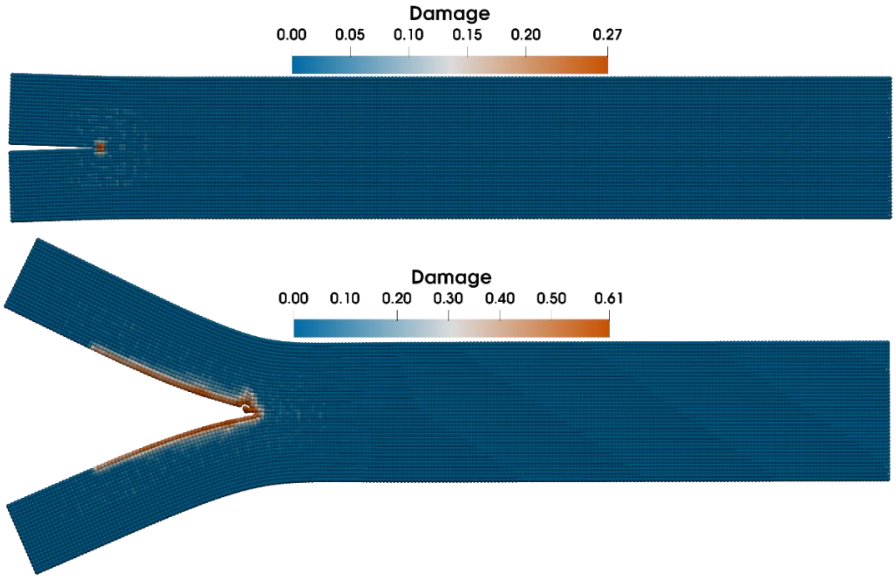

Figure 7.4. SEN specimen used to obtain A_{II}. a – 3 099 999 cycles; b – 13 275 999 cycles. Displacements are increased 10 times.

Then $\left(\frac{da}{dN}\right)'$ values are interpolated to match ΔK values from experimental data and A_{II} is calculated using equation (3.8). In total 22 A_{II} values were calculated. These values vary greatly, the coefficient of variation is 0.7134, therefore, an average value has been used. The repeated simulation with A_{II} not A'_{II} (see figure 7.3) shows an excellent agreement with the first part of the experimental data. It was not possible to determine agreement with the latter part of data, because the crack splits into two and equation (7.12) could no longer be used.

Table 7.1.

Fatigue damage model parameters

Parameter	Value
A_I	426.00
m_I	2.77
A_{II}	25237.48
m_{II}	4.00
ε_∞	0.00186
Φ_C	0.385

The demonstration model uses coarser discretization than the model of the SEN specimen. The horizon was kept at the length of three node spacings, so the actual value of the horizon is different in both simulations: 0.0015001 and 0.0006001 respectively. Change in horizon does not change A_I, m_I, m_{II} parameters, see chapter 4.3 in [47] for details, but A_{II} has to be scaled with the horizon. Equation (29) in [47] provides the means to do that:

$$A_{II}(\delta) = \widehat{A_{II}}\delta^{\frac{m_{II}-2}{2}} \rightarrow A_{II}(\delta) = 16823863 \times 0.0015001^{\frac{4-2}{2}} = 25237.48, \qquad (7.15)$$

where $\widehat{A_{II}}$ is independent of δ.

7.3 Change in modal properties due to fatigue damage

Modal frequencies and mode shapes were computed before and after the fatigue loading was applied. The fatigue simulation ran for 870 000 cycles and the model at the end of the simulation is shown in figure 7.5. Two cracks on the opposite sides of the narrowest part of the specimen grew towards each other and then each crack split into two. Furthermore, figure 7.5b shows that the damage is similar through the depth of the model.

A color legend with displacement values can't be provided for the mode shapes because a mode shape is a dimensionless representation of a structure vibrating at a modal frequency. However, the blue colors represent minimum displacements while the orange colors represent maximum displacements.

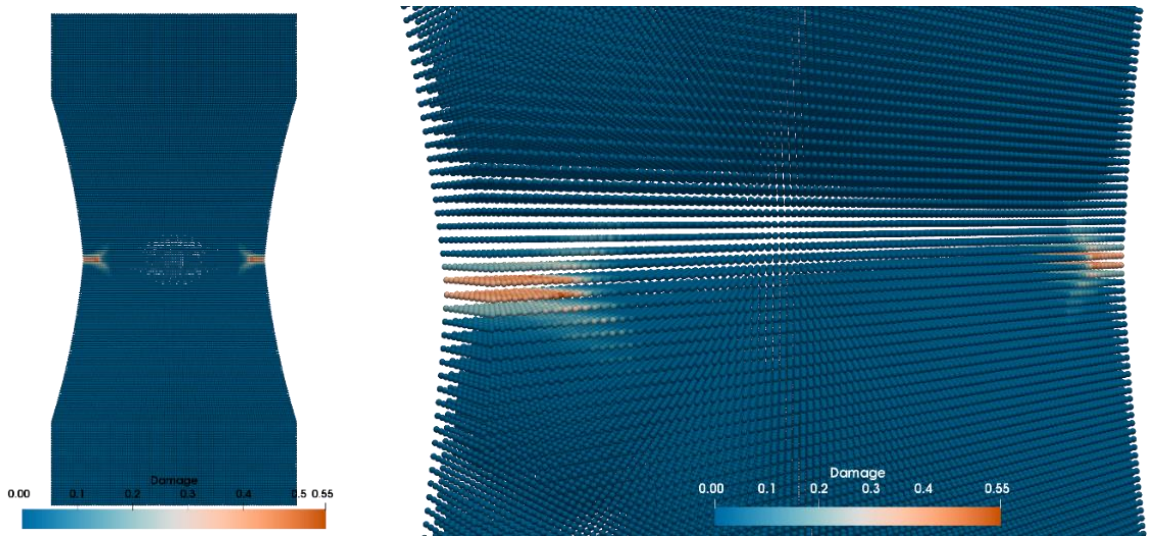

(a) (b)

Figure 7.5. The PD model showing damage after 870 000 cycles. a – the whole model, b – zone close to the damage.

Figure 7.6. The color scheme used in figure 7.7.

Table 7.2.

Modal frequencies of the undamaged model and the damaged model after 870 000 cycles.

Mode	Undamaged model (0 cycles)		Damaged model (870 000 cycles)		Δ_f, %
	Mode type	f, Hz	Mode type	f, Hz	
1st	1st bending	2446.38	1st bending	2377.17	-2.91%
2nd	1st torsional	2949.17	1st torsional	2911.42	-1.30%
3rd	2nd bending	6855.98	2nd bending	6820.82	-0.52%
4th	2nd torsional	7608.84	2nd torsional	7547.12	-0.82%
5th	1st transversal bending	11092.60	1st transversal bending	11042.50	-0.45%
6th	3rd torsional	11883.34	1st in-plane bending	11533.59	-

The computed modal frequencies are presented in table 7.2. All modal frequencies experienced frequency shift when the fatigue cracks were introduced. The largest frequency

shift was -2.91 %, for the 1st bending mode, which changed from 2446.38 Hz to 2377.17 Hz. All modes showed a frequency shift, however, for other modes, it was smaller in both absolute and relative values. This shows that the peridynamic theory allows for realistic and naturally evolving damage simulations coupled together with modal analysis for damage assessment.

The computed mode shapes before and after fatigue loading are shown in figure 7.7. Mode order was the same before and after fatigue simulation, except for the sixth mode, which changed from the 3rd torsional mode to the 1st in-plane bending mode due to the frequency shift. Introduced fatigue damage has not visibly changed mode shapes. However, quantitative rather than qualitative assessment should be done to assess the difference between mode shapes before and after fatigue damage. Such a study is outside the scope of this thesis.

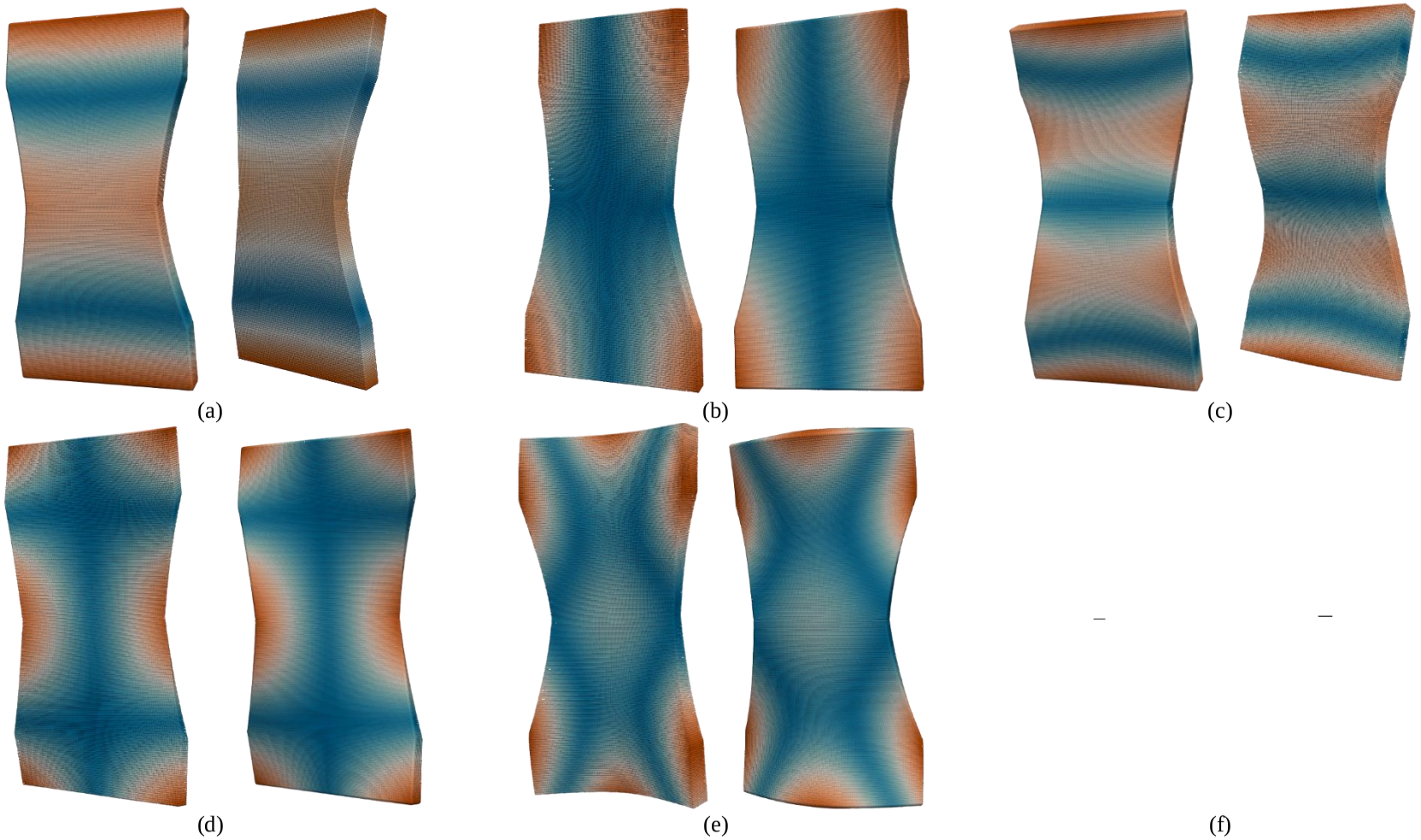

Figure 7.7**.** Mode shapes of an undamaged specimen (left) and damaged specimen (right). a –the 1st bending mode; b – the 1st torsional mode; c – the 2nd bending mode; d – the 2nd torsional mode; e – the 1st transversal bending mode; f – the sixth mode is not shown because it was the 3rd torsional mode in the undamaged configuration, but the 1st in-plane bending mode in the damaged configuration, making comparison meaningless.

8 CONCLUSIONS

This thesis is an original research project that considered a novel approach to modal analysis in the peridynamic theory. A modal solver capable of solving peridynamic modal problems was implemented and optimized for a massively-parallel computing environment. Peridynamic modal simulations of models at nine different crack configurations. Finite-element modal analyses were run for models at the same nine crack configurations. Then experimental test specimens were manufactured and tested to obtain both mechanical and modal properties. Next, the PD modal frequencies and mode shapes were verified against the FE results and validated against the experimental results. Lastly, an application of PD modal analysis was demonstrated by coupling it together with a fatigue damage simulation. Several conclusions can be drawn from this research.

1. The developed modal solver is optimized for and capable of running in a massively-parallel computing environment and solving peridynamic modal problems. Optimal parameter selection depends on the considered problem; however, optimization revealed several relations between the eigensolver, linear solver and preconditioner parameters and the simulation speed and memory use. These can be used as a starting point to determine optimal parameters in other cases.
2. The agreement between the peridynamic results and the FE results is excellent at all crack configurations. The differences in the computed modal frequencies range between 0.00 % and -4.00 %. The peridynamic modal frequencies are lower as the horizon increases. The increasing "surface effect" explains this behavior. Additionally, PD results also agree well with the experimental results. The modal frequencies are within ±3.2 % of the experimental results. Moreover, the PD frequency shift is similar to frequency shifts in FE and experimental analyses. The largest difference between the PD and the FE frequency shifts is -1.38 and 1.30 percentage points for T and S crack configurations respectively, but between the PD and the experimental frequency shifts -1.47 and 1.95 for T and S configurations respectively. The PD and the FE mode shapes agree well and are in the same order at each crack configuration. The agreement between the PD and the experimental mode shapes is good, furthermore, the change in the mode shapes from the introduced damage is similar in both analyses.
3. Two convergences – δm and δ – are considered. In the δm convergence study, results asymptotically approach a single value as the mesh density increases. The convergence is faster than linear, but slower than quadratic. Generally, the convergence order is between 1 and 2. Moreover, it is shown that the asymptotic range of convergence is reached with the 625 000 node model. Additionally, longer horizon results in lower computed frequencies, however, there are few exceptions in models with low mesh density. The δ-convergence plots are not asymptotic and show that the difference between the non-local and the local solution does not shrink smoothly as the horizon decreases.
4. An example of a practical application of the current implementation of PD modal analysis is shown. The modal solver is coupled with a peridynamic fatigue damage

simulation to demonstrate how the change in modal parameters due to fatigue damage can be assessed. First, the modal analysis is run. Next, 870 000 fatigue cycles are simulated. Last, modal analysis is run again. Mode shapes display no visible difference before and after the fatigue simulation, however, only qualitative assessment is done, but quantitative assessment is beyond the scope of this thesis. The difference in modal frequencies for the same modes ranged between -2.91 % to -0.45 %. Showing that the damage created by a fatigue simulation can be measured using modal analysis. Such measurements can be applied in model validation, manufacturing quality assurance, and structural damage detection.

LIST OF REFERENCES

[1] Italy bridge: Dozens feared dead in Genoa as motorway collapses, BBC News. (2018). https://www.bbc.com/news/world-europe-45183624 (accessed April 10, 2019).

[2] State: Voicemail about cracks 2 days before bridge fell, 6ABC News. (2018). https://6abc.com/state-voicemail-about-cracks-2-days-before-bridge-fell/3220344/ (accessed April 10, 2019).

[3] Baisā traģēdija "Maxima" – lielākā kopš neatkarības atjaunošanas, DELFI. (2013). https://www.delfi.lv/news/national/politics/baisa-tragedija-maxima-lielaka-kops-neatkaribas-atjaunosanas.d?id=43838728 (accessed April 10, 2019).

[4] Latvian State Roads, Valsts autoceļu tīkls, Statistika 2017 (State Road Network, Statistics 2017), 2018. http://lvceli.lv/wp-content/uploads/2018/08/Latvijas_Valsts_Celi_2017_115x118_tumszils_20180717_1550.pdf.

[5] Mainline, Maintenance, renewal and improvement of rail transport infrastructure to reduce economic and environmental impacts in Deliverable D1.1: Benchmark of New Technologies to Extend the Life of Elderly Rail Infrastructure European Project, 2013.

[6] D. Zonta, B. Glisic, S. Adriaenssens, Value of information: impact of monitoring on decision-making, Struct. Control Heal. Monit. 21 (2014) 1043–1056. doi:10.1002/stc.1631.

[7] S. Thöns, M. Faber, Assessing the value of structural health monitoring, in: Safety, Reliab. Risk Life-Cycle Perform. Struct. Infrastructures, CRC Press, 2014: pp. 2543–2550. doi:10.1201/b16387-367.

[8] D. Bolognani, A. Verzobio, D. Tonelli, C. Cappello, B. Glisic, D. Zonta, J. Quigley, Quantifying the benefit of structural health monitoring: what if the manager is not the owner?, Struct. Heal. Monit. 17 (2018) 1393–1409. doi:10.1177/1475921718794506.

[9] F. Nemry, H. Demirel, Impacts of Climate Change on Transport: A focus on road and rail transport infrastructures. JRC72217., 2012. doi:10.2791/15504.

[10] S.W. Doebling, C.R. Farrar, M.B. Prime, D.W. Shevitz, Damage identification and health monitoring of structural and mechanical systems from changes in their vibration characteristics: A literature review, Los Alamos, NM, 1996. doi:10.2172/249299.

[11] M. Fernandes, J.M. Hébert, The ups and downs of holoprosencephaly: dorsal versus ventral patterning forces., Clin. Genet. 73 (2008) 413–23. doi:10.1111/j.1399-0004.2008.00994.x.

[12] J.R. Casas, J.J. Moughty, Bridge Damage Detection Based on Vibration Data: Past and New Developments, Front. Built Environ. 3 (2017) 1–12. doi:10.3389/fbuil.2017.00004.

[13] X. Kong, C.-S. Cai, J. Hu, The State-of-the-Art on Framework of Vibration-Based Structural Damage Identification for Decision Making, Appl. Sci. 7 (2017) 497. doi:10.3390/app7050497.

[14] N.F. Alkayem, M. Cao, Y. Zhang, M. Bayat, Z. Su, Structural damage detection using finite element model updating with evolutionary algorithms: a survey, Neural Comput. Appl. 30 (2018) 389–411. doi:10.1007/s00521-017-3284-1.

[15] S.J. Cox, M. Embree, J.M. Hokanson, One Can Hear the Composition of a String: Experiments with an Inverse Eigenvalue Problem, SIAM Rev. 54 (2012) 157–178. doi:10.1137/080731037.

[16] The European Materials Modeling Council, The EMMC RoadMap 2018 for Materials Modelling and Informatics, 2018. https://emmc.info/wp-content/uploads/2018/09/EMMC_Roadmap2018V5a-del.pdf.

[17] European Commission, COUNCIL DECISION of 3 December 2013 establishing the specific programme implementing Horizon 2020 - the Framework Programme for Research and Innovation (2014-2020) and repealing Decisions 2006/971/EC, 2006/972/EC, 2006/973/EC, 2006/974/EC and 2006/975/EC, 2013. http://eur-lex.europa.eu/legal-content/EN/TXT/PDF/?uri=CELEX:32013D0743&qid=1455193076073&from=EN.

[18] European Commission, Horizon 2020 Work Programme 2014-2015 5. Leadership in enabling and industrial technologies ii. Nanotechnologies, Advanced Materials, Biotechnology and Advanced Manufacturing and Processing, 2015. https://ec.europa.eu/research/participants/data/ref/h2020/wp/2014_2015/main/h2020-wp1415-leit-nmp_en.pdf.

[19] European Commission, Horizon 2020 Work Programme 2016 - 2017 5.ii. Nanotechnologies, Advanced Materials, Biotechnology and Advanced Manufacturing and Processing, (2017).

[20] European Commission, Horizon 2020 Work Programme 2018-2020 5.ii. Nanotechnologies , Advanced Materials , Biotechnology and Advanced Manufacturing and Processing, (2020).

[21] S.A. Silling, Reformulation of elasticity theory for discontinuities and long-range forces, J. Mech. Phys. Solids. 48 (2000) 175–209. doi:10.1016/S0022-5096(99)00029-0.

[22] S.A. Silling, M. Epton, O. Weckner, J. Xu, E. Askari, Peridynamic states and constitutive modeling, J. Elast. 88 (2007) 151–184. doi:10.1007/s10659-007-9125-1.

[23] S.A. Silling, R.B. Lehoucq, Convergence of peridynamics to classical elasticity theory, J. Elast. 93 (2008) 13–37. doi:10.1007/s10659-008-9163-3.

[24] E. Emmrich, O. Weckner, On the well-posedness of the linear peridynamic model and its convergence towards the Navier equation of linear elasticity, Commun. Math. Sci. 5 (2007) 851–864. doi:10.4310/CMS.2007.v5.n4.a6.

[25] T. Mengesha, Q. Du, Nonlocal Constrained Value Problems for a Linear Peridynamic Navier Equation, J. Elast. 116 (2014) 27–51. doi:10.1007/s10659-013-9456-z.

[26] P. Seleson, M.L. Parks, M. Gunzburger, R.B. Lehoucq, Peridynamics as an Upscaling of Molecular Dynamics, Multiscale Model. Simul. 8 (2009) 204–227. doi:10.1137/09074807X.

[27] E. Madenci, E. Oterkus, Peridynamic Theory and Its Applications, Springer New York, New York, NY, 2014. doi:10.1007/978-1-4614-8465-3.

[28] F. Bobaru, J.T. Foster, P.H. Geubelle, S.A. Silling, Handbook of Peridynamic Modeling, CRC Press, 2016.

[29] A. Javili, R. Morasata, E. Oterkus, S. Oterkus, Peridynamics review, Math. Mech. Solids.

(2018) 1–26. doi:10.1177/1081286518803411.

[30] A.C. Eringen, D.G.B. Edelen, On nonlocal elasticity, Int. J. Eng. Sci. 10 (1972) 233–248. doi:10.1016/0020-7225(72)90039-0.

[31] E. Kröner, Elasticity theory of materials with long range cohesive forces, Int. J. Solids Struct. 3 (1967) 731–742. doi:10.1016/0020-7683(67)90049-2.

[32] A.C. Eringen, B.S. Kim, Stress concentration at the tip of crack, Mech. Res. Commun. 1 (1974) 233–237. doi:10.1016/0093-6413(74)90070-6.

[33] A.C. Eringen, B.S. Kim, On the Problem of Crack Tip in Nonlocal Elasticity, in: Contin. Mech. Asp. Geodyn. Rock Fract. Mech., Springer Netherlands, Dordrecht, 1974: pp. 107–113. doi:10.1007/978-94-010-2268-2_8.

[34] W. Gerstle, N. Sau, S. Silling, Peridynamic modeling of concrete structures, Nucl. Eng. Des. 237 (2007) 1250–1258. doi:10.1016/j.nucengdes.2006.10.002.

[35] W. Gerstle, N. Sau, N. Sakhavand, On peridynamic computational simulation of concrete structures, in: Am. Concr. Institute, ACI Spec. Publ., 2009: pp. 245–264. http://www.di.uson.mx/departamentos/dicym/images/doc/SP_265_11.pdf.

[36] A. Yaghoobi, M.G. Chorzepa, Meshless modeling framework for fiber reinforced concrete structures, Comput. Struct. 161 (2015) 43–54. doi:10.1016/j.compstruc.2015.08.015.

[37] F. Shen, Q. Zhang, D. Huang, Damage and Failure Process of Concrete Structure under Uniaxial Compression Based on Peridynamics Modeling, 2013 (2013).

[38] P. Perré, G. Almeida, M. Ayouz, X. Frank, New modelling approaches to predict wood properties from its cellular structure: image-based representation and meshless methods, Ann. For. Sci. (2015). doi:10.1007/s13595-015-0519-0.

[39] E. Madenci, S. Oterkus, Ordinary state-based peridynamics for plastic deformation according to von Mises yield criteria with isotropic hardening, J. Mech. Phys. Solids. 86 (2016) 192–219. doi:10.1016/j.jmps.2015.09.016.

[40] J. a Mitchell, A Nonlocal , Ordinary , State-Based Plasticity Model for Peridynamics, 2011.

[41] Y.L. Hu, N.V. De Carvalho, E. Madenci, Peridynamic modeling of delamination growth in composite laminates, Compos. Struct. 132 (2015) 610–620. doi:10.1016/j.compstruct.2015.05.079.

[42] K. Colavito, Peridynamics for failure and residual strength prediction of fiber-reinforced composites, 2013. http://search.proquest.com/docview/1475241115?accountid=45156.

[43] B. Kilic, A. Agwai, E. Madenci, Peridynamic theory for progressive damage prediction in center-cracked composite laminates, Compos. Struct. 90 (2009) 141–151. doi:10.1016/j.compstruct.2009.02.015.

[44] C. Diyaroglu, E. Oterkus, E. Madenci, T. Rabczuk, A. Siddiq, Peridynamic modeling of composite laminates under explosive loading, Compos. Struct. 144 (2016) 14–23. doi:10.1016/j.compstruct.2016.02.018.

[45] Y. Hu, E. Madenci, N. Phan, Peridynamics for predicting damage and its growth in composites, (2017) 1214–1226. doi:10.1111/ffe.12618.

[46] F. Bobaru, Y.D. Ha, W. Hu, Damage progression from impact in layered glass modeled with peridynamics, Cent. Eur. J. Eng. 2 (2012) 551–561. doi:10.2478/s1353101200206.

[47] S. Silling, A. Askari, Peridynamic model for fatigue cracks SANDIA REPORT SAND2014-18590, Albuquerque, 2014. http://docs.lib.purdue.edu/ses2014/mss/cfm/22/.

[48] G. Zhang, Q. Le, A. Loghin, A. Subramaniyan, F. Bobaru, Validation of a peridynamic model for fatigue cracking, Eng. Fract. Mech. 162 (2016) 76–94. doi:10.1016/j.engfracmech.2016.05.008.

[49] A. Freimanis, S. Kaewunruen, Peridynamic Analysis of Rail Squats, Appl. Sci. 8 (2018) 2299. doi:10.3390/app8112299.

[50] J. Jung, J. Seok, Mixed-mode fatigue crack growth analysis using peridynamic approach, Int. J. Fatigue. 103 (2017) 591–603. doi:10.1016/j.ijfatigue.2017.06.008.

[51] E. Oterkus, I. Guven, E. Madenci, Fatigue failure model with peridynamic theory, 2010 12th IEEE Intersoc. Conf. Therm. Thermomechanical Phenom. Electron. Syst. ITherm 2010. (2010). doi:10.1109/ITHERM.2010.5501273.

[52] F. Baber, I. Guven, Solder joint fatigue life prediction using peridynamic approach, Microelectron. Reliab. 79 (2017) 20–31. doi:10.1016/j.microrel.2017.10.004.

[53] D. De Meo, C. Diyaroglu, N. Zhu, E. Oterkus, M. Amir Siddiq, Modelling of stress-corrosion cracking by using peridynamics, Int. J. Hydrogen Energy. 41 (2016) 6593–6609. doi:10.1016/j.ijhydene.2016.02.154.

[54] M. Ghajari, L. Iannucci, P. Curtis, A peridynamic material model for the analysis of dynamic crack propagation in orthotropic media, Comput. Methods Appl. Mech. Eng. 276 (2014) 431–452. doi:10.1016/j.cma.2014.04.002.

[55] M. Behzadinasab, T.J. Vogler, A.M. Peterson, R. Rahman, J.T. Foster, Peridynamics Modeling of a Shock Wave Perturbation Decay Experiment in Granular Materials with Intra-granular Fracture, J. Dyn. Behav. Mater. 4 (2018) 529–542. doi:10.1007/s40870-018-0174-2.

[56] H. Ouchi, A. Katiyar, J.T. Foster, M.M. Sharma, A Peridynamics Model for the Propagation of Hydraulic Fractures in Naturally Fractured Reservoirs, SPE J. 22 (2017) 1082–1102. doi:10.2118/173361-PA.

[57] L.Y. Ye, C. Wang, X. Chang, H.Y. Zhang, Propeller-ice contact modeling with peridynamics, Ocean Eng. 139 (2017) 54–64. doi:10.1016/j.oceaneng.2017.04.037.

[58] F. Bobaru, G. Zhang, Why do cracks branch? A peridynamic investigation of dynamic brittle fracture, Int. J. Fract. (2016). doi:DOI 10.1007/s10704-015-0056-8.

[59] S.A. Silling, O. Weckner, E. Askari, F. Bobaru, Crack nucleation in a peridynamic solid, Int. J. Fract. 162 (2010) 219–227. doi:10.1007/s10704-010-9447-z.

[60] D.J. Littlewood, K. Mish, K. Pierson, Peridynamic Simulation of Damage Evolution for Structural Health Monitoring, Vol. 8 Mech. Solids, Struct. Fluids. (2012) 1. doi:10.1115/IMECE2012-86400.

[61] S.A. Silling, R.B. Lehoucq, Peridynamic theory of solid mechanics. Advances in Applied Mechanics, Adv. Appl. Mech. 44 (2010) 73–168.

[62] S.G. Kelly, Mechanical Vibrations: Theory and Applications, SI, 2012.

[63] M. Paz, W. Leigh, Structural Dynamics: Theory and Computation, 2012. https://books.google.com.br/books?id=ftd5BgAAQBAJ.

[64] L. Meirovitch, Fundamentals of Vibrations, 2001. doi:10.1115/1.1421112.

[65] J. He, Z.-F. Fu, Modal Analysis, 1st ed., Butterworth-Heinemann, 2001. doi:10.1109/IEMBS.2010.5626667.

[66] G. Strang, Linear Algebra and its Applications, 2009. doi:10.1016/B978-0-12-387000-1.01001-9.

[67] M. Heroux, Epetra performance optimization guide, Albuquerque, 2005. http://trilinos.sandia.gov/packages/epetra/EpetraPerformanceGuide.pdf.

[68] R.W. Macek, S.A. Silling, Peridynamics via finite element analysis, Finite Elem. Anal. Des. 43 (2007) 1169–1178. doi:10.1016/j.finel.2007.08.012.

[69] J. Amani, E. Oterkus, P. Areias, G. Zi, T. Nguyen-Thoi, T. Rabczuk, A non-ordinary state-based peridynamics formulation for thermoplastic fracture, Int. J. Impact Eng. 87 (2016) 83–94. doi:10.1016/j.ijimpeng.2015.06.019.

[70] J. O'Grady, J. Foster, Peridynamic beams: A non-ordinary, state-based model, Int. J. Solids Struct. 51 (2014) 3177–3183. doi:10.1016/j.ijsolstr.2014.05.014.

[71] J. O'Grady, J. Foster, Peridynamic plates and flat shells: A non-ordinary, state-based model, Int. J. Solids Struct. 51 (2014) 4572–4579. doi:10.1016/j.ijsolstr.2014.09.003.

[72] X. Gu, E. Madenci, Q. Zhang, Revisit of non-ordinary state-based peridynamics, Eng. Fract. Mech. 190 (2018) 31–52. doi:10.1016/j.engfracmech.2017.11.039.

[73] M.S. Breitenfeld, P.H. Geubelle, O. Weckner, S.A. Silling, Non-ordinary state-based peridynamic analysis of stationary crack problems, Comput. Methods Appl. Mech. Eng. 272 (2014) 233–250. doi:10.1016/j.cma.2014.01.002.

[74] P. Seleson, M. Parks, on the Role of the Influence Function in the Peridynamic Theory, Int. J. Multiscale Comput. Eng. 9 (2011) 689–706. doi:10.1615/IntJMultCompEng.2011002527.

[75] A.F. Queiruga, G. Moridis, Numerical experiments on the convergence properties of state-based peridynamic laws and influence functions in two-dimensional problems, Comput. Methods Appl. Mech. Eng. 322 (2017) 97–122. doi:10.1016/j.cma.2017.04.016.

[76] S.A. Silling, E. Askari, A meshfree method based on the peridynamic model of solid mechanics, Comput. Struct. 83 (2005) 1526–1535. doi:10.1016/j.compstruc.2004.11.026.

[77] J.T. Foster, S.A. Silling, W. Chen, an Energy Based Failure Criterion for Use With Peridynamic States, Int. J. Multiscale Comput. Eng. 9 (2011) 675–687. doi:10.1615/IntJMultCompEng.2011002407.

[78] E. Oterkus, I. Guven, E. Madenci, Fatigue failure model with peridynamic theory, in: 2010 12th IEEE Intersoc. Conf. Therm. Thermomechanical Phenom. Electron. Syst. ITherm 2010, 2010. doi:10.1109/ITHERM.2010.5501273.

[79] M.R. Tupek, J.J. Rimoli, R. Radovitzky, An approach for incorporating classical continuum damage models in state-based peridynamics, Comput. Methods Appl. Mech. Eng. 263 (2013) 20–26. doi:10.1016/j.cma.2013.04.012.

[80] P. Roy, A. Pathrikar, S.P. Deepu, D. Roy, Peridynamics damage model through phase field theory, Int. J. Mech. Sci. 128–129 (2017) 181–193. doi:10.1016/j.ijmecsci.2017.04.016.

[81] J.H. Wilkinson, C. Reinsch, Handbook for Automatic Computation.-Vol. 2: Linear Algebra, 1971.

[82] Y. Saad, Numerical Methods for Large Eigenvalue Problems, Numer. Methods Large Eig. Probl. (2011) 285. doi:10.1137/1.9781611970739.

[83] Y. Saad, Iterative Methods for Sparse Linear Systems, Society for Industrial and Applied Mathematics, 2003. doi:10.1137/1.9780898718003.

[84] M.L. Parks, D.J. Littlewood, J. a Mitchell, S. a Silling, Peridigm Users ' Guide, 2012.

[85] D.J. Littlewood, Roadmap for Peridynamic Software Implementation, Albuquerque, 2015. http://www.sandia.gov/~djlittl/docs/PeridynamicSoftwareRoadmap.pdf.

[86] J.E. Roman, C. Campos, E. Romero, A. Tomas, SLEPc Users Manual, 2016.

[87] R.B. Lehoucq, D.C. Sorensen, C. Yang, ARPACK Users' Guide, Society for Industrial and Applied Mathematics, 1998. doi:10.1137/1.9780898719628.

[88] Spectra - C++ Library For Large Scale Eigenvalue Problems, (2019). https://spectralib.org/index.html (accessed May 27, 2019).

[89] M. Sala, M.A. Heroux, D.M. Day, J.M. Willenbring, Trilinos Tutorial, 2010.

[90] S. Report, Teuchos::RCP Beginner's Guide, 3268 (2010).

[91] M. Sala, Robust Algebraic Preconditioners with IFPACK 3.0, Albuquerque, 2005. http://trilinos.sandia.gov/packages/ifpack/.

[92] E. Bavier, M. Hoemmen, S. Rajamanickam, H. Thornquist, Amesos2 and Belos: Direct and iterative solvers for large sparse linear systems, Sci. Program. 20 (2012) 241–255. doi:10.3233/SPR-2012-0352.

[93] C.G. Baker, U.L. Hetmaniuk, R.B. Lehoucq, H.K. Thornquist, Anasazi software for the numerical solution of large-scale eigenvalue problems, ACM Trans. Math. Softw. 36 (2009) 13. doi:10.1145/1527286.1527287.

[94] E.G. Boman, K.D. Devine, R.B. Lehoucq, N.L. Slattengren, T. Heidi, Installing the Anasazi Eigensolver Package with Application to Some Graph Eigenvalue Problems, (2014) 19.

[95] G.W. Stewart, A Krylov--Schur Algorithm for Large Eigenproblems, SIAM J. Matrix Anal. Appl. 23 (2002) 601–614. doi:10.1137/S0895479800371529.

[96] Y. Zhou, Y. Saad, Block Krylov–Schur method for large symmetric eigenvalue problems, Numer. Algorithms. 47 (2008) 341–359. doi:10.1007/s11075-008-9192-9.

[97] R.B. Morgan, D.S. Scott, Generalizations of Davidson's Method for Computing Eigenvalues of Sparse Symmetric Matrices, SIAM J. Sci. Stat. Comput. 7 (1986) 817–825. doi:10.1137/0907054.

[98] Y. Saad, A Flexible Inner-Outer Preconditioned GMRES Algorithm, SIAM J. Sci. Comput. 14 (1993) 461–469. doi:10.1137/0914028.

[99] Y. Saad, M.H. Schultz, GMRES: A Generalized Minimal Residual Algorithm for Solving Nonsymmetric Linear Systems, SIAM J. Sci. Stat. Comput. 7 (1986) 856–869. doi:10.1137/0907058.

[100] B.L. Fox, H.D. Huskey, J.H. Wilkinson, Notes on the Solution of Algebraic, Methods. (1947).

[101] V. Eglajs, P. Audze, New approach to the design of multifactor experiments, in: Probl. Dyn. Strength, Zinatne Publishing House, Riga, 1977: pp. 104–107.

[102] M.D. McKay, R.J. Beckman, W.J. Conover, A Comparison of Three Methods for Selecting Values of Input Variables in the Analysis of Output from a Computer Code, Technometrics. 21 (1979) 239. doi:10.2307/1268522.

[103] B.G.M. Husslage, G. Rennen, E.R. van Dam, D. den Hertog, Space-filling Latin hypercube designs for computer experiments, Optim. Eng. 12 (2011) 611–630. doi:10.1007/s11081-010-9129-8.

[104] H. Schreier, J.-J. Orteu, M.A. Sutton, Image Correlation for Shape, Motion and Deformation Measurements, Springer US, Boston, MA, 2009. doi:10.1007/978-0-387-78747-3.

[105] Q. V. Le, F. Bobaru, Surface corrections for peridynamic models in elasticity and fracture, Comput. Mech. 61 (2018) 499–518. doi:10.1007/s00466-017-1469-1.

[106] Erkan Oterkus, Peridynamic Theory for Modeling Three-Dimensional Damage Growth in Metallic and Composite Structures, Arizona Üniversitesi. 9 (2008) 1–108. doi:10.1029/2007GC001699.

[107] J. Mitchell, S. Silling, D. Littlewood, A position-aware linear solid constitutive model for peridynamics, J. Mech. Mater. Struct. 10 (2015) 539–557. doi:10.2140/jomms.2015.10.539.

[108] W. Gerstle, N. Sau, S. Silling, Peridynamic Modeling of Plain and Reinforced Concrete, in: 18th Int. Conf. Struct. Mech. React. Technol. (SMiRT 18), Beijing, 2005: pp. 54–68.

[109] S. Oterkus, E. Madenci, A. Agwai, Peridynamic thermal diffusion, J. Comput. Phys. 265 (2014) 71–96. doi:10.1016/j.jcp.2014.01.027.

[110] E. Madenci, M. Dorduncu, A. Barut, N. Phan, Weak form of peridynamics for nonlocal essential and natural boundary conditions, Comput. Methods Appl. Mech. Eng. 337 (2018) 598–631. doi:10.1016/j.cma.2018.03.038.

[111] P.J. Roache, QUANTIFICATION OF UNCERTAINTY IN COMPUTATIONAL FLUID DYNAMICS, Annu. Rev. Fluid Mech. 29 (1997) 123–160. doi:10.1146/annurev.fluid.29.1.123.

[112] N.J. Higham, Accuracy and Stability of Numerical Algorithms, Society for Industrial and Applied Mathematics, 2002. doi:10.1137/1.9780898718027.

[113] F. Bobaru, M. Yang, L.F. Alves, S.A. Silling, E. Askari, J. Xu, Convergence, adaptive refinement, and scaling in 1D peridynamics, Int. J. Numer. Methods Eng. 77 (2009) 852–877. doi:10.1002/nme.2439.

[114] T.E. Oliphant, Python for Scientific Computing, Comput. Sci. Eng. 9 (2007) 10–20. doi:10.1109/MCSE.2007.58.

[115] E. Jones, T. Oliphant, P. Peterson, others, SciPy: Open source scientific tools for Python, (n.d.). http://www.scipy.org/ (accessed March 2, 2017).

[116] K.J. Millman, M. Aivazis, Python for Scientists and Engineers, Comput. Sci. Eng. 13 (2011) 9–12. doi:10.1109/MCSE.2011.36.

[117] J.J. Scutti, R.M. Pelloux, R. Fuquen-Moleno, FATIGUE BEHAVIOR OF A RAIL STEEL, Fatigue Fract. Eng. Mater. Struct. 7 (1984) 121–135. doi:10.1111/j.1460-2695.1984.tb00410.x.

[118] J. Jung, J. Seok, Mixed-mode fatigue crack growth analysis using peridynamic approach, Int. J. Fatigue. 103 (2017) 591–603. doi:10.1016/j.ijfatigue.2017.06.008.

[119] J. Jung, J. Seok, Fatigue crack growth analysis in layered heterogeneous material systems using peridynamic approach, Compos. Struct. 152 (2016) 403–407. doi:10.1016/j.compstruct.2016.05.077.

[120] F. Baber, I. Guven, Solder joint fatigue life prediction using peridynamic approach, Microelectron. Reliab. 79 (2017) 20–31. doi:10.1016/j.microrel.2017.10.004.

APPENDIX A

Table A.1.

PD modal frequencies (Hz) at Tb crack configuration.

Nodes in a model	Horizon	Mode					
		1st bending	1st torsional	2nd torsional	2nd bending	1st in-plane bending	1st trans. bending
40000	$\sqrt{2}h$	1586.33	1881.50	3977.28	4170.64	5647.60	6418.07
40000	$2h$	1594.55	1810.05	3855.18	4169.57	5630.87	6420.13
40000	$3h$	1536.46	1778.74	3786.78	4035.78	5624.28	6204.15
40000	$4h$	1499.63	1759.48	3748.08	3948.28	5605.26	6084.19
135000	$\sqrt{2}h$	1616.44	1890.11	4014.24	4222.56	5660.20	6505.61
135000	$2h$	1616.58	1857.01	3950.64	4219.48	5650.92	6494.61
135000	$3h$	1586.15	1838.85	3909.39	4148.42	5647.66	6379.19
135000	$4h$	1564.14	1827.30	3883.90	4098.00	5635.66	6304.59
320000	$\sqrt{2}h$	1622.90	1895.44	4019.95	4252.87	5664.44	6536.60
320000	$2h$	1622.67	1875.45	3984.74	4245.34	5656.18	6524.22
320000	$3h$	1604.26	1863.05	3957.37	4200.54	5653.96	6452.13
320000	$4h$	1589.95	1854.92	3940.13	4165.61	5645.11	6400.10
625000	$\sqrt{2}h$	1629.80	1896.54	4030.45	4258.63	5668.24	6552.70
625000	$2h$	1628.37	1883.83	4004.86	4253.97	5662.68	6541.46
625000	$3h$	1615.82	1875.44	3985.33	4223.76	5661.27	6492.23
625000	$4h$	1605.41	1869.71	3971.94	4198.94	5654.52	6453.63

Table A.2.

PD modal frequencies (Hz) at Tc crack configuration.

Nodes in a model	Horizon	Mode					
		1st bending	1st torsional	1st in-plane bending	2nd torsional	2nd bending	3rd torsional
40000	$\sqrt{2}h$	1343.15	1606.10	3090.54	3285.29	3667.84	5470.82
40000	$2h$	1343.37	1561.46	3078.41	3202.15	3637.75	5356.17
40000	$3h$	1300.56	1523.86	3076.56	3133.40	3535.40	5253.05
40000	$4h$	1272.20	1500.04	3063.57	3088.99	3469.86	5188.08
135000	$\sqrt{2}h$	1368.11	1615.97	3088.76	3296.72	3706.05	5510.34
135000	$2h$	1366.56	1596.02	3072.86	3262.71	3686.65	5462.72
135000	$3h$	1344.39	1575.85	3084.37	3223.93	3632.92	5402.12
135000	$4h$	1328.37	1561.62	3081.82	3197.81	3595.15	5363.53
320000	$\sqrt{2}h$	1377.09	1624.59	3108.94	3329.12	3733.12	5547.28
320000	$2h$	1375.90	1610.77	3103.02	3304.06	3719.43	5511.69
320000	$3h$	1361.51	1596.55	3102.80	3276.24	3684.61	5468.50
320000	$4h$	1350.56	1586.43	3096.94	3257.16	3657.97	5439.67
625000	$\sqrt{2}h$	1382.59	1624.96	3103.10	3323.65	3736.23	5549.54
625000	$2h$	1381.42	1616.94	3094.04	3311.07	3725.69	5531.99
625000	$3h$	1372.04	1607.80	3101.25	3292.55	3703.05	5502.34
625000	$4h$	1364.60	1600.55	3100.02	3278.85	3684.50	5481.30

Table A.3.

PD modal frequencies (Hz) at Td crack configuration.

Nodes in a model	Horizon	Mode					
		1st bending	1st torsional	1st in-plane bending	2nd torsional	2nd bending	3rd torsional
40000	$\sqrt{2}h$	1322.53	1577.53	3057.82	3090.11	3470.00	5216.60
40000	$2h$	1322.91	1533.19	3025.71	3045.92	3435.21	5077.64
40000	$3h$	1280.74	1496.37	2949.26	3044.12	3342.68	4992.53
40000	$4h$	1252.39	1472.33	2898.84	3031.35	3282.51	4934.66
135000	$\sqrt{2}h$	1346.15	1587.27	3056.34	3110.76	3506.22	5241.00
135000	$2h$	1344.99	1567.56	3040.87	3084.06	3483.75	5188.13
135000	$3h$	1323.15	1547.78	3042.20	3051.85	3434.85	5136.53
135000	$4h$	1307.23	1533.72	3012.55	3049.18	3400.22	5103.10
320000	$\sqrt{2}h$	1355.98	1596.54	3076.34	3142.63	3533.93	5283.31
320000	$2h$	1354.75	1582.95	3070.52	3122.20	3518.92	5241.21
320000	$3h$	1340.59	1568.85	3070.34	3091.84	3487.29	5202.42
320000	$4h$	1329.65	1558.85	3064.56	3070.48	3462.46	5175.94
625000	$\sqrt{2}h$	1360.76	1596.84	3070.68	3140.63	3536.60	5279.57
625000	$2h$	1359.71	1588.97	3061.86	3130.28	3524.90	5260.70
625000	$3h$	1350.49	1579.90	3068.76	3110.29	3504.18	5234.41
625000	$4h$	1343.08	1572.75	3067.46	3094.88	3486.98	5215.64

Table A.4.

PD modal frequencies (Hz) at Te crack configuration.

Nodes in a model	Horizon	Mode					
		1st bending	1st torsional	2nd torsional	1st in-plane bending	2nd bending	2nd in-plane bending
40000	$\sqrt{2}h$	1229.87	1429.84	2479.93	2697.12	3005.46	4243.68
40000	$2h$	1230.52	1390.05	2452.53	2687.09	2960.84	4226.08
40000	$3h$	1190.19	1358.00	2374.31	2685.75	2888.03	4226.99
40000	$4h$	1161.62	1337.38	2324.23	2674.34	2840.73	4210.32
135000	$\sqrt{2}h$	1246.05	1438.59	2502.23	2688.96	3029.17	4229.74
135000	$2h$	1245.85	1422.04	2494.01	2674.95	3001.05	4206.67
135000	$3h$	1225.76	1404.15	2452.81	2685.45	2965.24	4224.24
135000	$4h$	1210.10	1391.88	2423.38	2683.88	2939.40	4221.64
320000	$\sqrt{2}h$	1260.08	1451.05	2534.40	2715.42	3058.76	4271.59
320000	$2h$	1258.60	1439.31	2523.19	2710.41	3042.24	4263.22
320000	$3h$	1244.90	1426.54	2493.42	2710.54	3016.64	4263.97
320000	$4h$	1233.94	1417.76	2471.89	2705.50	2996.69	4256.24
625000	$\sqrt{2}h$	1260.99	1450.72	2532.86	2705.82	3057.56	4255.91
625000	$2h$	1260.30	1444.58	2529.49	2697.79	3043.94	4242.85
625000	$3h$	1251.80	1436.08	2510.31	2704.44	3029.05	4253.59
625000	$4h$	1244.44	1429.84	2494.98	2703.77	3016.22	4252.38

Table A.5.

PD modal frequencies (Hz) at Sb crack configuration.

Nodes in a model	Horizon	Mode					
		1st bending	1st torsional	2nd torsional	2nd bending	1st transv. bending	1st in-plane bending
40000	$\sqrt{2}h$	1638.10	1953.31	4195.93	4344.96	6458.64	6819.44
40000	$2h$	1647.63	1872.67	4050.20	4358.13	6454.73	6791.26
40000	$3h$	1589.39	1848.50	3992.01	4227.90	6233.71	6722.92
40000	$4h$	1550.92	1831.92	3955.53	4138.50	6118.17	6660.90
135000	$\sqrt{2}h$	1658.57	1957.18	4208.97	4384.02	6539.89	6809.94
135000	$2h$	1660.57	1921.15	4142.82	4383.61	6525.00	6799.68
135000	$3h$	1632.91	1906.73	4108.15	4324.37	6407.31	6798.03
135000	$4h$	1613.61	1896.82	4086.42	4285.02	6333.28	6793.31
320000	$\sqrt{2}h$	1676.54	1964.70	4228.11	4441.08	6571.98	6832.19
320000	$2h$	1676.75	1941.44	4184.64	4438.66	6556.85	6826.24
320000	$3h$	1657.48	1931.90	4161.00	4391.96	6483.50	6820.69
320000	$4h$	1642.09	1924.77	4144.32	4354.49	6431.37	6810.92
625000	$\sqrt{2}h$	1677.91	1964.06	4227.53	4439.11	6585.87	6825.86
625000	$2h$	1677.11	1950.25	4201.27	4434.55	6572.54	6820.88
625000	$3h$	1663.95	1942.63	4182.92	4402.15	6522.22	6815.91
625000	$4h$	1654.53	1938.12	4171.93	4381.29	6483.38	6812.24

Table A.6.

PD modal frequencies (Hz) at Sc crack configuration.

Nodes in a model	Horizon	Mode					
		1st bending	1st torsional	2nd torsional	2nd bending	1st transv. bending	1st in-plane bending
40000	$\sqrt{2}h$	1631.93	1950.35	4188.76	4315.01	6457.49	6810.70
40000	$2h$	1641.26	1868.97	4041.73	4327.04	6454.06	6789.51
40000	$3h$	1584.61	1846.26	3986.70	4204.40	6233.33	6709.60
40000	$4h$	1546.48	1829.61	3950.20	4116.76	6117.58	6645.68
135000	$\sqrt{2}h$	1652.41	1952.89	4199.34	4353.73	6538.77	6801.01
135000	$2h$	1653.99	1918.21	4135.62	4351.36	6524.40	6793.53
135000	$3h$	1626.71	1903.61	4100.73	4293.98	6406.61	6793.47
135000	$4h$	1608.15	1893.93	4079.64	4258.23	6332.59	6789.95
320000	$\sqrt{2}h$	1670.92	1961.91	4221.48	4413.85	6571.28	6823.39
320000	$2h$	1671.20	1938.10	4177.03	4411.64	6556.36	6817.86
320000	$3h$	1652.12	1929.14	4154.50	4365.92	6482.95	6813.32
320000	$4h$	1636.72	1921.97	4137.71	4328.30	6430.76	6804.08
625000	$\sqrt{2}h$	1670.60	1960.47	4218.82	4403.71	6585.02	6814.32
625000	$2h$	1669.79	1946.15	4191.65	4399.07	6571.78	6809.73
625000	$3h$	1657.36	1939.18	4174.74	4370.15	6521.53	6806.62
625000	$4h$	1648.26	1934.78	4164.02	4350.79	6482.64	6803.39

Table A.7.

PD modal frequencies (Hz) at Sd crack configuration.

Nodes in a model	Horizon	Mode					
		1st bending	1st torsional	2nd torsional	2nd bending	1st transv. bending	1st in-plane bending
40000	$\sqrt{2}h$	1547.01	1915.99	4013.48	4116.69	6442.76	6521.39
40000	$2h$	1549.59	1844.12	3980.88	4009.61	6424.42	6441.81
40000	$3h$	1508.06	1820.00	3922.10	3932.28	6222.06	6412.30
40000	$4h$	1476.96	1805.65	3859.19	3897.44	6106.77	6384.92
135000	$\sqrt{2}h$	1579.69	1930.34	4094.00	4146.16	6527.85	6571.18
135000	$2h$	1579.68	1895.25	4076.59	4092.21	6513.72	6535.09
135000	$3h$	1557.62	1880.34	4038.16	4051.91	6396.50	6532.65
135000	$4h$	1536.13	1871.27	3994.41	4027.06	6322.12	6507.71
320000	$\sqrt{2}h$	1596.54	1937.54	4143.42	4167.71	6559.52	6601.19
320000	$2h$	1595.79	1912.81	4118.40	4141.22	6544.93	6580.51
320000	$3h$	1581.85	1904.60	4097.17	4112.34	6472.20	6578.91
320000	$4h$	1569.04	1897.87	4076.29	4088.42	6420.20	6568.96
625000	$\sqrt{2}h$	1614.12	1941.42	4172.06	4197.17	6576.16	6652.62
625000	$2h$	1612.72	1926.97	4146.14	4189.30	6563.01	6639.36
625000	$3h$	1599.26	1919.16	4127.21	4157.67	6512.53	6624.05
625000	$4h$	1586.59	1914.00	4112.30	4127.85	6473.22	6604.33

Table A.8.

PD modal frequencies (Hz) at Se crack configuration.

Nodes in a model	Horizon	Mode					
		1st bending	1st torsional	2nd torsional	2nd bending	1st transv. bending	1st in-plane bending
40000	$\sqrt{2}h$	1528.64	1905.21	3907.72	4096.15	6439.91	6506.33
40000	$2h$	1529.98	1835.93	3884.34	3976.61	6416.91	6439.55
40000	$3h$	1490.54	1811.26	3821.12	3916.34	6219.93	6395.64
40000	$4h$	1460.68	1797.61	3765.03	3883.67	6104.94	6362.94
135000	$\sqrt{2}h$	1564.69	1923.06	4007.56	4133.53	6525.92	6560.04
135000	$2h$	1564.16	1887.79	3992.17	4074.08	6511.64	6528.95
135000	$3h$	1541.74	1872.58	3948.46	4037.44	6394.64	6527.45
135000	$4h$	1520.18	1863.64	3902.31	4014.40	6320.22	6502.62
320000	$\sqrt{2}h$	1579.27	1929.46	4044.31	4154.43	6557.26	6586.69
320000	$2h$	1578.25	1904.60	4033.17	4112.18	6542.68	6569.58
320000	$3h$	1565.22	1896.54	4010.22	4090.86	6470.19	6570.77
320000	$4h$	1552.90	1889.95	3985.41	4074.05	6418.27	6561.95
625000	$\sqrt{2}h$	1599.67	1934.95	4106.03	4171.89	6574.47	6637.18
625000	$2h$	1598.15	1920.40	4093.42	4149.73	6561.34	6626.57
625000	$3h$	1583.97	1912.03	4061.47	4125.74	6510.77	6612.98
625000	$4h$	1571.12	1906.69	4031.57	4109.11	6471.47	6594.77

Table A.9.

FE modal frequencies (Hz) at Healthy and S crack configurations.

Mode	Mode type	Nodes			
		46 359	149 188	345 117	664 146
		Healthy configuration			
1	1st bending	1706.80	1706.60	1706.50	1706.50
2	1st torsional	1976.40	1976.50	1976.50	1976.50
3	2nd torsional	4255.80	4256.40	4256.70	4256.80
4	2nd bending	4542.10	4542.80	4543.00	4543.00
5	1st in-plane bending	6601.20	6610.00	6613.10	6614.50
6	1st transversal bending	6862.10	6863.10	6863.40	6863.60
		Sb crack configuration			
1	1st bending	1664.20	1687.50	1681.40	1677.20
2	1st torsional	1960.00	1968.30	1965.70	1964.00
3	2nd torsional	4219.00	4238.40	4232.80	4229.20
4	2nd bending	4368.90	4462.20	4437.80	4421.30
5	1st transversal bending	6594.30	6606.70	6608.70	6609.40
6	3rd torsional	6768.70	6829.50	6815.70	6805.40
		Sc crack configuration			
1	1st bending	1650.50	1680.70	1672.50	1667.10
2	1st torsional	1953.90	1965.20	1961.60	1959.40
3	2nd torsional	4201.90	4230.90	4222.70	4217.40
4	2nd bending	4304.80	4430.50	4396.30	4374.30
5	1st transversal bending	6592.80	6606.00	6607.70	6608.20
6	3rd torsional	6752.80	6819.40	6803.20	6791.70
		Sd crack configuration			
1	1st bending	1589.60	1617.20	1588.00	1601.60
2	1st torsional	1936.80	1944.50	1936.80	1939.50
3	2nd torsional	4086.00	4179.80	4095.10	4134.20
4	2nd bending	4167.70	4197.50	4166.90	4175.60
5	3rd torsional	6561.00	6596.50	6543.50	6592.40
6	1st transversal bending	6584.40	6636.00	6595.70	6598.70
		Se crack configuration			
1	1st bending	1575.60	1600.80	1568.40	1585.70
2	1st torsional	1931.10	1937.40	1928.40	1932.80
3	2nd torsional	4007.60	4098.10	3984.50	4045.70
4	2nd bending	4158.50	4178.40	4152.90	4165.10
5	1st in-plane bending	6547.30	6594.10	6526.50	6576.80
6	1st transversal bending	6582.30	6620.50	6592.40	6596.60

Table A.10.

Experimental modal frequencies (Hz) at Healthy and S crack configurations.

Mode	Mode type	Specimen					μ	σ	CoV
		1	2	3	4	5			
Healthy configuration									
1	1st bending	1665.00	1677.50	1665.00	1665.00	1662.50	1667.00	5.97	0.36%
2	1st torsional	1925.00	1927.50	1927.50	1925.00	1925.00	1926.00	1.37	0.07%
3	2nd torsional	4200.00	4197.50	4197.50	4197.50	4197.50	4198.00	1.12	0.03%
4	2nd bending	4522.50	4527.50	4507.50	4515.00	4507.50	4516.00	8.94	0.20%
5	1st trans. bending	6467.50	6472.50	6460.00	6527.50	6457.50	6477.00	28.85	0.45%
Sb crack configuration									
1	1st bending	1642.50	1645.00	1645.00	1645.00	1645.00	1644.50	1.12	0.07%
2	1st torsional	1925.00	1925.00	1922.50	1925.00	1925.00	1924.50	1.12	0.06%
3	2nd torsional	4170.00	4170.00	4200.00	4200.00	4200.00	4188.00	16.43	0.39%
4	2nd bending	4450.00	4450.00	4450.00	4450.00	4450.00	4450.00	0.00	0.00%
5	1st trans. bending	6475.00	6475.00	6512.50	6505.00	6502.50	6494.00	17.73	0.27%
Sc crack configuration									
1	1st bending	1640.00	1647.50	1647.50	1640.00	1647.50	1644.50	4.11	0.25%
2	1st torsional	1920.00	1917.50	1917.50	1920.00	1920.00	1919.00	1.37	0.07%
3	2nd torsional	4177.50	4177.50	4187.50	4150.00	4177.50	4174.00	14.10	0.34%
4	2nd bending	4430.00	4427.50	4430.00	4430.00	4430.00	4429.50	1.12	0.03%
5	1st trans. bending	6517.50	6505.00	6515.00	6480.00	6502.50	6504.00	14.85	0.23%
Sd crack configuration									
1	1st bending	1557.50	1562.50	1562.50	1575.00	1577.50	1567.00	8.73	0.56%
2	1st torsional	1877.50	1877.50	1877.50	1877.50	1900.00	1882.00	10.06	0.53%
3	2nd torsional	4097.50	4102.50	4102.50	4100.00	4112.50	4103.00	5.70	0.14%
4	2nd bending	4115.00	4115.00	4145.00	4137.50	4167.50	4136.00	22.12	0.53%
5	1st trans. bending	6485.00	6457.50	6480.00	6487.50	6495.00	6481.00	14.21	0.22%
Se crack configuration									
1	1st bending	1532.50	1547.50	1555.00	1547.50	1562.50	1549.00	11.12	0.72%
2	1st torsional	1887.50	1890.00	1887.50	1887.50	1887.50	1888.00	1.12	0.06%
3	2nd torsional	3992.50	4015.00	4060.00	4042.50	4067.50	4035.50	31.39	0.78%
4	2nd bending	4062.50	4062.50	4100.00	4067.50	4100.00	4078.50	19.73	0.48%
5	1st trans. bending	6475.00	6460.00	6500.00	6457.50	6477.50	6474.00	17.01	0.26%

APPENDIX B

Table B.1.

Peridynamic and finite-element modal frequencies and percent differences between them at Healthy and T crack configurations. PD results were computed with the 625 000 node model and FE results were computed with the 664 146 node model.

Mode Type	Finite-element	Peridynamic, $\delta = \sqrt{2}h$		Peridynamic, $\delta = 4h$	
	f, Hz	f, Hz	Δ	f, Hz	Δ
Healthy configuration					
1st bending	1706.50	1697.80	-0.51%	1672.78	-2.02%
1st torsional	1976.50	1973.73	-0.14%	1946.68	-1.53%
2nd torsional	4256.80	4248.81	-0.19%	4190.64	-1.58%
2nd bending	4543.00	4521.83	-0.47%	4457.51	-1.92%
Tb configuration					
1st bending	1639.20	1629.80	-0.58%	1605.41	-2.10%
1st torsional	1903.90	1896.54	-0.39%	1869.71	-1.83%
2nd torsional	4045.50	4030.45	-0.37%	3971.94	-1.85%
2nd bending	4286.80	4258.63	-0.66%	4198.94	-2.09%
Tc configuration					
1st bending	1404.30	1382.59	-1.57%	1364.6	-2.91%
1st torsional	1642.20	1624.96	-1.06%	1600.55	-2.60%
2nd torsional	3365.80	3323.65	-1.27%	3278.85	-2.65%
2nd bending	3766.10	3736.23	-0.80%	3684.5	-2.21%
Td configuration					
1st bending	1377.10	1360.76	-1.20%	1343.08	-2.53%
1st torsional	1612.10	1596.84	-0.96%	1572.75	-2.50%
2nd torsional	3186.20	3140.63	-1.45%	3094.88	-2.95%
2nd bending	3556.00	3536.6	-0.55%	3486.98	-1.98%
Te configuration					
1st bending	1268.10	1260.99	-0.56%	1244.44	-1.90%
1st torsional	1459.40	1450.72	-0.60%	1429.84	-2.07%
2nd torsional	2592.90	2532.86	-2.37%	2494.98	-3.92%
2nd bending	3099.40	3057.56	-1.37%	3016.22	-2.76%

Table B.2.

Peridynamic and finite-element modal frequencies and percent differences between them at Healthy and S crack configurations. PD results were computed with the 625 000 node model and FE results were computed with the 664 146 node model.

Mode Type	Finite-element	Peridynamic, $\delta = \sqrt{2}h$		Peridynamic, $\delta = 4h$	
	f, Hz	f, Hz	Δ	f, Hz	Δ
Healthy configuration					
1st bending	1706.50	1697.80	-0.51%	1672.78	-2.02%
1st torsional	1976.50	1973.73	-0.14%	1946.68	-1.53%
2nd torsional	4256.80	4248.81	-0.19%	4190.64	-1.58%
2nd bending	4543.00	4521.83	-0.47%	4457.51	-1.92%
1st transversal bending	6601.20	6590.00	-0.17%	6486.96	-1.76%
Sb configuration					
1st bending	1677.20	1677.91	0.04%	1654.53	-1.37%
1st torsional	1964.00	1964.06	0.00%	1938.12	-1.34%
2nd torsional	4229.20	4227.53	-0.04%	4171.93	-1.37%
2nd bending	4421.30	4439.11	0.40%	4381.29	-0.91%
1st transversal bending	6609.40	6585.87	-0.36%	6483.38	-1.94%
Sc configuration					
1st bending	1667.10	1670.6	0.21%	1648.26	-1.14%
1st torsional	1959.40	1960.47	0.05%	1934.78	-1.27%
2nd torsional	4217.40	4218.82	0.03%	4164.02	-1.28%
2nd bending	4374.30	4403.71	0.67%	4350.79	-0.54%
1st transversal bending	6608.20	6585.02	-0.35%	6482.64	-1.94%
Sd configuration					
1st bending	1601.60	1614.12	0.78%	1586.59	-0.95%
1st torsional	1939.50	1941.42	0.10%	1914	-1.33%
2nd torsional	4134.20	4172.06	0.91%	4112.3	-0.53%
2nd bending	4175.60	4197.17	0.51%	4127.85	-1.16%
1st transversal bending	6598.70	6576.16	-0.34%	6473.22	-1.94%
Se configuration					
1st bending	1585.70	1599.67	0.87%	1571.12	-0.93%
1st torsional	1932.80	1934.95	0.11%	1906.69	-1.37%
2nd torsional	4045.70	4106.03	1.47%	4031.57	-0.35%
2nd bending	4165.10	4171.89	0.16%	4109.11	-1.36%
1st transversal bending	6596.60	6574.47	-0.34%	6471.47	-1.93%

Table B.3.

Peridynamic, experimental, and finite-element modal frequencies and percent differences between them at Healthy and T crack configurations. PD results were computed with the 625 000 node model and FE results were computed with the 664 146 node model.

Mode Type	Experimental	Peridynamic, $\delta = \sqrt{2}h$		Peridynamic, $\delta = 4h$		Finite-element	
	f, Hz	f, Hz	Δ	f, Hz	Δ	f, Hz	Δ
Healthy configuration							
1st bending	1667.00	1697.80	1.81%	1672.78	0.35%	1706.50	2.31%
1st torsional	1926.00	1973.73	2.42%	1946.68	1.06%	1976.50	2.56%
2nd torsional	4198.00	4248.81	1.20%	4190.64	-0.18%	4256.80	1.38%
2nd bending	4516.00	4521.83	0.13%	4457.51	-1.31%	4543.00	0.59%
Tb configuration							
1st bending	1594.50	1629.80	2.17%	1605.41	0.68%	1639.20	2.73%
1st torsional	1847.50	1896.54	2.59%	1869.71	1.19%	1903.90	2.96%
2nd torsional	3973.50	4030.45	1.41%	3971.94	-0.04%	4045.50	1.78%
2nd bending	4269.50	4258.63	-0.26%	4198.94	-1.68%	4286.80	0.40%
Tc configuration							
1st bending	1367.00	1382.59	1.13%	1364.6	-0.18%	1404.30	2.66%
1st torsional	1583.50	1624.96	2.55%	1600.55	1.07%	1642.20	3.57%
2nd torsional	3323.50	3323.65	0.00%	3278.85	-1.36%	3365.80	1.26%
2nd bending	3737.50	3736.23	-0.03%	3684.5	-1.44%	3766.10	0.76%
Td configuration							
1st bending	1350.50	1360.76	0.75%	1343.08	-0.55%	1377.10	1.93%
1st torsional	1570.50	1596.84	1.65%	1572.75	0.14%	1612.10	2.58%
2nd torsional	3159.00	3140.63	-0.58%	3094.88	-2.07%	3186.20	0.85%
2nd bending	3598.50	3536.6	-1.75%	3486.98	-3.20%	3556.00	-1.20%
Te configuration							
1st bending	1248.00	1260.99	1.03%	1244.44	-0.29%	1268.10	1.59%
1st torsional	1422.00	1450.72	1.98%	1429.84	0.55%	1459.40	2.56%
2nd torsional	2550.00	2532.86	-0.68%	2494.98	-2.21%	2592.90	1.65%
2nd bending	3102.00	3057.56	-1.45%	3016.22	-2.84%	3099.40	-0.08%

Table B.4.

Peridynamic, experimental, and finite-element modal frequencies and percent differences between them at Healthy and T crack configurations. PD results were computed with the 625 000 node model and FE results were computed with the 664 146 node model.

Mode Type	Experimental	Peridynamic, $\delta = \sqrt{2}h$		Peridynamic, $\delta = 4h$		Finite-element	
	f, Hz	f, Hz	Δ	f, Hz	Δ	f, Hz	Δ
Healthy configuration							
1st bending	1667.00	1697.80	1.81%	1672.78	0.35%	1706.50	2.31%
1st torsional	1926.00	1973.73	2.42%	1946.68	1.06%	1976.50	2.56%
2nd torsional	4198.00	4248.81	1.20%	4190.64	-0.18%	4256.80	1.38%
2nd bending	4516.00	4521.83	0.13%	4457.51	-1.31%	4543.00	0.59%
1st transversal bending	6477.00	6590.00	1.71%	6486.96	0.15%	6601.20	1.88%
Sb configuration							
1st bending	1644.50	1677.91	1.99%	1654.53	0.61%	1677.20	1.95%
1st torsional	1924.50	1964.06	2.01%	1938.12	0.70%	1964.00	2.01%
2nd torsional	4188.00	4227.53	0.94%	4171.93	-0.39%	4229.20	0.97%
2nd bending	4450.00	4439.11	-0.25%	4381.29	-1.57%	4421.30	-0.65%
1st transversal bending	6494.00	6585.87	1.39%	6483.38	-0.16%	6609.40	1.75%
Sc configuration							
1st bending	1644.50	1670.6	1.56%	1648.26	0.23%	1667.10	1.36%
1st torsional	1919.00	1960.47	2.12%	1934.78	0.82%	1959.40	2.06%
2nd torsional	4174.00	4218.82	1.06%	4164.02	-0.24%	4217.40	1.03%
2nd bending	4429.50	4403.71	-0.59%	4350.79	-1.81%	4374.30	-1.26%
1st transversal bending	6504.00	6585.02	1.23%	6482.64	-0.33%	6608.20	1.58%
Sd configuration							
1st bending	1567.00	1614.12	2.92%	1586.59	1.23%	1601.60	2.16%
1st torsional	1882.00	1941.42	3.06%	1914	1.67%	1939.50	2.96%
2nd torsional	4103.00	4172.06	1.66%	4112.3	0.23%	4134.20	0.75%
2nd bending	4136.00	4197.17	1.46%	4127.85	-0.20%	4175.60	0.95%
1st transversal bending	6481.00	6576.16	1.45%	6473.22	-0.12%	6598.70	1.78%
Se configuration							
1st bending	1549.00	1599.67	3.17%	1571.12	1.41%	1585.70	2.31%
1st torsional	1888.00	1934.95	2.43%	1906.69	0.98%	1932.80	2.32%
2nd torsional	4035.50	4106.03	1.72%	4031.57	-0.10%	4045.70	0.25%
2nd bending	4078.50	4171.89	2.24%	4109.11	0.74%	4165.10	2.08%
1st transversal bending	6474.00	6574.47	1.53%	6471.47	-0.04%	6596.60	1.86%